APPLICATION OF IMPEDANCE COMPUTED TOMOGRAPHY AT THE PORTAGE LA PRAIRIE LANDFILL

by

Uwe V.R. Roeper

A thesis
presented to the University of Manitoba
in partial fulfillment of the
requirements for the degree of
Master of Science in Civil Engineering
in the
Department of Civil Engineering

Winnipeg, Manitoba, June 1985

APPLICATION OF IMPEDANCE COMPUTED TOMOGRAPHY

AT THE PORTAGE LA PRAIRIE LANDFILL

BY

UWE V.R. ROEPER

A thesis submitted to the Faculty of Graduate Studies of the University of Manitoba in partial fulfillment of the requirements of the degree of

MASTER OF SCIENCE

I hereby declare that I am the sole author of this thesis.

I authorize the University of Manitoba to lend this thesis to other institutions or individuals for the purpose of scholarly research.

Uwe V.R. Roeper

I further authorize the University of Manitoba to reproduce this thesis by photocopying or by other means, in total or in part, at the request of other institutions or individuals for the purpose of scholarly research

Uwe V.R. Roeper

ABSTRACT

An application of the Electroscan™ system was undertaken at the Portage La Prairie landfill to evaluate its potential as a novel geophysical tool. The Electroscan system is an Impedance Computed Tomography technique capable of completely automatic data inversion for the imaging of three-dimensional subsurface structures. A detailed field study and geophysical survey were conducted to locate a suitable experimental site. Two electrode grids were constructed over a suspect contaminant plume, data were collected and imaged. Subsequently, Earth-resistivity data, excavations, soil logging, conductivity sampling and a magnetometer survey were used to confirm subsurface impedance structures.

Electroscan is a trademark of Quantic Electroscan Incorporated

ACKNOWLEDGEMENTS

The preparation and organization of this study and thesis was made possible under the guidance, assistance and encouragement of my advisor, Prof. A. Tamburi. I express my sincere gratitude.

To all my friends who volunteered their time and effort, I would like to extend my sincere appreciation:

Vivian Dzuba
Ian Terry
Ken Keith
Herb Ziervogel

For advice and the use of equipment, I thank the following people and departments:

Cary Mandel, Dr. A. Wexler and the Department of Electrical Engineering

Maris Rutilis, Bob Betcher and the Water Resources Branch

Dr. C.D. Anderson and the Department of Earth Sciences

Finally, I thank Stan Kaskiw for watertight carpentry work on the control box.

TABLE OF CONTENTS

LIST OF FIGURES

Figure

LIST OF PLOTS

Plot

<u>Plot</u>

LIST OF APPENDICES

Chapter 1

INTRODUCTION

The application of various geophysical methods has become a valuable asset in the remote-sensing of contaminant plumes. Distinct physical properties may be delineated from the surface and yield important subsurface information before an extensive drilling program is undertaken. Geophysical methods have proven to be fast and cost efficient. However, the primary application has been in reconnaissance study with few attempts to fully utilize the potential of these methods. Recent advances in the field of Impedance Computed Tomography promise to further extend the area of geophysical applications to complete two-, and three-dimensional imaging of subsurface structures.

Impedance structures created in the subsurface by variation of ion concentrations in the groundwater have made electrical impedance-based methods particularly suitable for the detection of leachate plumes. Contaminants may be detected and traced using their geoelectric signatures at the surface. For over 50 years, the Earth-resistivity method with its four-electrode configuration has been extensively employed in a variety of hydrogeologic studies (eg. 4, 8, 16. 17). However, a number of difficulties are associated with the interpretation of geoelectric signatures.

Geoelectric signatures, or the response of subsurface impedance structures to potential measurements carried out at the surface, are highly object dependent and complex. This creates the equivalence problem when the geoelectric signature recorded may be representative of more than one possible impedance structure. The interpretation of the Earth-resistivity data collected thus becomes ambiguous with the fitting of signatures to fixed mathematical models dependent on direct subsurface confirmation and a thorough understanding of the subsurface geology.

Extensive studies have been conducted by various researchers (eg. 1, 3, 5, 6, 10, 12, 14, 15, 19) on inversion and imaging using Earth-resistivity data. It was implied by at least one researcher (10) that the limitations on the interpretation were limited by the measurement technique of the Earth-resistivity method. The conventional array consists of four electrodes spaced along a line with two introducing a current field into the subsurface and two measuring the potential drop along the line. Successive measurements are taken by moving or spacing the electrodes along the line. In this sense, a number of one-dimensional measurements are taken to image a three-dimensional electric field. An indeterminancy necessarily results in the attempt to image the responses for all but the simplest structures.

Habberjam, (10), suggests that collecting measurements perpendicular to the line of the initial measurements allows for more effective data inversion. To extend this concept, measuring the entire potential field in an area and repeating the procedure over the same area for several linearly independent current fields should result in the necessary data to image the subsurface impedence structures without equivalence.

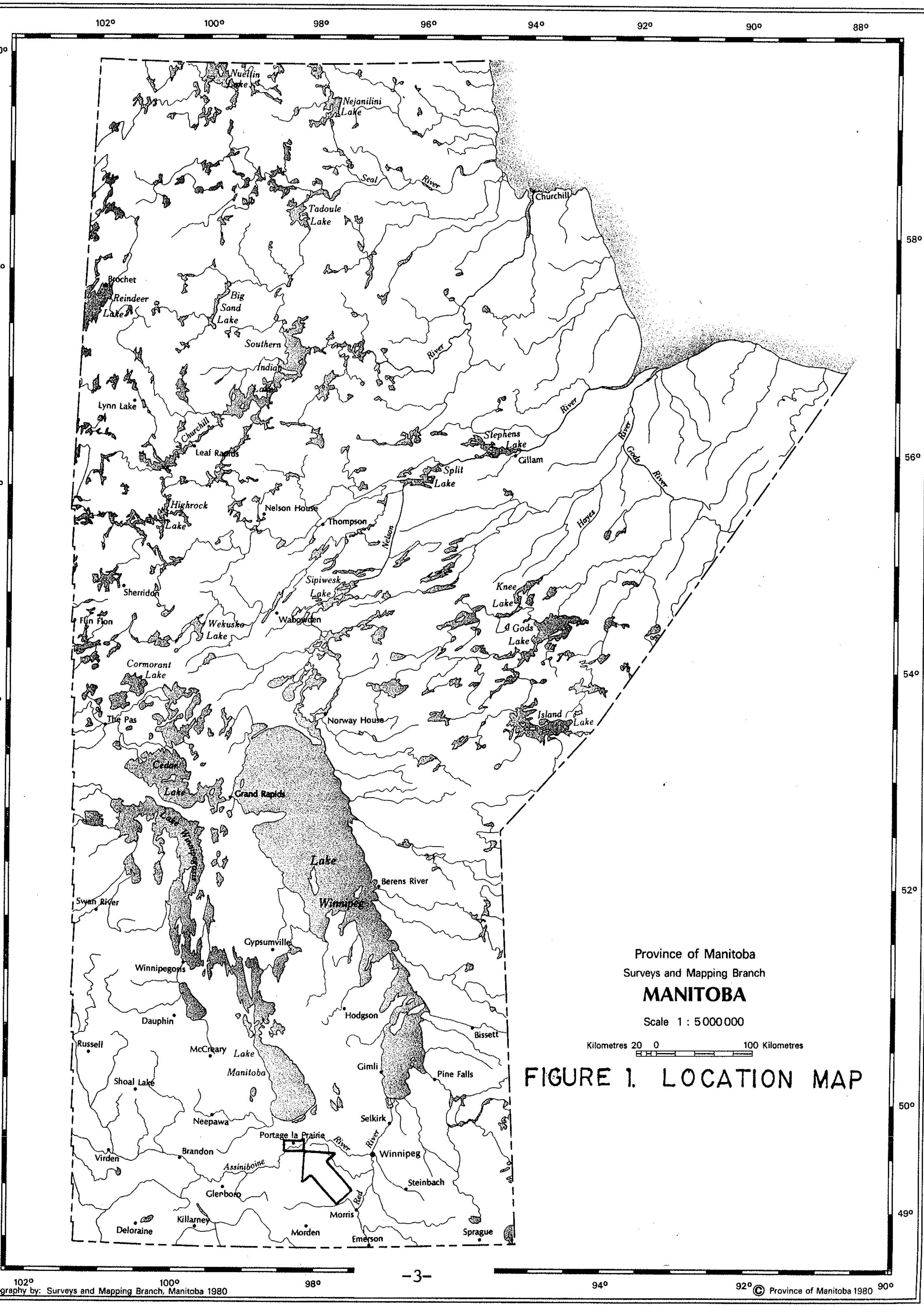

FIGURE 1. LOCATION MAP

Wexler (20) has provided significant research into this approach of Impedance Computed Tomography and its potential for direct subsurface imaging of impedance structures. An algorithm and system (Electroscan) was developed capable of solving the electric field equation using sufficient sets of linearly independent potential measurements at the surface. This is a novel and powerful approach to Impedance Computed Tomography since no assumptions are made regarding the existing structure and no mathematical models have to be used in the solution. Consequently, the application of Electroscan in hydrogeologic landfill studies promises to provide a three-dimensional subsurface imaging system far more comprehensive than the conventional Earth-resistivity method.

The landfill site chosen for the application of the Electroscan system is located in the George Lake oxbow -a meander cut-off along the Assiniboine River just south of Portage La Prairie, Manitoba (see Figure 1 and 2). Geologic, geophysical and tomographic data were collected for presentation in this study.

In Chapter II of this thesis, the conventional Earth-resistivity theory and the Electroscan system are reviewed. Some results of previous experiments with the Electroscan are discussed in Chapter III. Chapter IV covers the geology and site history relevant to this study. In Chapter V, the geophysical work, the Electroscan study, as well as subsequent subsurface sampling and a magnetometer survey are presented. A discussion and evaluation of the experiment and the obtained results may be found in Chapter VI.

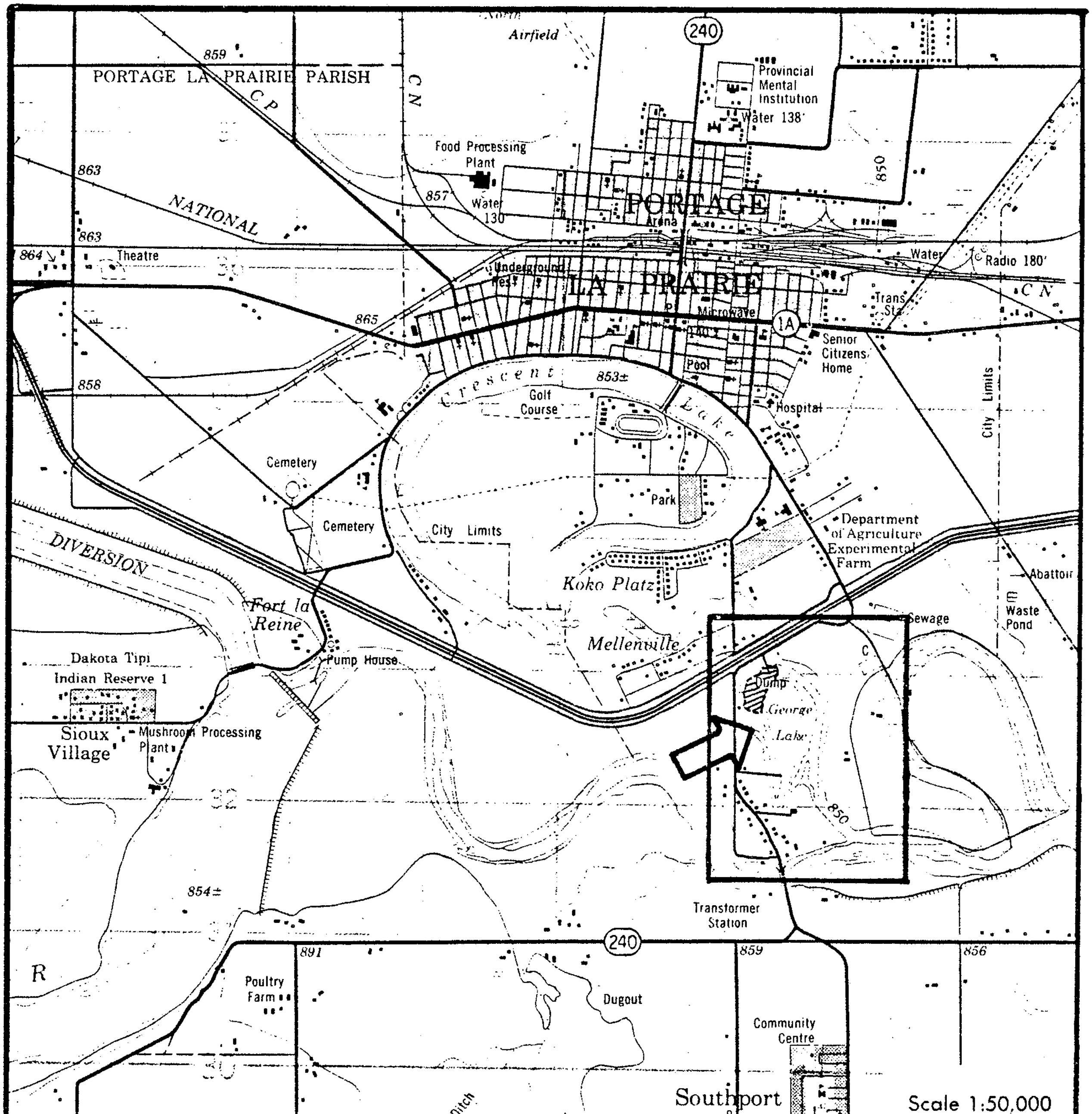

FIGURE 2. AREA MAP AND SITE LOCATION

(U. Roeper 1985)

DUMP

OXBOW

SCALE 1 : 50 000

Chapter II

GEOPHYSICAL THEORY

2.1 INTRODUCTION

In this chapter, the basic concepts, method of data collection, and data inversion will be compared for the Earth-resistivity and the Electroscan approach. It should be noted that the Earth-resistivity method will be discussed primarily in the scope of this comparison. For a broader coverage, the reader is referred to more comprehensive sources (eg. 10, 13). The patent process limits the discussion of the Electroscan method to a condensed version of Wexler (20). A more detailed review of the algorithm and system is currently not available.

2.2 EARTH-RESISTIVITY

2.2.1 CONCEPTS

For the understanding of the principles involved, the simplest electrode arrangement, the Wenner array, is most suitable. Four electrodes are spaced equally along a line. A constant current (Low frequency A.C. or D.C.) is injected through the outer electrodes while potential drops are measured across the inner electrodes (Figure 3).

Given a half-space of homogeneous material, the potential drop is directly proportional to the subsurface resistivity (Rho). Multiplying the potential by the electrode spacing and a geometric factor (2π for the Wenner array) gives the unit resistivity of the half-space material in ohm-meters. If the half-space is infinite in extent, its unit resistivity may be calculated using any electrode separation and various array configurations (if the appropriate geometric factor is used for each array).

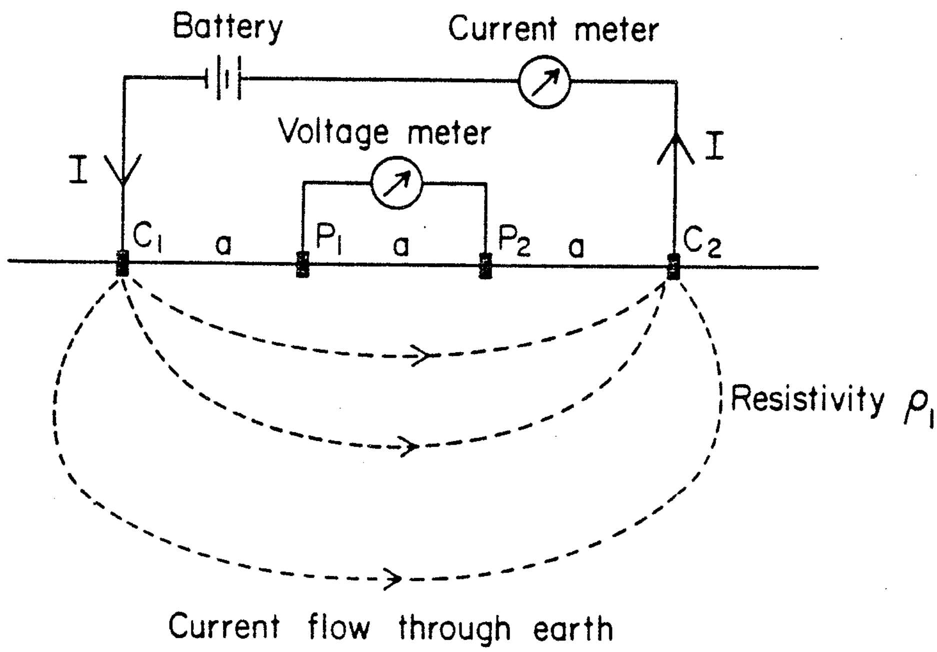

Figure 3. Earth-resistivity system, source (Mooney, 1980)

If the half-space consists of two layers of different resistivities, it can easily be shown that as electrode separation is increased, first the top and then both layers determine the resistivity measured. While the close separation results will reflect the resistivity of the upper layer, wider separation results give the apparent or bulk resistivity of both layers. Consider the example shown in Figure 4.

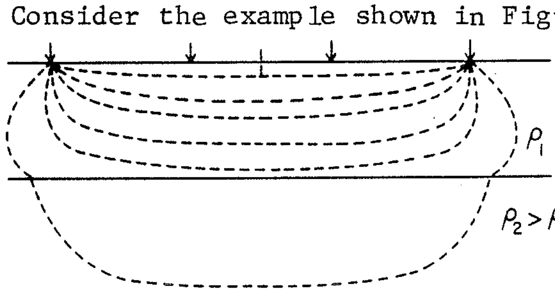

Figure 4. Current flow with resistive layer at depth.

The greater resistivity of the lower layer increases the current density in the upper layer, producing a potential drop greater than for the infinite half-space result of the top layer. Similarly, for a lower layer of lesser resistivity, the opposite is true (see Figure 5).

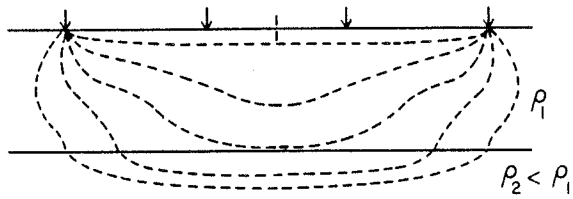

Figure 5. Current flow with conductive layer at depth.

It can be shown that the data from such simple layered case potential measurements can be easily interpreted by curve matching (20) or other interpretative techniques (eg. 3, 5, 6, 14, 19). However, the limitation in this approach is its assumption of a layered model. From research on other geometric structures (15) similar assumptions are necessary to achieve a unique solution from the inversion of the Earth-resistivity data.

Ambiguity or equivalence occurs in the solution whenever vertical or horizontal impedence boundaries are approached or crossed. The same changes in current density necessary to achieve a solution with a given model create indeterminancy in the solution if unmodelled impedance structures are excluded from the calculation. For the application of Earth-resistivity to subsurface imaging, it can be quickly realized that the results obtained depend on drilling, geologic confirmation or previous knowledge of the subsurface to produce useful information.

2.2.2 DATA COLLECTION

The Earth-resistivity technique is commonly employed in two modes of operation, sounding and profiling (see Figure 6). Sounding or the

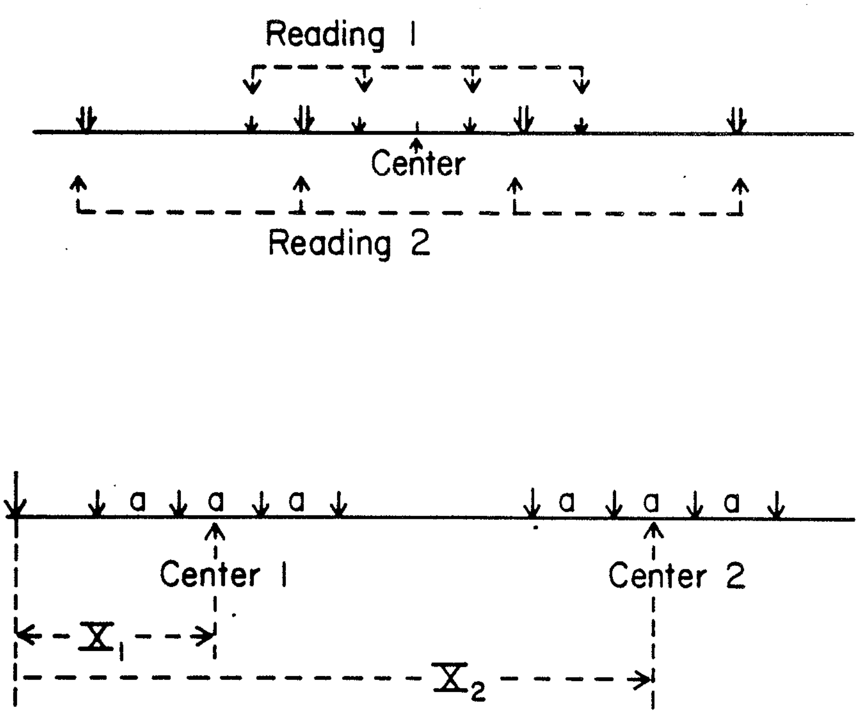

Figure 6. Sounding (top) and profiling (bottom).

identification of general layered structures, is accomplished by measuring potential drops after successively increasing electrode separation. The data are then inverted, and the resistivities, depths and thicknesses of the target layers resolved. Although this method is effective for simple geologic conditions, difficulties are encountered when horizontal impedance boundaries are crossed and not recognized.

Profiling is done by choosing a suitable electrode separation, usually after a target layer has been sounded, and moving the fixed array laterally across the terrain. The resistivity values collected may be plotted against distance to reveal horizontal changes in subsurface impedance along the profile. Data from several parallel profiles may be plotted on a map to give resistivity contours of the covered area. One should be aware, however, that the measured values are bulk or apparent resistivities and not target layer resistivities. Changes of resistivity in any layer, especially the surface layer may falsely indicate apparent changes in the target layer. Consequently, the contoured data does not represent a two dimensional image of any target layer, but merely a contour of bulk resistivity values integrated from the surface to the target layer or a depth dependent on electrode separation.

2.2.3 DATA INVERSION

Numerous techniques have been developed for the interpretation and inversion of Earth-resistivity data. The interpretational techniques consist of field plotting procedures which yield only rough and very approximate resistivity and depth approximations for most data using simple layered models. These techniques are not suitable for proper data inversion and will not be further discussed here.

Inversion techniques are solutions which provide exact depths and layer resistivities for collected data which fit the model and assumptions made. Field data which slightly deviates from the model may be fit with a loss of accuracy in the solution. Data solutions which greatly deviate from the model result in erroneous fits and equivalence problems.

Inversion techniques may be categorized into curve fitting tables and automatic computer aided inversion. The former consists of theoretical response curves of layered models (12) while the latter consists of iterative solutions based on various geometric models (3, 5, 14, 15, 19).

Partial Imaging has been attempted by using perpendicular arrays and combining soundings and profiles. Although this technique allows the calculation of more complex impedance structures, the effort required provides only partial freedom from geometric models. Automatic inversion and imaging of unmodelled impedence structures has not been accomplished with the Earth-resistivity method.(1, 14, 22).

2.3 IMPEDANCE COMPUTED TOMOGRAPHY

2.3.1 CONCEPTS

Impedance Computed Tomography is relatively new to the field of tomographic methods. X-ray computed tomography has been applied actively in medical and industrial applications to image bone structures or microfractures in steel members. Ultrasound tomography has provided a useful imaging technique for outlining the fetus in a mother's womb. Until recently, Impedance Computed Tomography was largely ignored, mainly due to its more complex theory and previous lack of working algorithms.

Impedance Computed Tomography is based on the concept that any geometric structure in the subsurface will produce unique current distributions for given electric fields injected into the subsurface. Theoretically, if a sufficient number of potential drops are measured and the necessary boundary conditions can be met, a unique solution to current distributions in the subsurface of the structure should yield an impedance image.

This approach is the reverse of Earth-resistivity inversion since sufficient data are collected to solve the impedance structure image rather than fitting limited data to a fixed model. Finding the solution, however, is more difficult than in other tomography methods. Since the current distribution inside an impedance structure is a complex function of the electric field, the current injections sites, object shapes, object location and resistivities, the simple assumption of ray-like path behaviour used in other tomographic techniques cannot be used for Impedance Computed Tomography. It is apparent that at some point in the imaging process a solution to the electric field equation must be sought. The Electroscan system and algorithm described by Wexler (20) utilizes precisely this approach.

2.3.2 ELECTROSCAN SYSTEM

The Electroscan system, when used for three-dimensional imaging from the surface, employs a square grid of electrodes set up at the surface. A current is injected through two electrodes while the potential drops at the other electrodes are measured with respect to zero. Thus, a set of measurements for the electric field over the area of interest is collected. This procedure is repeated for the same current injected through several pairs of electrodes until a sufficient number of two-dimensional, linearly independent potential measurements are collected. The impedance structure of a subsurface cube consisting of a number of blocks with each edge equal to the electrode separation on the surface grid is then solved.

The basic principle employed is that the sets of potential measurements are characteristic of the particular conductivity distribution underground. "By making a guess at the conductivity distribution, one may then calculate a potential distribution throughout the region and, in particular, at the surface. Because the guess at the conductivity is unlikely to correspond to what was actually underground when the measurements were taken, the calculated and measured surface potentials will disagree." (20) The Electroscan algorithm iteratively refines the conductivity estimate by reducing the sum of squares deviation between observed and predicted values until acceptable agreement is achieved. At this point, the actual impedence structures underground are assumed to be known.

2.3.3 ELECTROSCAN ALGORITHM

Wexler, (20), describes the Electroscan algorithm in five steps. The flow chart presented in Figure 7 may be referred to in this condensed explanation. The procedure is initialized by assuming the electric field potentials and current distribution are for an infinite homogeneous half-space.

Step (1) consists of calculating the potentials and current for a desired cube of theoretical blocks in the subsurface. The procedure involves the solution to the partial differential Poisson's equation for continuously inhomogeneous media by applying the Neuman boundary conditions.

The Neuman boundary conditions state that no current crosses the boundaries of the cube except where potential measurements are taken. Since five of the cube faces are in actual contact with the remaining subsurface region, the assumption is made that the excised region is sufficiently large in extent so that negligible current crosses those boundaries.

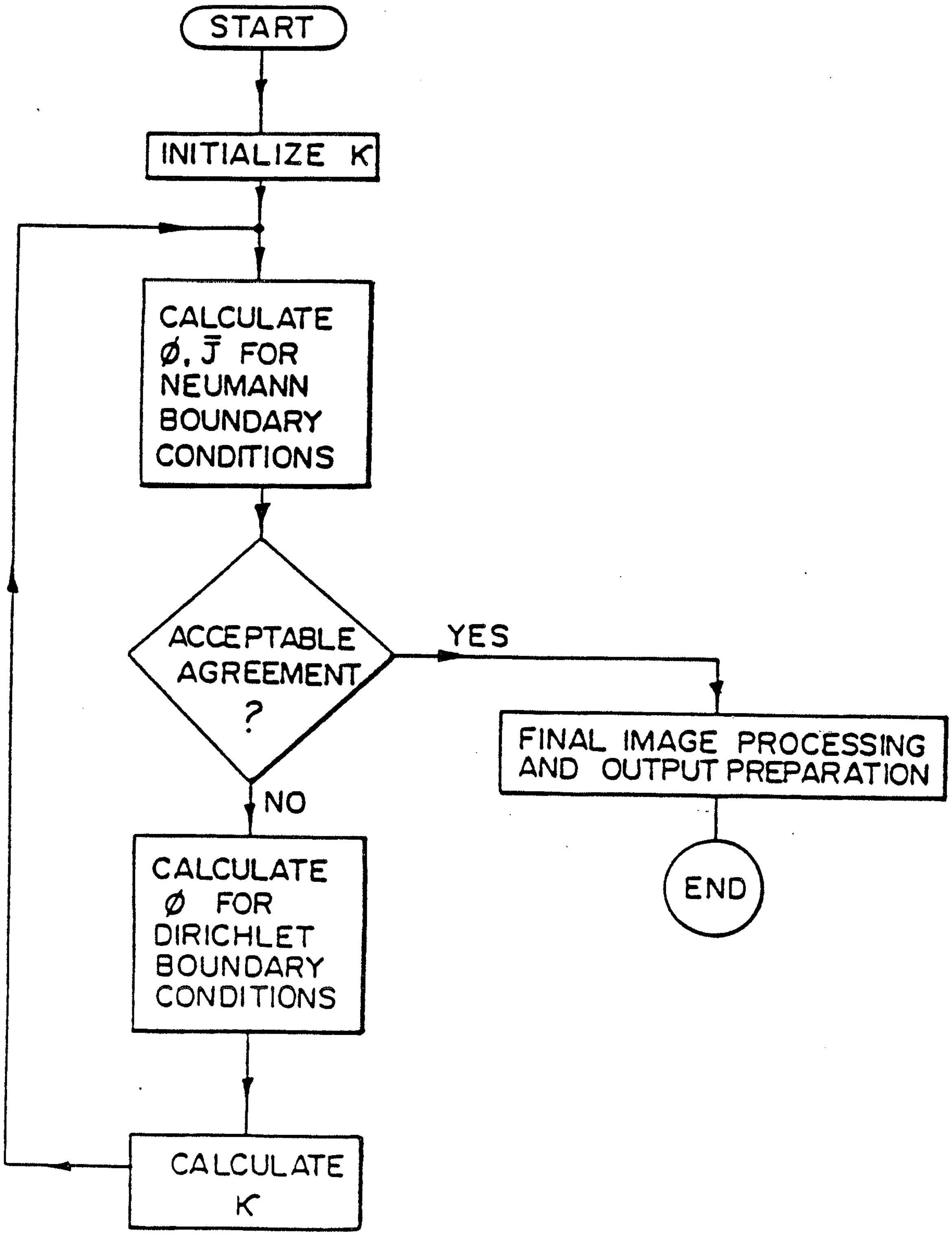

Figure 7. Electroscan flow chart, source (Wexler, 1984)

If the calculated potentials agree with those measured at the surface within acceptable limits, the result may be output. However, for the initialized conductivities this will not be the case, and the calculation passes to the next step.

Step (2) consists of potential calculations using the Dirichlet boundary conditions. The measured voltages are used to cause a change to the conductivity distribution in order to tend towards the minimization of the difference between the measured and calculated surface potentials.

Step (3) estimates the conductivity distribution such that approximate compatibility with the Neuman and Dirichlet boundary condition is attained. A least-square approach is used to produce a revised estimate of the conductivity.

Step (4). Using the conductivities calculated in the previous step, step (1) is re-initialized. In this iterative procedure, recursive improvement is achieved. If the differences between the surface potentials and the conductivities calculated are less than a pre-set tolerance, or if by experience sufficient iterations are known to have been performed, the process continues to step (5).

Step (5) consists of outputting the final image data for processing and presentation. The results consist of a calculated conductivity value for each block in the cube. Since the cube is only of mathematical and not physical depth, the number of blocks in the cube depends on the depth or level to which calculations were performed in the algorithm.

The representation of the results may consist of grey-plots for each block and level, contouring of each level, or three-dimensional relief plotting of selected conductivity blocks.

SUMMARY OF CHAPTER II

Since both the Electroscan and the Earth-resistivity methods are impedance-based electrical methods, their approach is similar but not related. The Earth-resistivity method measures only selected one-dimensional points of the electric field thus allowing for simplified visualization of the results before data reduction. The advantage is that rough estimates and interpretations can be made in the field while data are being collected. However, the inadequate method of data collection introduces the problem of equivalence during data inversion. Consequently, the Earth-resistivity method has limited potential for complete two- and three-dimensional impedence image reconstruction.

The Electroscan method uses the proper theoretical basis for attempting automatic data inversion by utilizing potential drops measured over the entire area of interest. The algorithm employed is a powerful approach to Impedance Computed Tomography. Unlike the inversion techniques used in Earth-resistivity, the algorithm solves Poisson's Equation for the electric field in a recursive iterative process using simple boundary conditions. In this approach, the problem of equivalence is ameliorated, and a complete two- and three-dimensional impedance image reconstruction is perceivable.

Chapter III

TEST AND MODEL TANK STUDIES

3.1 INTRODUCTION

This study is the first application of the Electroscan system in an uncontrolled geophysical environment. Unlike the laboratory studies, the impedance structures to be imaged are unknown; therefore, it seems worthwhile to review the experiments and previous studies to gain a better understanding of the results which may be obtained with the Electroscan system.

The review can be divided into three studies: those conducted by Wexler et al. for the publication in reference (20), those subsequently conducted by Mandel (11) (B.Sc. thesis), and those by Allard (2) (B.Sc. thesis).

3.2 WEXLER, FRY AND NEUMAN STUDIES

Wexler, Fry and Neuman included mainly computer simulated as well as potential measurements for two-dimensional imaging. The potential measurements were conducted in an acrylic test tank. A layer of water was used as the conductive host medium and objects were placed into the tank. Measurements were taken through 64 electrodes along the tank periphery only. As shown in Figure 8, 44 electrodes were used while the remaining served as current injection sites. Since each side of the tank features 16 electrodes, 256 logical blocks are formed. It was found that, in general, the number of measurements required to image the region had to equal or exceed the number of blocks to find a unique conductivity value for each.

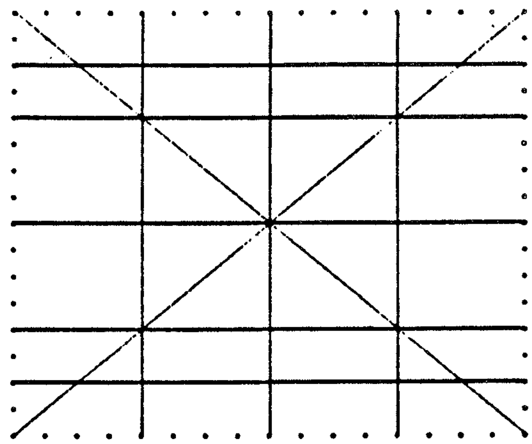

Figure 8. Ten excitation patterns for the two-dimensional case

Figure 9 shows a step function model which was imaged using computer simulated measurements processed by the Electroscan algorithm. In the relief plot shown, the sides appear as steep slopes rather than steps; this, of course, is due to the coarse block units used. Reconstruction of the step function is shown for several stages in the iteration of Figure 10. It may be clearly seen that successive improvement of the image occurred with increasing iterations.

Wexler, (20), mentions that for excessive iterations, (1700), an oscillatory response occurred. Also, a definite edge effect exists -- the sides and top of the step functions were imaged as sloping faces. However, a competent image was reconstructed.

Convincing results were also obtained using measurements in the acrylic test tank. A plastic jug and a metal cannister were placed in the host medium (water). In Figure 11, the imaging process clearly reproduced a rough outline of the metal can and the plastic jug in the

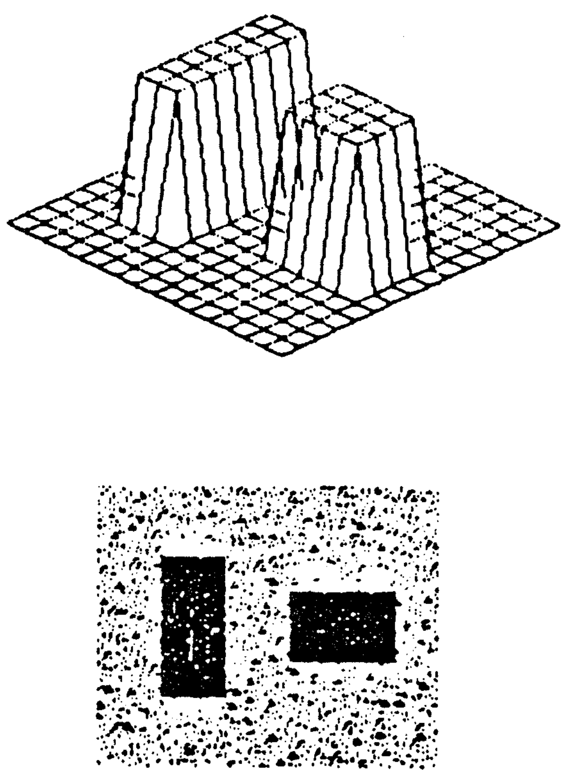

Figure 9. Relief and density plots of step function, source (Wexler, 1984)

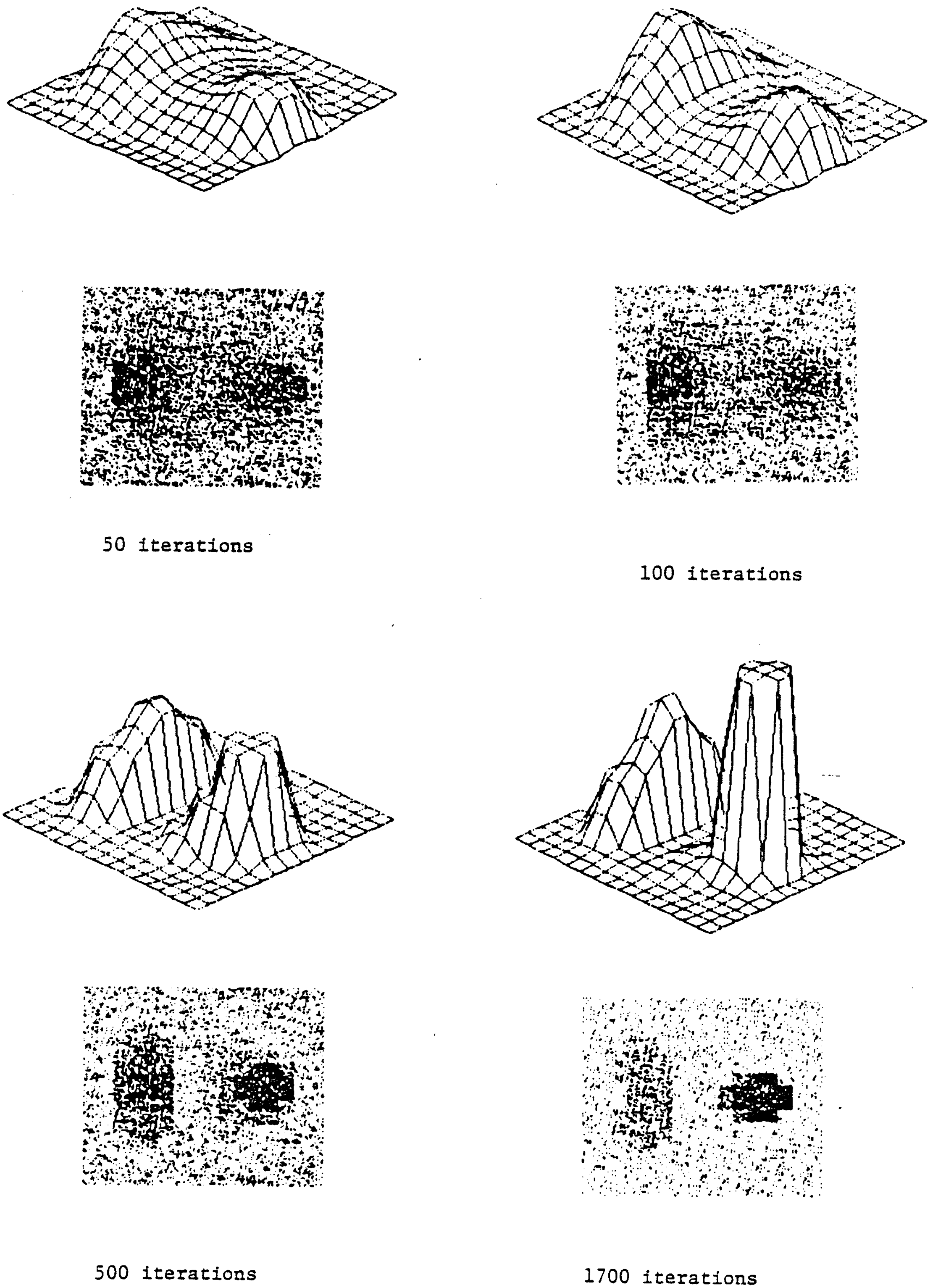

Figure 10. Relief and density plots of step function image, source (Wexler, 1984), (conductivity ratio 5:1)

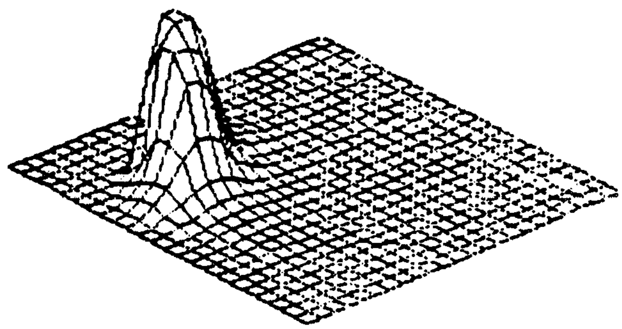

(a)

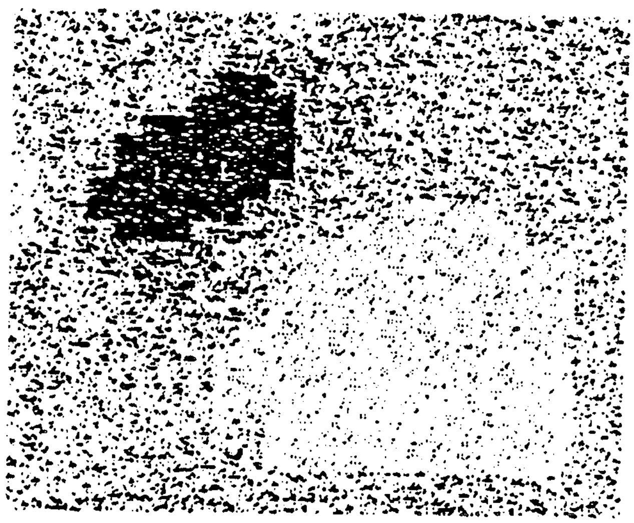

(b)

Figure 11. Relief and logarithms density plot of tin can and plastic jug image in test tank, source (Wexler, 1984).

density plot (note that on the density plot the plastic jug depression is more clearly visible by using the logarithmic display method).

Finally, simulated data were used for the subsurface model of a conductive box by using surface measurements only. The box was modeled in the centre of the subsurface host medium cube to be imaged. The algorithm was then used to process the simulated surface measurements by assuming four layers in the cube with the box present in the middle two. Although the image improved with more iterations, the image was not fully reconstructed after 1700 recursions. The second layer clearly showed the box while the third layer showed only an elevated conductivity. It thus appears that the image patterns evolve from the top and migrate down, and a large number of iterations are required. Further, a conductivity "shadow" was present on the fourth layer which, in the model, did not contain the box.

3.3 MANDEL'S THESIS

Mandel, (11), continued the three-dimensional subsurface imaging study by processing physical measurements. A grid of 64 electrodes in an 8x8 array was used to image the subsurface region. The region was divided into finite elements or blocks for which the conductivity was calculated (Figure 12). Since the maximum number of blocks for which the conductivity can be calculated is determined by the number of measurements taken, only three, four or five layers of blocks were usually calculated.

Several excitation patterns were tried to achieve a good current distribution for all current injection pairs used. The excitation pattern of Figure 13 produced suitable results and was used for the Mandel,

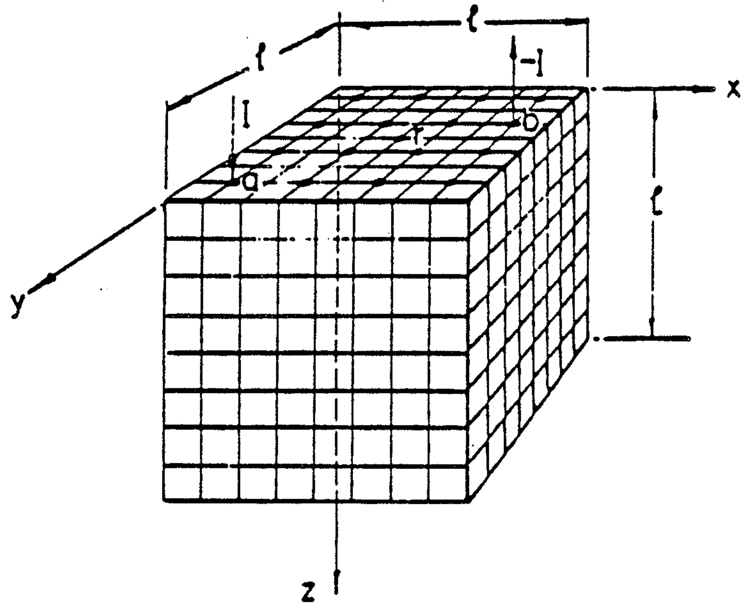

Figure 12. Subsurface cube showing levels of blocks, source (Wexler, 1984).

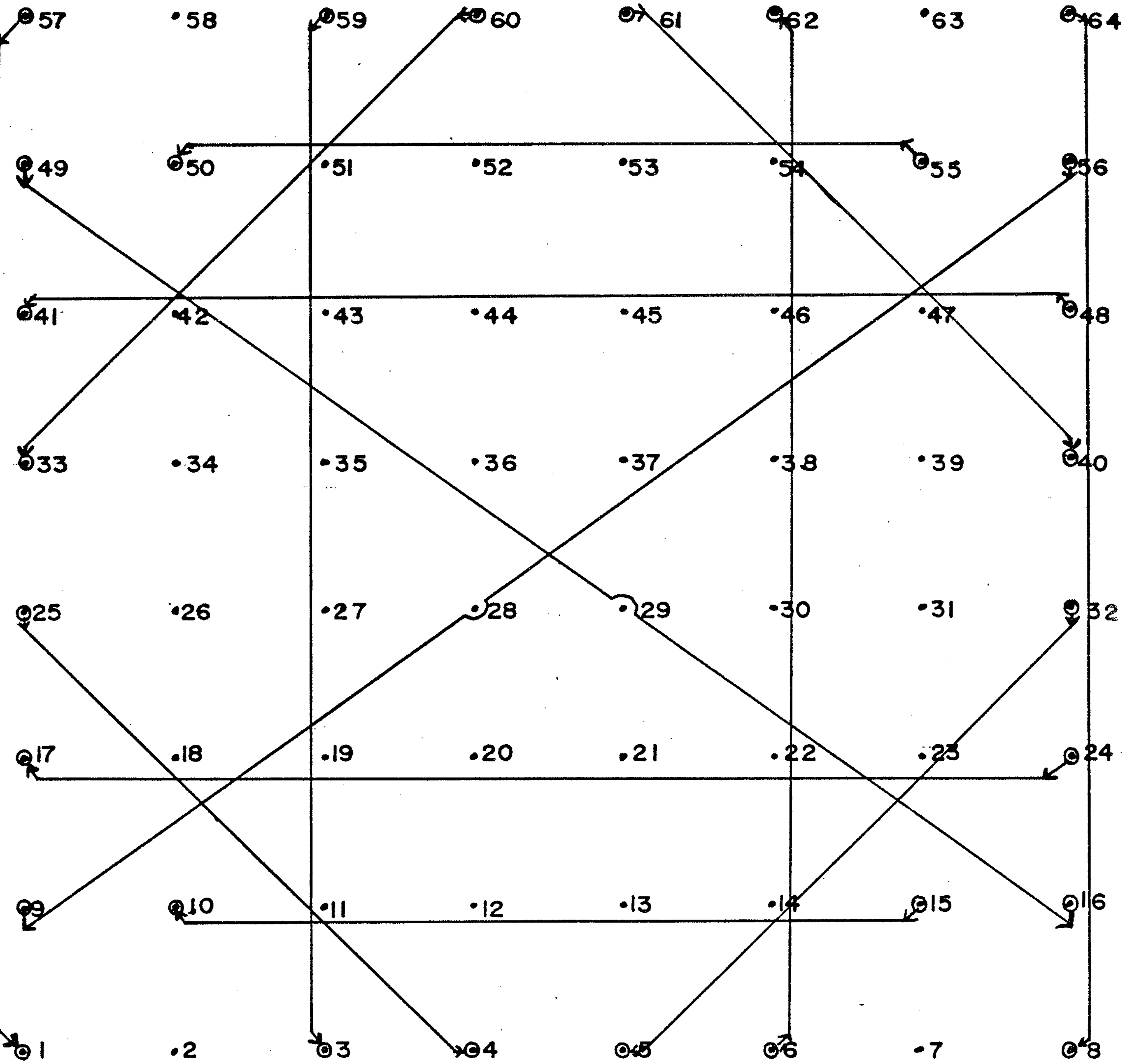

THREE DIMENSIONAL ELECTRODE ARRANGEMENT 8x8 ARRAY

• POTENTIAL ELECTRODE (36 of)

INPUT (14 of) / OUTPUT (14 of) — CURRENT ELECTRODE PAIRS

FIGURE 13.
by U. Roeper 1985

and Allard theses, and this study.

For the representation of the results, Mandel used grey-plots for each level of blocks, as well as, numerical array results for each block. Figure 14 shows the image of a plastic cube placed in the N-W corner of the test tank. A rough outline (black) is visible of the low conductivity object in the host medium. However, since only eight grey levels are available, discrimination of blocks is difficult.

Useful conclusions about the behaviour of the algorithm can be obtained from Mandel's results. For the plastic cube mentioned, the tank was filled with the host medium to five block layers. The cube was submerged to a depth of 1.6 blocks under the surface. The resulting images show that the impedance shape of the cube deteriorates in levels 4 and 5 of the figure. Furthermore, irregularities in the conductivity of the host medium have been calculated which do not exist.

Mandel also points out that all experiments showed discrepancies in the top layer. Since this phenomena is seen only in the physical measurement studies and not the simulated data, the problem was traced to an inaccuracy in the measurements at the surface boundary layer. The conductive "shadow" observed by Wexler (20) was again present beneath objects of high conductivities. In an experiment with a highly conductive steel mortar shell submerged in water, horizontal "shadows" were also present.

Generally, it was noted that the image quality increases with iterations, with an optimum being reached between 40 to 120 iterations. Much higher iterations cause the image to deteriorate. Also, imaging the same object to three, four or five layers had little effect on higher layers. Lastly, all tests performed produced images of acceptable to good quality.

Level 1

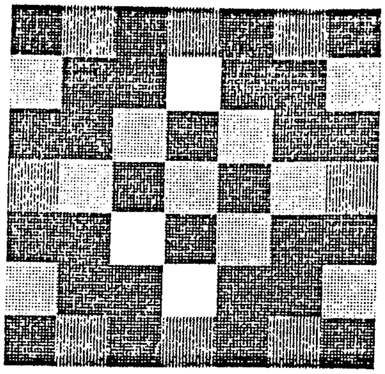

Level 2

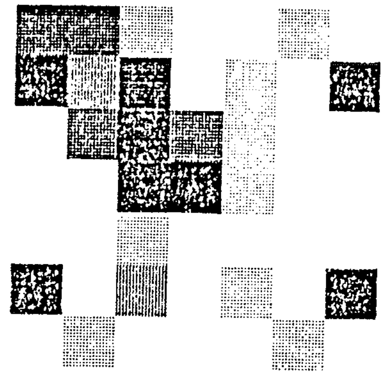

Level 3

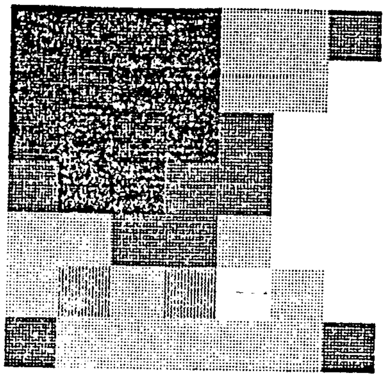

Level 4

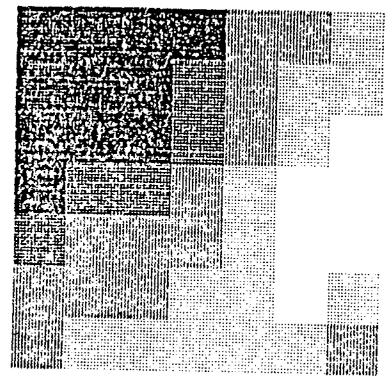

Level 5

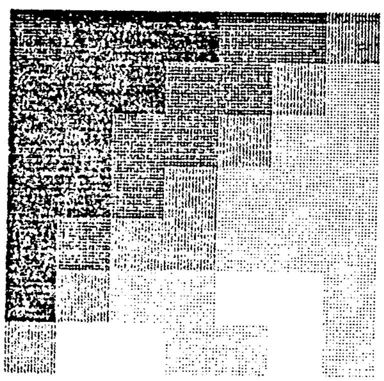

Levels							
	88	132	74	97	78	131	87
	139	91	40	182	34	87	139
	83	92	159	27	168	79	85
	98	154	28	138	20	157	100
	81	78	176	17	160	66	81
1	141	92	28	217	28	83	140
	87	127	77	103	78	125	87
	204	203	288	399	686	286	307
	91	225	132	573	261	477	153
	706	201	145	222	302	381	1472
	358	356	152	54	288	671	689
	1345	344	270	310	339	377	1531
2	140	459	239	769	258	507	146
	308	294	590	446	646	297	310
	92	117	120	170	260	305	213
3	125	107	137	156	272	256	310
	131	140	132	146	222	326	330
	207	173	147	175	221	334	443
	247	258	210	200	261	340	326
	270	242	295	241	317	261	310
	202	295	260	266	276	305	212
	79	88	107	130	175	206	226
	84	100	111	141	181	229	231
	106	113	130	160	204	238	268
	127	142	161	184	226	257	270
	159	175	197	216	239	253	266
4	187	221	218	233	235	251	227
	216	227	245	235	241	227	220
	86	114	120	124	140	172	212
	93	114	130	144	169	201	231
	94	119	144	170	199	223	231
	98	129	165	198	223	235	232
	107	151	193	222	240	244	231
5	132	192	228	238	248	247	234
	207	263	256	246	246	255	230

Figure 14. Plastic cube image, source Mandel 1985. Computed to five levels after 80 iterations.

3.4 ALLARD'S THESIS

Allard, (2), conducted experiments in an aquifer test bed. This set-up consisted of a 6.25 m x 2.5 m x 0.45 m sand bed placed on a concrete floor and surrounded by rigid side walls. To make the experiment dynamic, a flow field of fresh water was allowed to seep through the sand.

Using salt solutions, various plumes (slugs and continuous injection) were imaged. The grid used consisted of a 64 electrode grid with a block size of 0.1 x 0.1 x 0.1 m. The image calculations were carried out to a depth of four and five block levels. Regrettably, the fifth level images only to a depth of 0.5 m (theoretically) and, therefore, no deductions at greater depths were made. This would have been of considerable interest in evaluating the shadow effect and the systems response to the layered case (ie. saturated sand overlying concrete).

Nevertheless, consistently useable images of the plumes were imaged. Figure 15 shows an example of a salt solution injected at the top left corner of the grid. After time, measurements were made and the data was imaged with the Electroscan algorithm. An impedance plume, small and concentrated in level two and wider but less concentrated is resolved in the lower levels along the left side of the grid.

As noted earlier, the discrepancies encountered in the top layer were again present in these experiments; clearly the surface layer discrepancies are a characteristic of the algorithm. Also, it was noted that "symmetrical" shadows were produced around the edges of each level. These were attributed to edge effects due to the absence of acrylic tank walls to confine the current flow paths. However, the plume images could be easily distinguished from the secondary conductivities of the shadows.

LEVEL 1

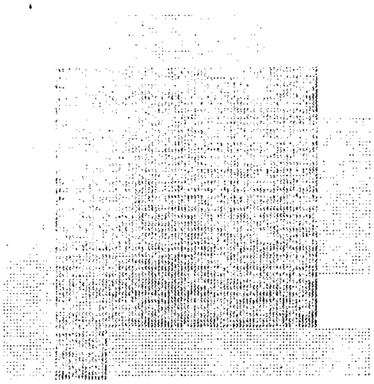

LEVEL 2

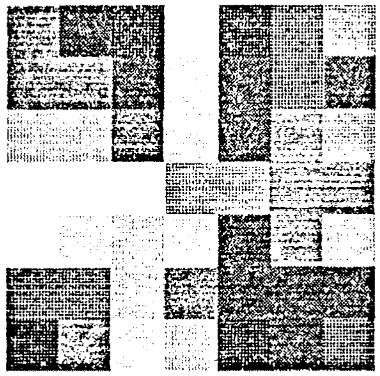

LEVEL 3

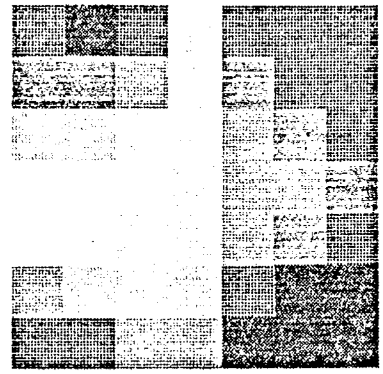

LEVEL 4

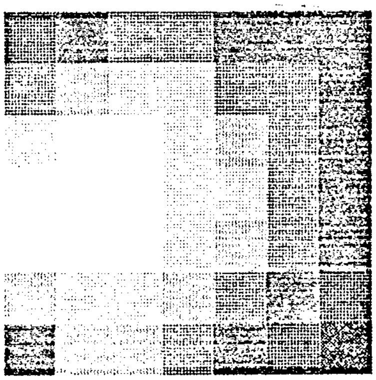

LEVEL 5

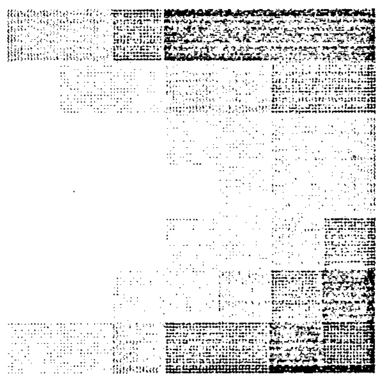

67	65	34	41	32	57	68
71	10	10	10	10	10	66
40	10	10	10	10	10	42
61	10	10	10	10	10	48
38	10	10	10	10	10	35
32	10	10	10	10	10	53
44	10	39	40	26	38	55

57	42	23	135	25	47	76
68	69	60	112	51	51	33
127	150	135	310	59	67	68
769	478	773	260	142	58	59
565	287	219	244	45	70	73
42	46	151	71	31	35	20
10	61	160	87	11	32	42

53	45	62	99	56	53	55
77	72	114	187	83	58	60
166	192	302	281	133	80	60
661	720	558	417	147	98	70
390	470	374	224	115	73	57
92	136	169	158	57	37	36
46	61	105	87	37	29	30

59	69	94	98	80	70	65
104	140	209	189	125	92	72
278	352	421	337	195	120	87
559	579	563	393	233	131	88
431	444	440	326	177	103	72
176	223	254	181	103	67	48
80	125	145	106	65	47	39

129	117	103	92	86	83	80
367	292	240	193	153	125	107
574	483	421	327	238	169	121
592	563	514	402	279	182	118
475	482	438	333	232	152	98
339	325	275	206	148	106	75
183	178	144	110	88	73	55

Figure 15. SW-Slug image, source (Allard 1985). Computed to five levels after 80 iterations.

3.5 SUMMARY OF CHAPTER III

A considerable number of experiments were conducted by Wexler et al., Mandel and Allard. The images produced for two- and three-dimensional cases with simulated and measured potential are promising. Those images based on simulated data have shown that a sloping effect is introduced by the algorithm along sharp conductivity boundaries. Mandel's thesis indicates that the top layer of the image shows considerable discrepancies between observed and expected values. This was attributed to measurement inaccuracy. Also, after an optimum number of iterations are performed (40 to 120), the image deteriorates. Allard's work showed that unexplained symmetric shadows may appear in experiments in which the insulating walls are removed. However, acceptable images were obtained in these experiments which strongly reflect the impedance structures to be resolved.

Chapter IV

GEOLOGY AND SITE HISTORY

4.1 INTRODUCTION

During the course of this field study at Portage La Prairie, a considerable amount of information was gathered on the geology pertinent to the landfill. It became readily apparent that although a good regional understanding of the geology had been documented, a thorough knowledge of the George Lake area did not exist.

In this Chapter, the geologic and hydrogeologic data for this area were compiled and complemented by a careful site investigation and interpretation.

4.2 PORTAGE AREA GEOLOGY

Much of the Portage area, including the George Lake oxbow is situated on the alluvial outwash fan formed where the Assiniboine River flows into the Manitoba Lowlands. In general, this area consists of Lake Agassiz basin clays overlain by several meters of alluvial outwash sands and floodplain silts. To the west, the area is bordered by the ancient Assiniboine Delta as shown in Figure 16.

A study conducted by Wolowich and Tamburi (21) shows that sediments are eroded out of the delta sands by a classic back-cutting action of the Assiniboine River (Figure 17) and deposited again on the alluvial fan. It was noted, due to the high sediment load, that extensive sandbar formation occurs along this reach of the river causing rapid aggradation, flooding (controlled since 1969 by the Portage Diversion Dam), and unstable meander activity.

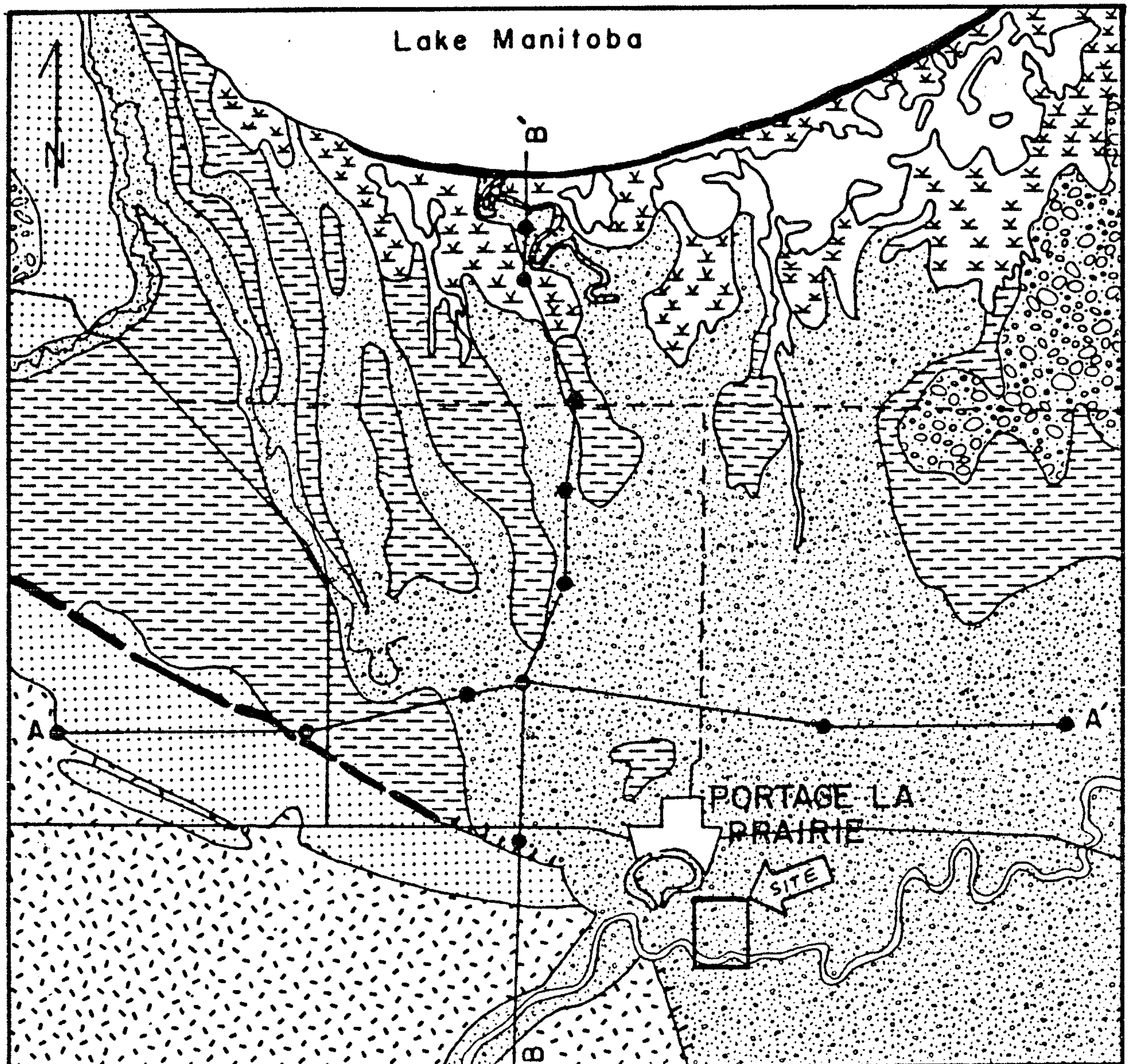

FIGURE 16. PORTAGE AREA GEOLOGY

SCALE 1:200 000

Age Unit

Recent

Beach

Marsh

Alluvial

Pleistocene

Strandline beach

scarp

Deltaic sand

Offshore silt

clay

Till

from M. FENTON 1971

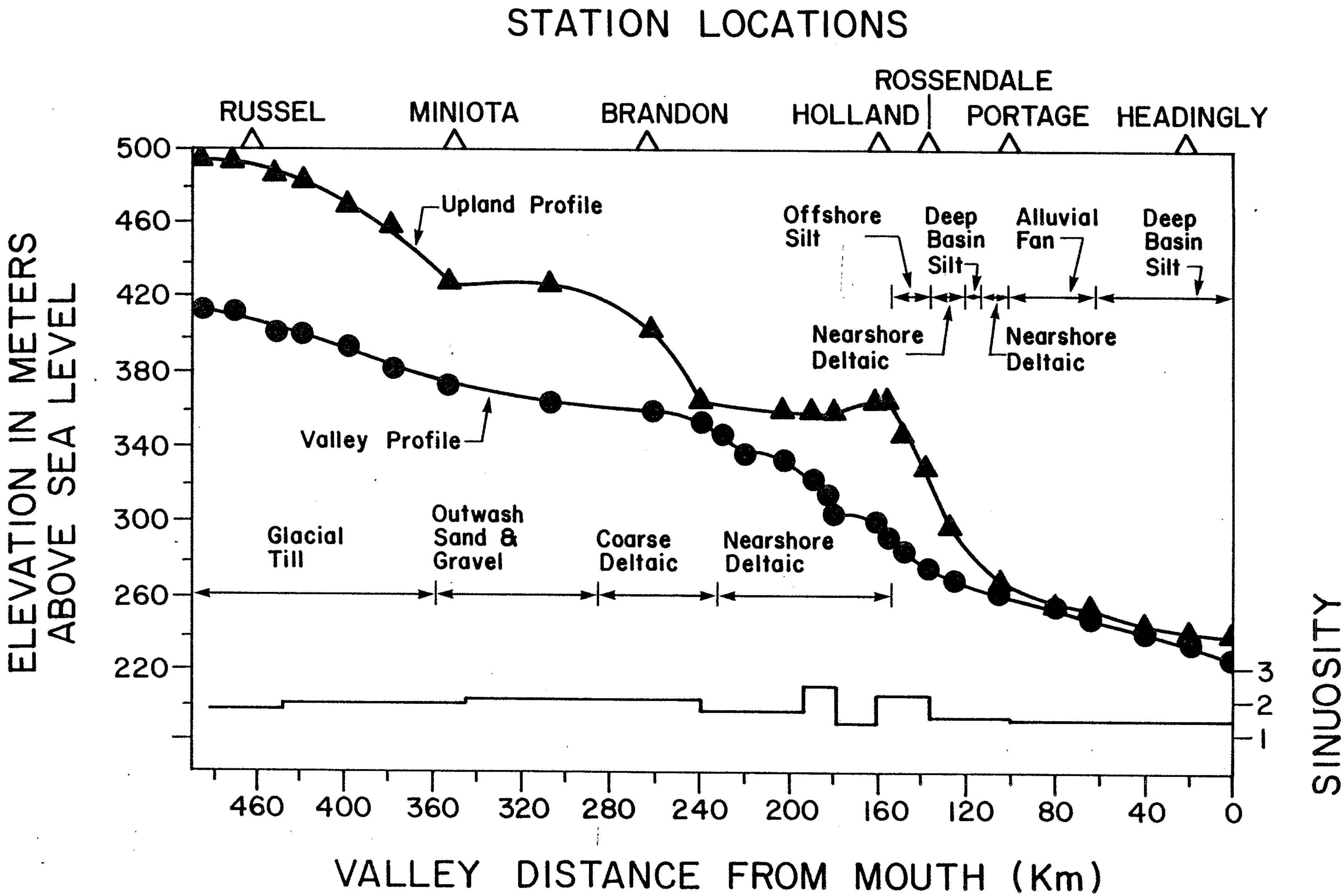

Figure 17. River slope, source (Wolowich & Tamburi, 1985)

Figure 18 presents the alluvial geology and meander activity in more detail. Gilliland (9) reports that during earlier periods of aggradation on the alluvial fan, water flowed north into Lake Manitoba, not east to the Red River. Accordingly, much of the area around Portage La Prairie features a thick blanket of alluvial sand, overlain by extensive floodplain silts and clays.

Gilliland divides the alluvial activity into early and late channel; as can be seen from Figure 18, George Lake is a late channel deposit. In this study, it became apparent that the late channel deposits could be further divided into meander phases. A detailed air-photo interpretation showed that the sweep of the meander loops could be identified for the later deposits.

Figure 18b gives a detailed visualization of meander movement in the late deposits. Phase 1 represents the earlier meanders of the late deposits while Phase 2 is the more recent activity of the Assiniboine River. From this interpretation, it was deduced that the George Lake area was reworked at least twice by the late meanders.

It was also noted that the George Lake oxbow features an overly sharp curvature and excessive sandbar formation on the west limb. This oxbow is clearly deformed indicating material (clay), much more resistive to erosion, prevailed east of the meander.

4.3 SITE HISTORY

The present landfill, as shown in Figure 19, completely covers about five hectares of the north bend of George Lake. The total height of the waste and fill above grade is approximately 15 m on the south ramp.

Floodplain silts are excavated in a borrow pit on the meander flat as cover and fill material for the landfill operation. A small tributary

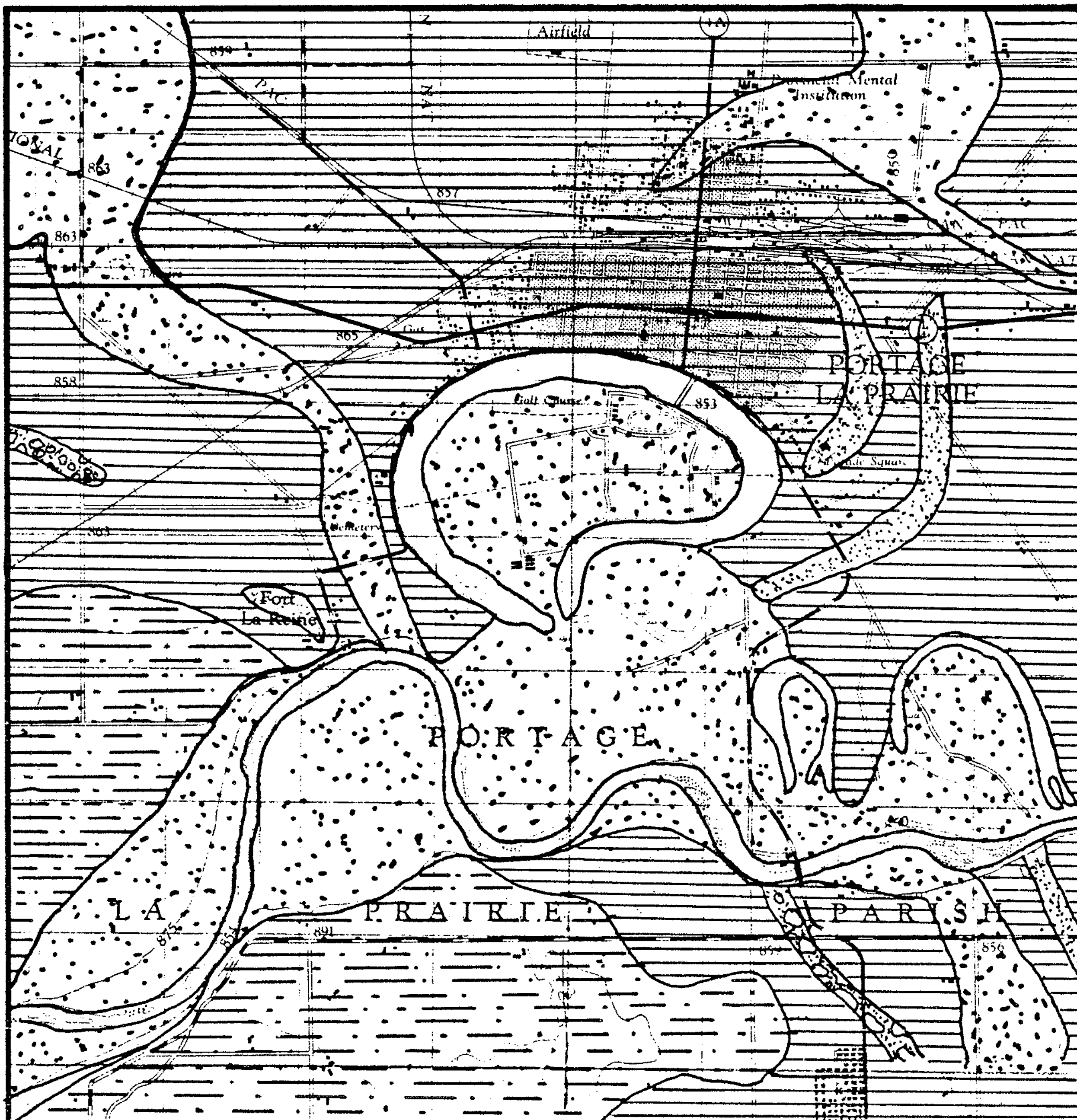

FIGURE 18. GEOLOGY AND MEANDER ACTIVITY

LEGEND

after J. GILLILAND 1965

- FLOODPLAIN SILT
- EARLY CHANNELS
- LATE CHANNELS
- AEOLIAN LACUSTRINE SAND
- BEACH RIDGES

Scale = 1:50000

by U. Roeper 1985

FIGURE 18B

GEOLOGY AND MEANDER ACTIVITY

by U. Roeper 1985

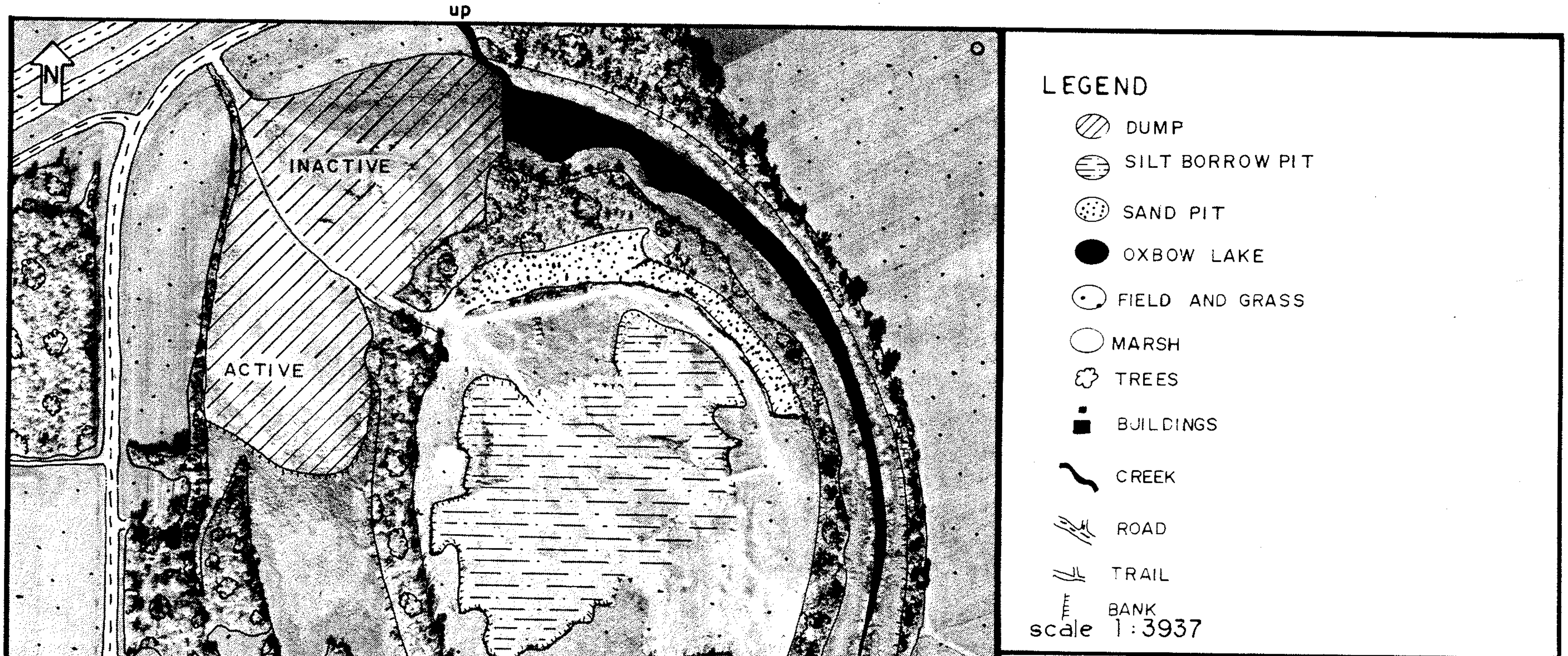

FIGURE 19.

SITE PHYSIOGRAPHY

by U. Roeper 1985

drains into the oxbow lake in the east limb. Along Provincial Road 242, which leads south past George Lake, 26 private residences draw water from shallow wells set into the alluvial sands.

In 1984 and 1985, two consulting studies (17, 18) were concluded for the Province of Manitoba. It was reported that in at least some of the wells, leachates from the landfill were contaminating ground water.

This landfill has been operating in its present location since the 1930s. To assist in the understanding of the site, recent and historic air-photos of the site were compared. Figure 20 shows the George Lake area in 1948 and 1979. It should be noted that in 1948, waste and fill were deposited directly into the oxbow lake which at that time covered most of the north bend. It was confirmed with an older resident in the area that during floods (before construction of the Portage Diversion Dam in 1969), the meander limbs would be flooded with water. Clearly, it may be assumed that early contaminants from the disposed waste were carried throughout the oxbow by advection in open water, particularly those areas covered by the oxbow lake.

4.4 HYDROGEOLOGY

The hydrogeology of the area may be best understood by examining the groundwater level contours in Figure 21 (reported by Gilliland (9)). It is evident that in the Assiniboine Delta deposits (southeast part of figure) a steep and well-defined hydraulic gradient follows the topography and the river valley. On the alluvial fan, groundwater flow direction becomes more ill-defined. It appears that some gradients follow the direction of the river while a general flow off the alluvial fan is evident. Tamburi

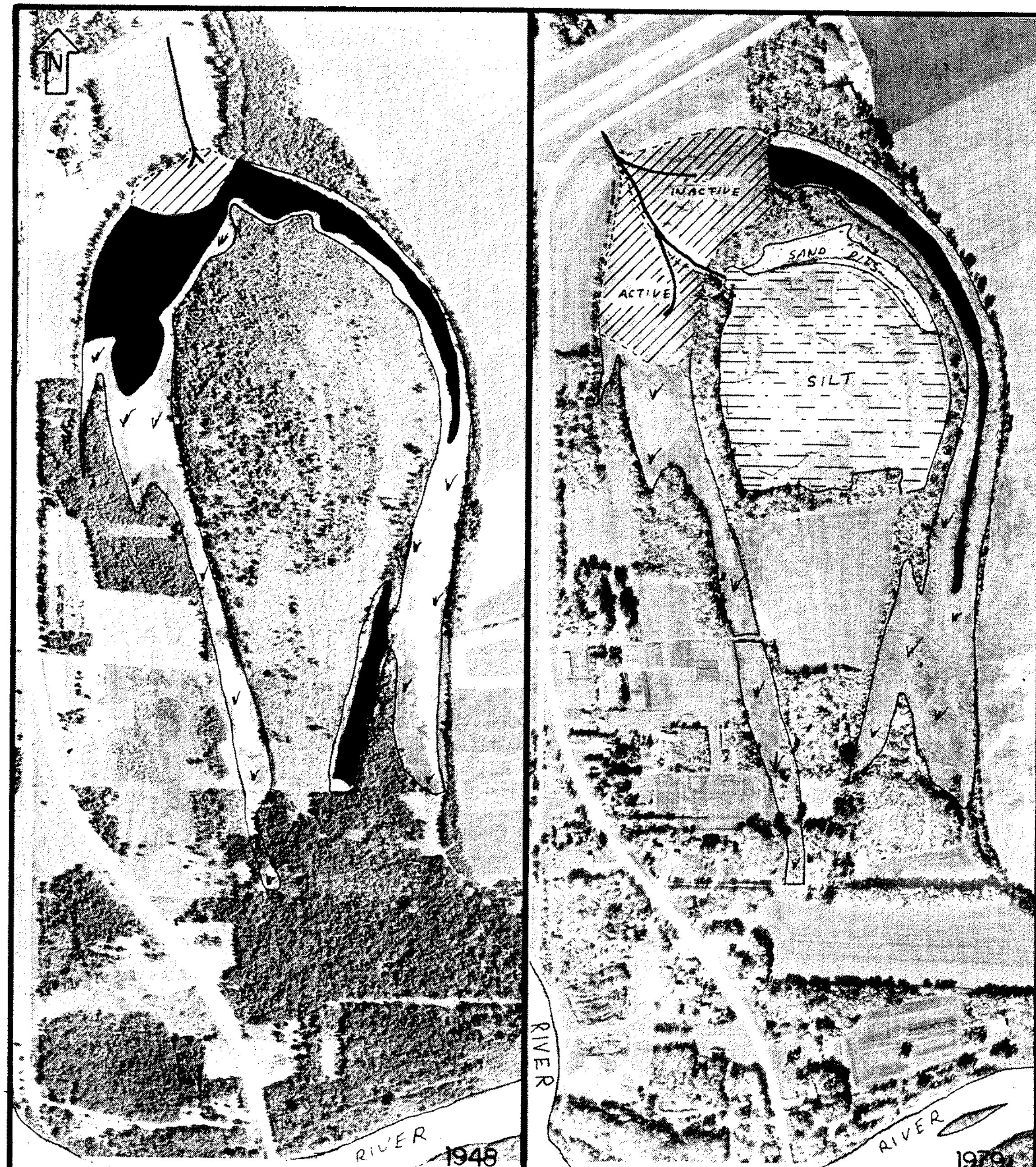

LEGEND

DUMP

SILT BORROW PIT

OXBOW

OXBOW LAKE

scale 1:7874

FIGURE 20.

SITE HISTORY AND EXTENT OF OPEN WATER IN GEORGE LAKE IN 1948 AND 1979

by U. Roeper 1985

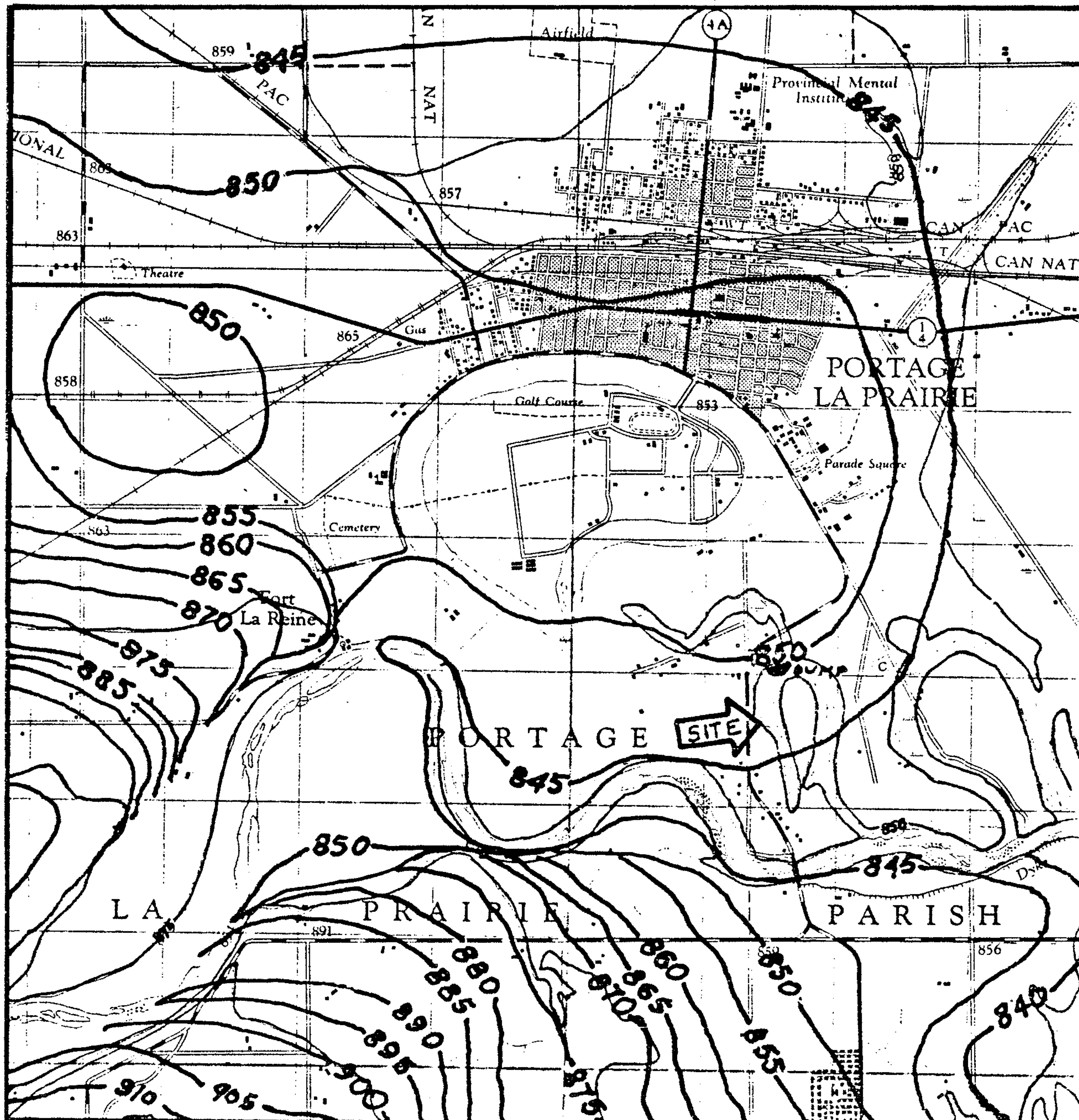

FIGURE 21. TOPOGRAPHY AND WATER LEVELS
(U. Roeper 1985)

SCALE = 1 : 50 000

DUMP

ELEVATION (Feet)

WATER LEVELS (Feet) from J. Gilliland 1965 (oral, 1985) suggested that the groundwater flow field for this area had not fully adjusted to the numerous changes in river flow direction. A gradient from an old channel at Portage La Prairie through the site south to the Assiniboine River exists.

Figure 22 shows groundwater contours interpreted from water levels reported by Slaine (17). In this more detailed approach, it becomes clear that steep local gradients exist near the landfill, flattening south towards the river. It appears that the elevated waste mound has a significant topographic effect on the groundwater gradients near the landfill.

Since coarse, permeable sands are underlain by lake basin clays, and overlain by less permeable floodplain silts, the majority of the groundwater flow is expected in the sand unit.

4.5 OXBOW GEOMORPHOLOGY

One of the major impedance structures in the subsurface are the resistive dry sandbar soils. Extensive sandbar formation occurred in the meander before the cut-off. Figure 23 shows some of the more prominent sandbars identified from the air-photos. It is interesting to note that the residual channel is considerably wider in the north bend. Consequently, the channel depths should be deeper in the narrow part. in the narrow part. This, however, would result in only a minor difference in depth after the cut-off occurred since the thalweg would normally slump and collapse or undergo progressive infill. Only a slight difference in grain size should be expected; impedance structure should not change.

Using the drill logs of the Province of Manitoba monitoring wells, a general cross-section of the oxbow was constructed (Figure 24). On

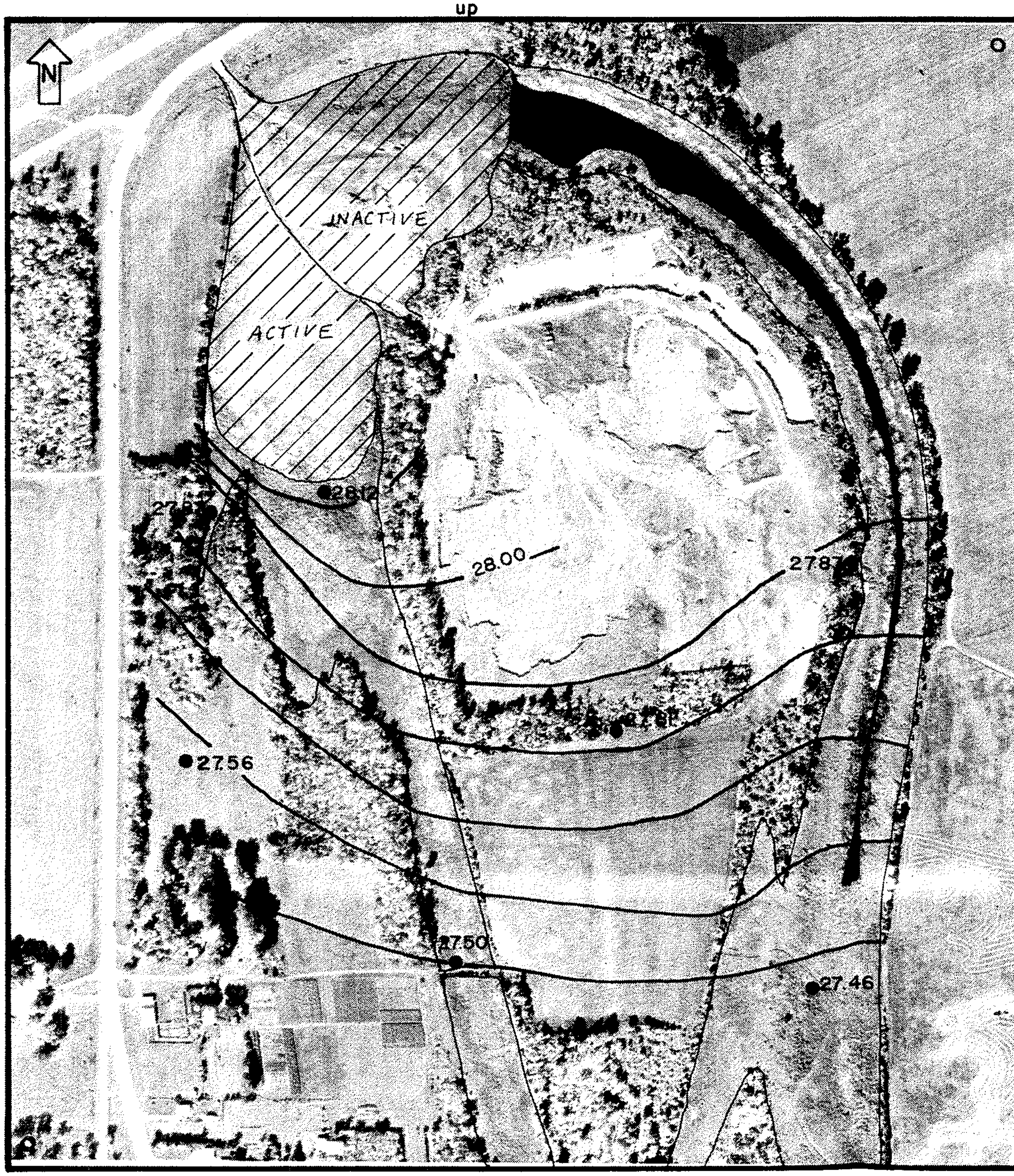

LEGEND

DUMP

WATER

OXBOW

● PROVINCE OF MANITOBA MONITORING WELL

27.50 STATIC WATER LEVEL 20.11.85
BY G.L.A.
ELEVATIONS UNREFERENCED METERS

scale 1 : 3937

FIGURE 22.

GROUND WATER LEVELS

by U. Roeper 1985

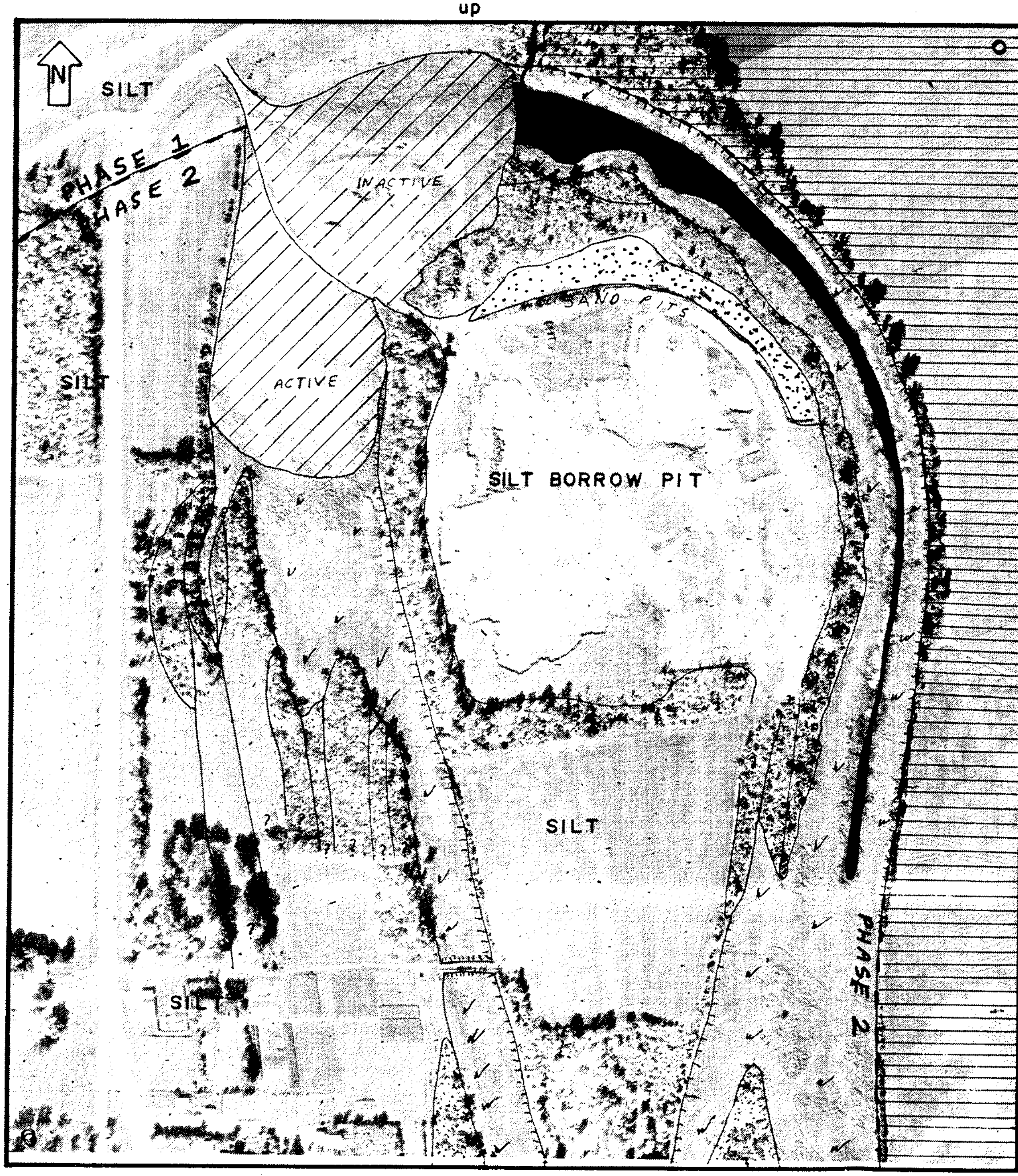

LEGEND

- DUMP
- FLOODPLAIN
- RECENT SILT
- OXBOW LAKE
- OXBOW
- COARSE SAND (RIVERBED)
- FINE SAND (SANBAR)

scale 1: 3937

FIGURE 23.

INTERPRETATION OF REMNANT GEOMORPHOLOGY

by U. Roeper 1985

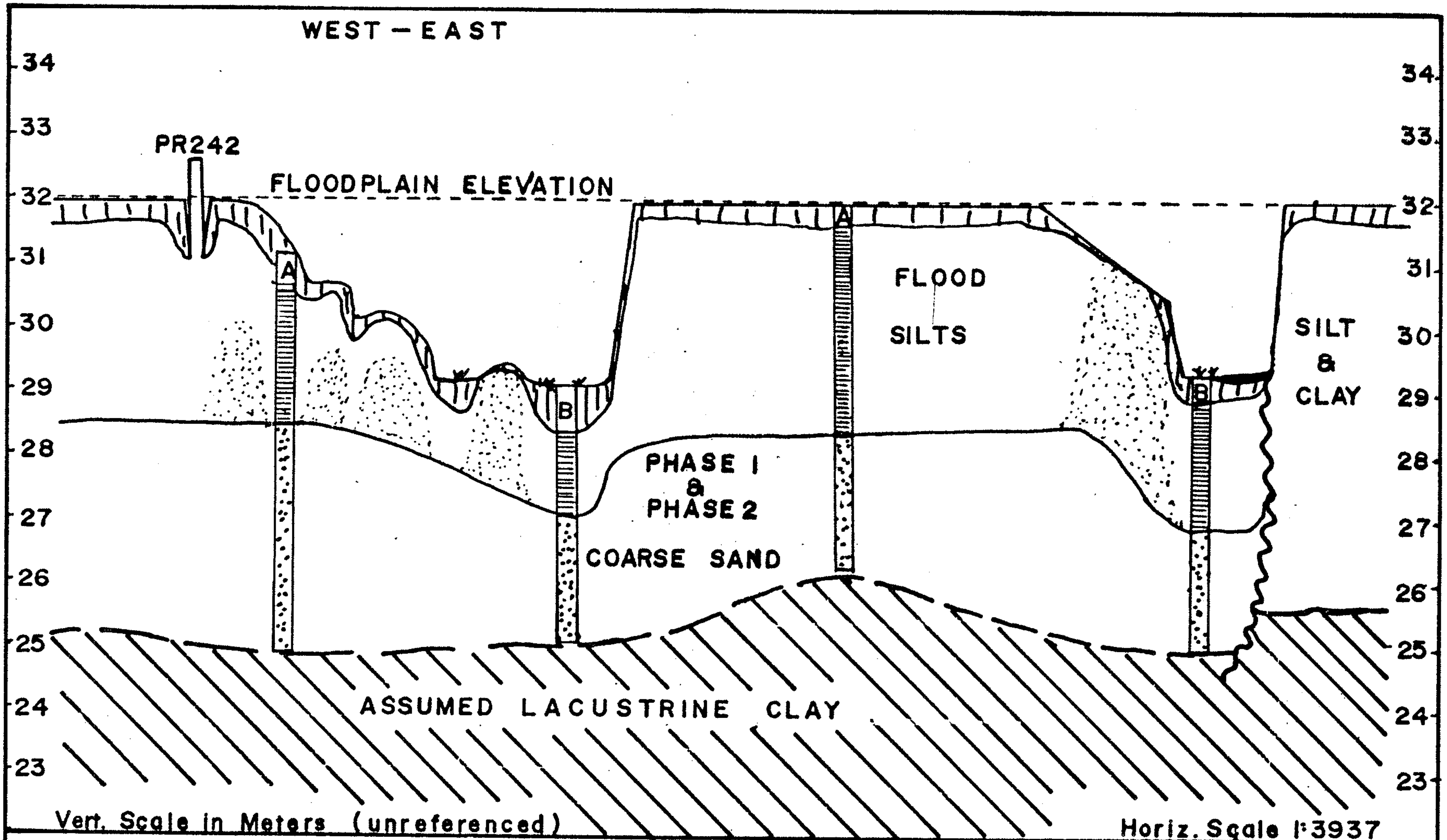

FIGURE 24. GENERAL CROSS–SECTION OF OXBOW

A – SILTY TOPSOIL

B – BLACK ORGANICS

SANDBARS

MEANDER EDGE

EROSIONAL BOUNDARY

by U. Roeper 1985

the east side of the oxbow, a silt and clay boundary was drawn in to represent the inerodable material discussed in Section 4.2. It is not clear if these deposits extend down to basin clay or if a thin layer of early sand underlies them.

The cross-section clearly shows how floodplain deposition occurred at a much slower rate than the erosion of the west limb. The east limb was in position for a considerable length of time since aggradation is nearly complete.

In the channel, the silt infill is of greater thickness than the rest of the depositional area. This feature is believed to be characteristic of the cut-off process. During normal progression of the meander loop, most of the thalweg is infilled with bedload sand on the point bar side; during the cut-off, silt or very fine sand infills the channel.

The composition of the silt should be essentially the same in the channel and in the floodplain except for small differences in grain size. However, some organics, peats and swamp soils (all reducing environments in nature) may form during prolonged periods in those areas covered by the oxbow lake. As impedance structures, the silt may show significant increases in conductivity with increased moisture content; the organics, if saturated, may be extremely conductive.

Sandbars (Figure 25) are of saturation-dependent conductivity. The dry sands near the surface are of high resistivity, as mentioned. With pollution, the conductivity is dependent on both saturation and ion concentration. Saturated with clean water, the conductivity of the sandbar will be less than silt; saturated with leachate, the conductivity will be greater.

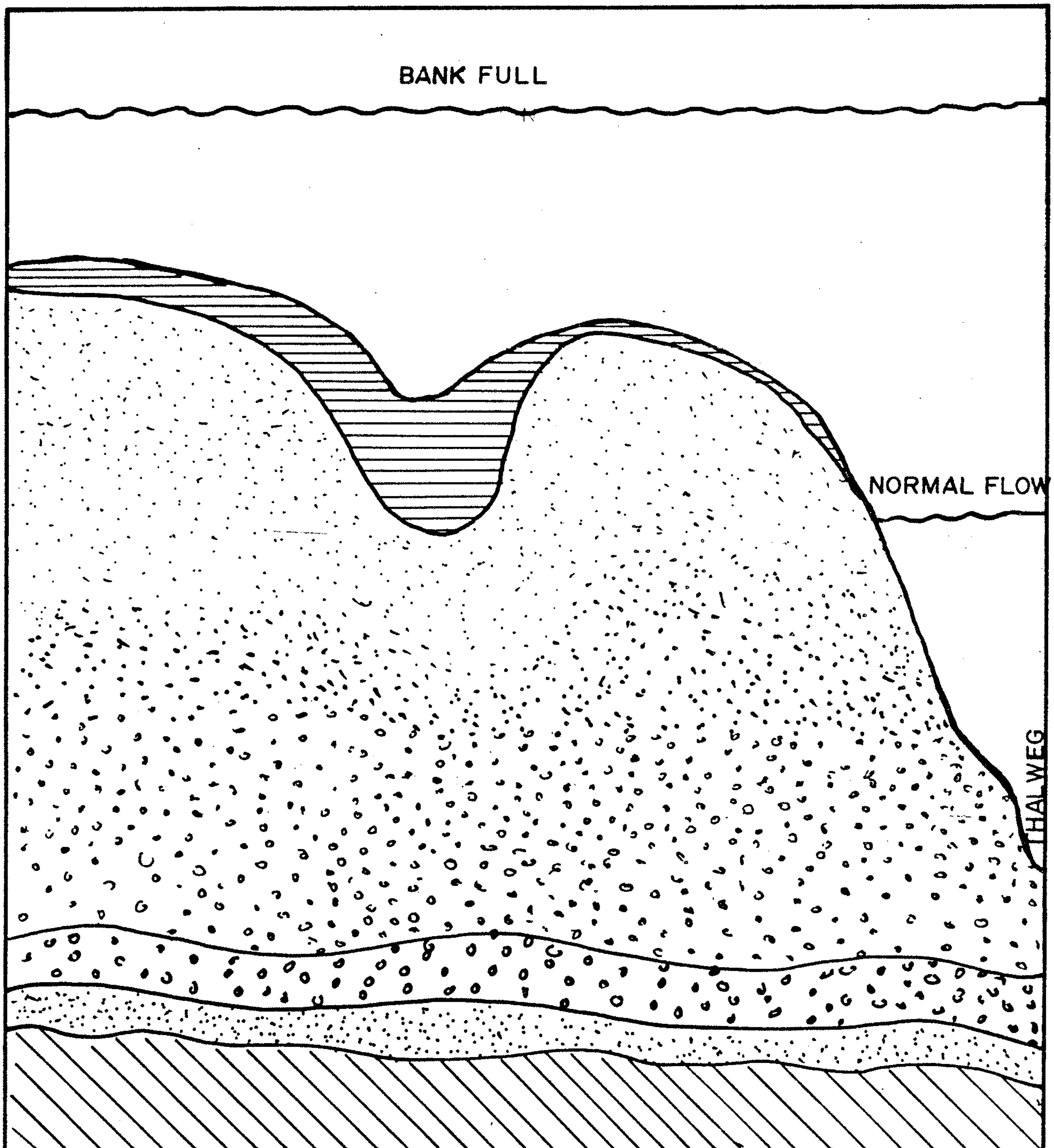

FIGURE 25. SANDBAR AND SUBSTRATA

SILT

SÁNDBAR (FINING UPWARDS)

PHASE I SAND (IF PRESENT)

AEOLIAN SAND

OFFSHORE CLAY

by U. Roeper 1985

4.6 GROUNDWATER CONTAMINATION

A continuous contaminant distribution throughout the area would mean that the plume could only be imaged with respect to the other soil units. However, Figure 26 shows how conductivities of the groundwater vary with location. In general conductivities increase at and beneath the landfill and decrease as the distance from the landfill increases.

When examining the conductivities, the reader should be aware that the values by UMA and GLA are laboratory measurements of water samples, while the other values are field results. A YSI model 33 was used for the field results. It was noted that fouling on the conductivity probe produced consistently low readings for higher conductivities. This does not invalidate their qualitative meaning.

Contaminants leached from the buried waste are assumed to enter the groundwater unit via two separate flow passages. The direct flow passage is through permeable sandbars into the flow field in the sands beneath the floodplain silts. The less direct source is by slow seepage of leachates through the clayey silt channel fill.

While the silt seepage is a continuous process, the sandbar passage may conduct increased amounts of leachate during times of high infiltration (eg. snowmelt). The primary passages in the sandbars are believed to lead south along the west side of George Lake. The channel bed is actually the least active conductor since it features the thickest silt layer.

Contamination of the silt around the landfill is also likely, if only to a lesser extent. Lateral seepage in the silt is slow. However, clay particles in the soil attenuate the contaminants with time by adsorption. Soil and silt contamination was not assessed for this study.

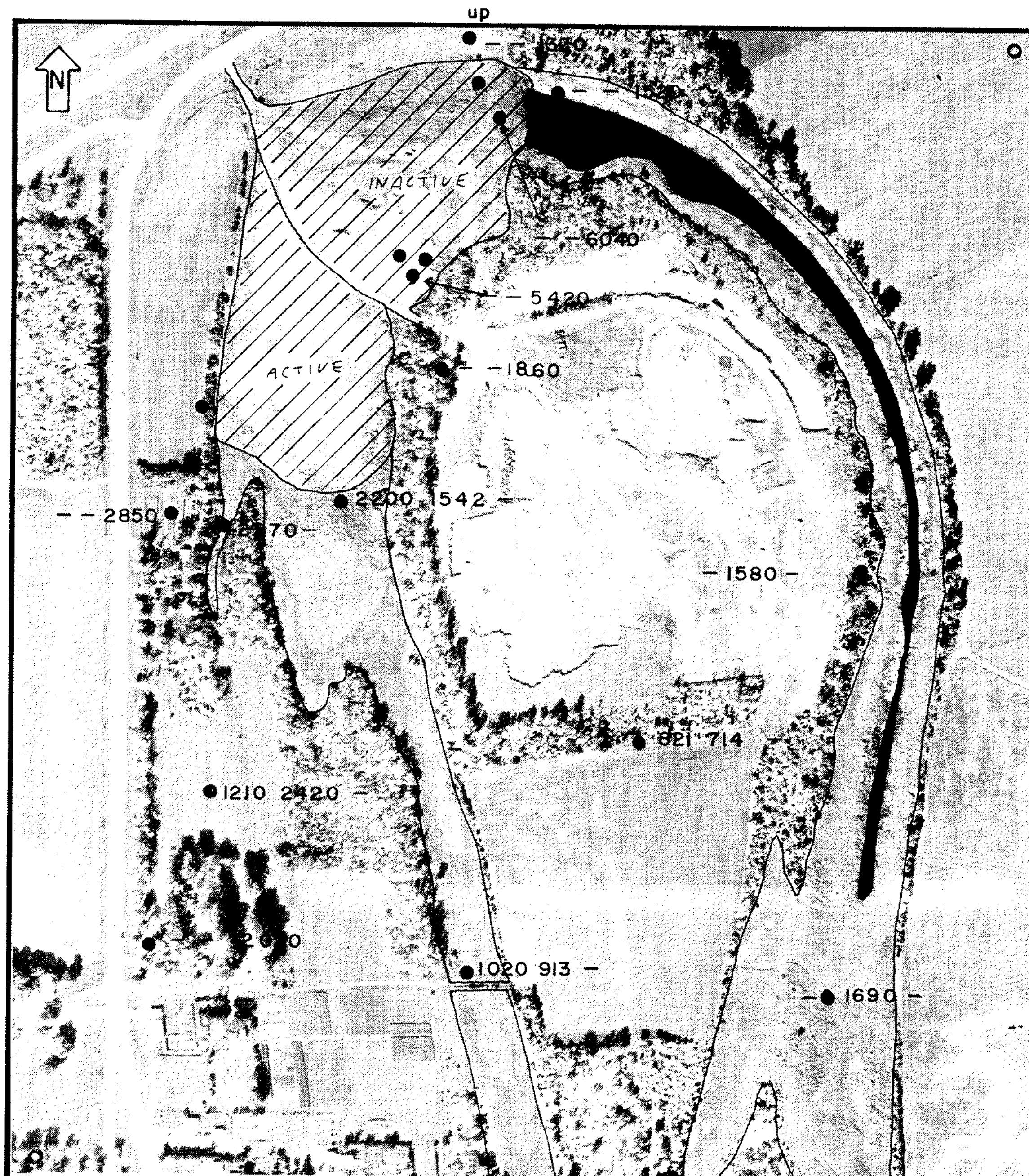

LEGEND

DUMP

OXBOW

OXBOW LAKE

2200 – – MAY 1985

– 2270 – OCT. 1984 (G.L.A.)

– – 1320 OCT. 1983 (UMA)

scale 1:3937

FIGURE 26.

CONDUCTIVITY OF GROUND WATER

by U. Roeper 1985

4.7 SUMMARY OF CHAPTER IV

A thorough understanding of the site geology was gained during this study. The area consists of basin clay overlain by sand and covered by floodplain silts. Groundwater flows south towards the Assiniboine River in the sand unit.

Site history shows that waste was historically deposited in the oxbow lake. To date, the landfill covers five hectares and is up to 15 m high. Wells in the area have been contaminated by leachate from the landfill.

Contaminants are believed to enter the groundwater via two passages -- sandbars and seepage through silt.

Chapter V

PORTAGE FIELD WORK

5.1 INTRODUCTION

To locate a suitable site for the Electroscan application, a reconnaissance geophysical survey was carried out. To avoid property conflicts, a site on the dry bed of George Lake was sought.

After a site with acceptable impedance responses was located, two grids of 64 electrodes each were set up; one large, one small. The method of data collection of previous studies was followed to minimize complication and to ensure compatibility with the Electroscan computer program.

After the data collection on the grids was completed and the set-up could be removed, sample holes were dug on both grids, soil logs taken, and groundwater conductivity measured. Finally, a magnetometer survey was carried out to ensure no large ferromagnetic objects (such as car bodies) were buried beneath the grids which might have interfered with the data collected.

5.2 GEOPHYSICAL EQUIPMENT

For the reconnaissance and the grid data collection, an extended sensitivity BISON 2350 resistivity meter was used. The unit combines a constant current generator with a manually balanced potential measurement circuitry. The current used consists of a low frequency 20.5 milliamperes source driven to a maximum 270 volts to overcome contact resistance in dry soils.

The potential measurement circuitry features an increased precision measurement switch to ameliorate contact resistance at the potential electrodes. Since all measurements for this study were conducted in moist, conductive soils, this feature gave no noticeable measurement improvement and thus was not further utilized.

For potential measurements taken at the most sensitive scale (.001 multiplier) provisions for balancing the contact resistance of both potential electrodes were utilized. However, operation of the equipment at this scale proved difficult. In most instances when working with this sensitivity, which occurred frequently, after balancing the instrument, considerable drift and noise would cause uncontrollable fluctuations in the readings. Often it was impossible to adjust the instrument at all. In addition, poor correlations existed between values read at this scale and upper scales. To achieve consistency in the results, all readings taken on the 64 electrode grids were collected using the .01 scale. At this scale the instrument was usually well behaved and repeated measurements would yield consistent results.

It was believed, although it could not be confirmed, that contact resistance and natural earth-currents were responsible for the erratic instrument behaviour at the .001 scale. It is proposed that a self-potential exists in the subsurface at the site between the contaminated water, the silt, and less contaminated water which affects potential measurements. This conclusion is based on the analogous existence of measurable self-potentials between drilling muds and groundwater in geophysical bore hole logging.

Finally, the readings obtained on the BISON 2350 are expressed in current normalized potentials, ie (2π V/I). This feature is significant when the current electrodes are placed on highly resistive ground and the nominal current of 20.5 milliamperes cannot be achieved with the maximum voltage available (270 volts). In this case, the normalized potential still produces an accurate result. In this study, this feature had no bearing; all readings were collected above 20 milliamperes.

To measure the groundwater conductivity in the sample holes, a YSI model 33 (also see Chapter IV) was used. This meter features a temperature/conductivity probe, submersible in water. At least three conductivity samples were collected and averaged for each reading. It was noted that this instrument was well behaved.

As mentioned earlier, slight fouling of the probe was experienced. All reported readings may be considered low, with higher readings being more affected. However, this does not affect the patterns generated by the readings and all comparative interpretations are valid. Little emphasis was placed on quantitative measurement since the Electroscan computer program used produces unscaled conductivities only.

The instrument used in the ferromagnetic survey was a SINTREX MF-2 flux-gate magnetometer. This unit features a readable sensitivity of $\pm$ 10 gammas at a full-scale deflection of 500 gammas. This unit is vertically polarized and should be capable of locating survey stakes, steel drums (near the surface) and larger ferromagnesian objects. The instrument was base-stationed before and after the survey to correct for magnetic drift.

5.3 RECONNAISSANCE GEOPHYSICS

A shown Figure 27, two resistivity soundings and two profiles were carried out in the east limb of George Lake on August 30 and September 9, 1984. Plots 1 and 2 * are the response curves for soundings S1 and S2 respectively.** The soundings were used to determine a suitable electrode spacing for profiling the desired target layer. It was decided that an electrode separation (A-spacing) of about 18.3 m would best represent the sounding responses for the target layer. A need to invert the results did not exist since sufficient subsurface data were available.

By inspection, sounding S2 showed conductivities for the silt layer (below full saturation) were around 600 micromhos/cm near the base of the landfill. Also, the maximum response of 850 micromhos/cm on the sounding curve indicates that the target layer had a "minimal" conductivity of 850 micromhos/cm. The nearby monitoring well sampled in October, 1984 (Figure 26) showed the groundwater to conduct 2200 micromhos/cm (target layer). It is apparent that the response curve would require inversion if the target layer conductivity was unknown.

A 600 m long profile (P1, shown on Plot 3) was run using 33 stations from the edge of the dump,south,in George Lake oxbow. The selected electrode separation of 18.3 m was used.

* All plots appended after text.

** For compatibility with the YSI conductivity meter and the Electroscan results, all responses are expressed in conductivities on all plots.

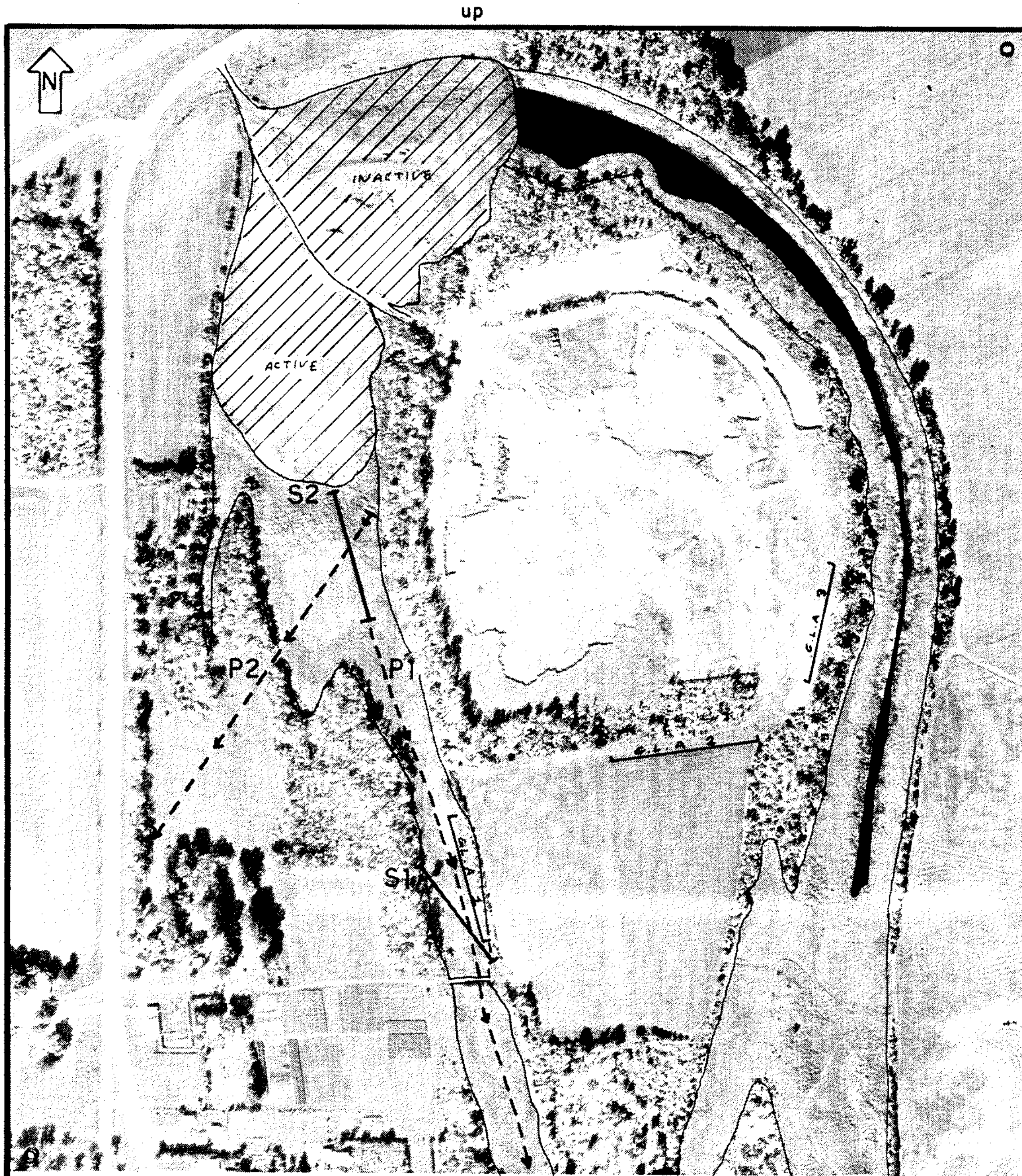

LEGEND

DUMP

OXBOW

OXBOW LAKE

S1 SOUNDING

SOUNDING BY G L A

P1 PROFILE

scale 1:3937

FIGURE 27.

RESISTIVITY PROFILES AND SOUNDINGS

by U. Roeper 1985

An inspection of the plot allows several interesting observations. The edge of the landfill introduces a topographic effect (due to current being drained into the waste mound), a culvert nearly the length of the electrode separation produces "bridging", and general noise of about 50 micromhos/cm is evident (likely due to lateral changes in soil resistance with saturation differences near the surface). However, between 90 m and 160 m south of the landfill (add 30 m to exact edge of fill), the bulk subsurface conductivity decreases from around 850 micromhos/cm to roughly 600 micromhos/cm. A look at Figure 26 shows that this corresponds to a drop of 1180 micromhos/cm in the target layer.

A second profile (P2, shown on Plot 4) was carried out on September 15, 1984. No changes of conductivity in the channel were observed, but significant decreases in conductivities occurred as the electrodes were moved onto the dry sandbars on the west river bank. The conductivity break located with the first profile was used as the impedance structure to be imaged by the Electroscan system.

Figure 28 shows how the two electrode grids were located in the channel. For the large grid, several lines were cut through the brush on a sandbar which occupies the southwest part of the grid. The small grid was simply located in the open marsh.

The large grid was given an electrode spacing of 12 m. This made the grid 84 m x 84 m with each subsurface block layer representing a 12 m theoretical depth unit. The small grid was chosen at a 3 m electrode spacing and 21 m x 21 m in size with each block layer a theoretical 3 m thick. Both grids were surveyed into place.

up

LEGEND

DUMP

OXBOW MARSH

OXBOW LAKE

scale 1:3937

FIGURE 28.

ELECTRODE GRID LOCATIONS

by U. Roeper 1985

5.4 DATA COLLECTION

For each grid, 64, 90 cm long, one-half inch round aluminum electrodes were used. The electrodes were pushed or hammered into the ground with 10 cm exposed. A central control box was constructed and TEW 16 gauge multistrand (PVC insulated) wire connected from it to all electrodes. To ensure good electrode contact, the wires were fastened to the electrodes with hose clamps and small screws.

Before and after the collection of a data set, all electrodes were checked for continuity from the control box (ie. electrical test for damaged wires). All grid measurements were also collected from the box.

Conventional Wenner arrays and Electroscan type data were collected on each grid. For the Wenner arrays, only two A-Spacings could be collected due to the dimensions of the grids. For the large grid, spacings of 12 m and 24 m were used; on the small grid, 3 m and 6 m spacings were collected. Since the amount of arrays possible on the grid were limited, a complete set of Wenner data could be measured in under two hours.

For the Electroscan type data, the standard excitation pattern (Figure 13) with 14 current input pairs used in the earlier studies (11, 20) was employed here. However, a minor change in the method of potential measurement was necessary. The equipment used in the test-tank studies consisted of a custom built circuitry which collected (by digitized data acquisition) potential measurements at each electrode with respect to a reference zero potential on the switchboard. The BISON 2350 measures potential drops between two points only and not with respect to an internal zero. After oral consultation with Wexler

(20) it was decided that all measurements could be made by using one electrode as arbitrary zero and measuring all potential drops with respect to it. Electrode number 36 was chosen on both grids as reference zero. Wexler (20) assured that this procedure would be fully compatible with the Electroscan algorithm; later experiments by Allard (2) confirmed this.

A complete set of potential measurements for one grid took approximately five hours to collect. All grid data was collected between October 12 and 15, 1984. As discussed in Section 5.2, poor instrument behaviour did not allow the most sensitive scale (.001) on the Bison equipment to be used. This made approximations of very small potentials difficult. For potentials around zero, the electrode polarity was always reversed to double check for positive or negative current flow direction.

For discussion of the Wenner and Electroscan results (Plots 5 to 47), refer to Chapter VI.

5.5 SUBSURFACE SAMPLING

A subsurface sampling program was undertaken on May 9, 1985 to confirm the existence of the imaged impedance structures. The program consisted of a hired backhoe used to dig sampling holes through the channel fill to the saturated bedload sand below. A stainless steel well point was then pushed into the sand layer and conductivity samples were extracted at depth. As shown in Figure 29, eight sample holes were completed. Detailed soil logs were kept (Appendix A) and cross-sections were constructed as shown. Sample holes 1 to 7 were all dug in the channel while hole eight was located on the sandbar deposit (treed area).

It was noted that a thinly bedded firm clay separates the silt from the underlying sand (see Figure 30, 31). The presence of this clay layer

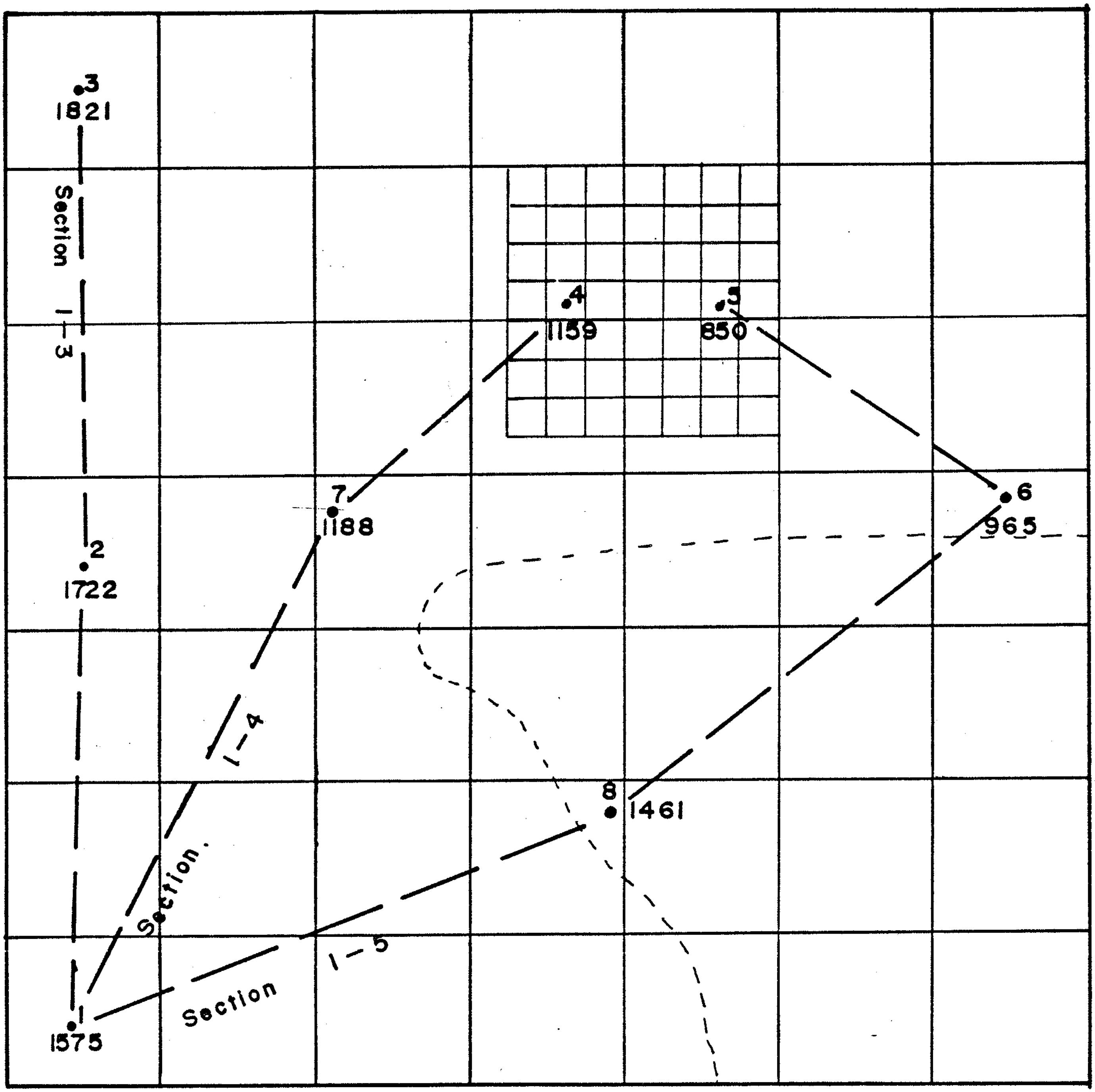

CONDUCTIVITY SAMPLES OF GROUND WATER

•1 = SAMPLING HOLES

1575 = WATER SAMPLE CONDUCTIVITY IN MICROMHOS / CENTIMETER

= EXTENT OF BUSH AND TREES (SANDBAR)

TOP OF PAGE IS EAST

FIGURE 29.

by U. Roeper 1985

is assumed to be related to sedimentation of fine suspended particles immediately after the cut-off occurred. Except in the sandbar (see Figure 32), the clay forms a continuous low permeability blanket overlying the bedload sands. It was felt that this substantiated the theory of groundwater contaminant passages through sandbars proposed in Chapter IV.

The coarse bedload sands at depth were clearly differentiated into light yellow brown sand and dark grey sand. Since no apparent difference in composition or grain size was noted, two possibilities were considered:

a) The difference in colour indicates separate river phases.

b) The grey sand represents the reducing environment of prolonged submersion below the water table.

The latter possibility was deemed more likely. Sampling the conductivity above and below the grey sand showed no notable difference; it was concluded that the coarse sand (if saturated) could be treated as one impedance structure.

Although most of the silty channel fill was located above the groundwater table, and a continuous upward decrease in conductivity and saturation exists, the unit was considered as one impedance structure vertically. This assumption seems justified since the 90 cm electrodes penetrated most of this unit to achieve an average contact resistance. Lateral changes in conductivity will, of course, affect measured conductivity. These may be due to saturation changes away from the centre of the channel, as well as, local soil contamination discussed in Chapter IV.

The cross-section in Figure 32 clearly shows how the sandbar protrudes upward to the surface without the presence of a clay layer or a silt channel fill cover. The sand does however show characteristic

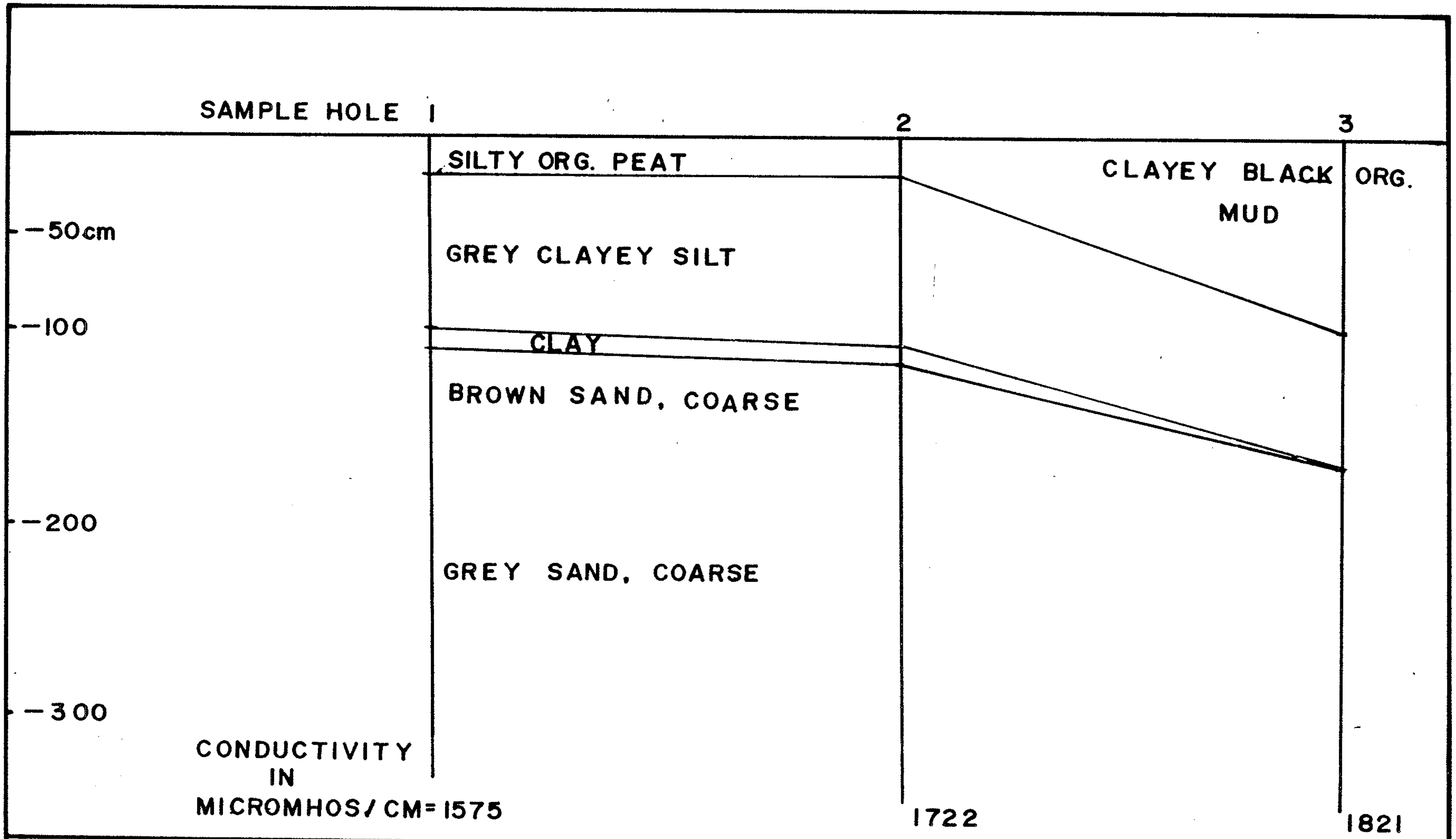

FIGURE 30. GRID CROSS-SECTION 1-3

HORIZ. SCALE 1:480

——— CONTACT (Interpolation)

– – – CONTACT (Infered)

by U. Roeper 1985

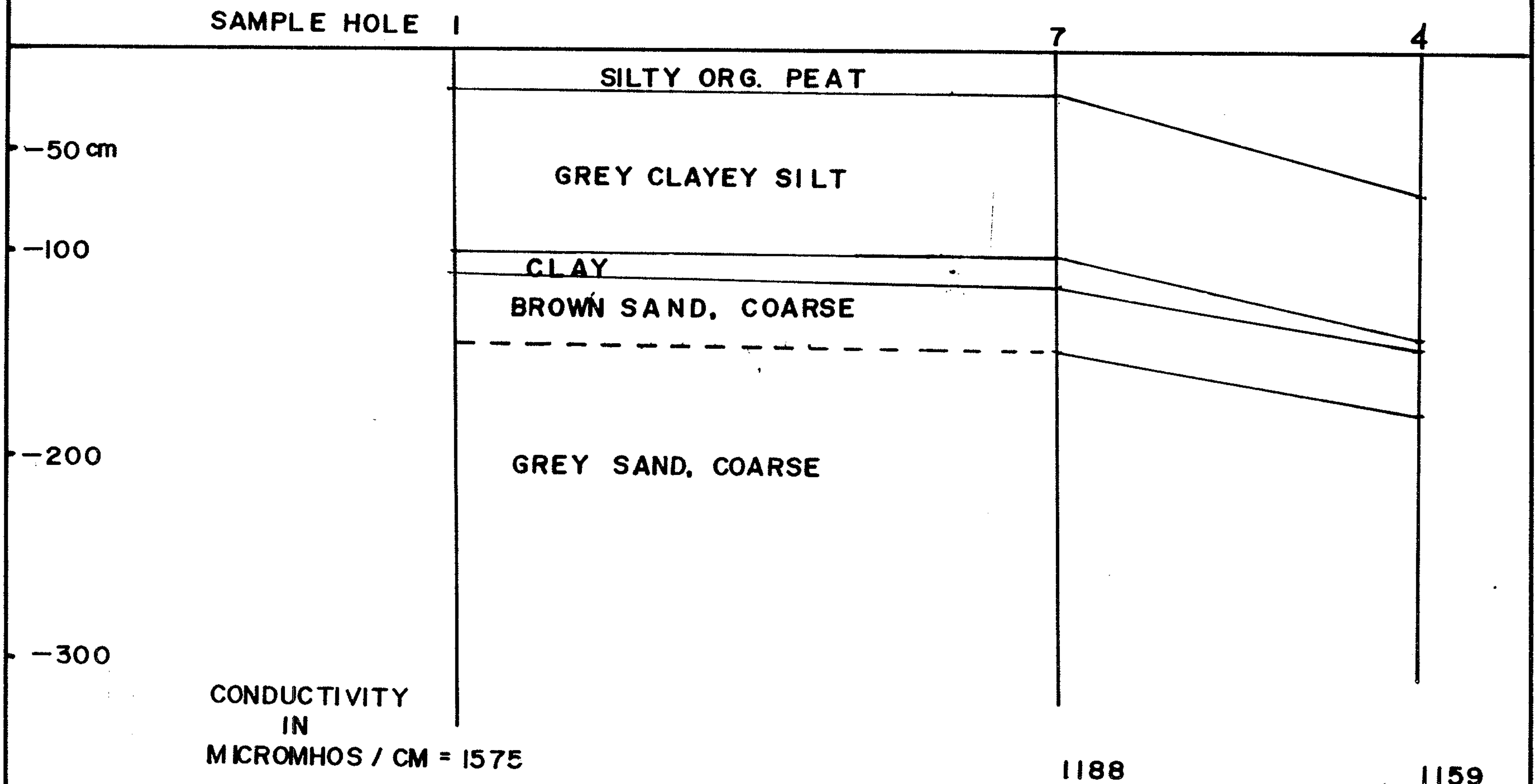

FIGURE 31. GRID CROSS—SECTION 1—4

Horiz. Scale 1:480

——— CONTACT (Interpolation)

– – – CONTACT (Infered)

by U. Roeper 1985

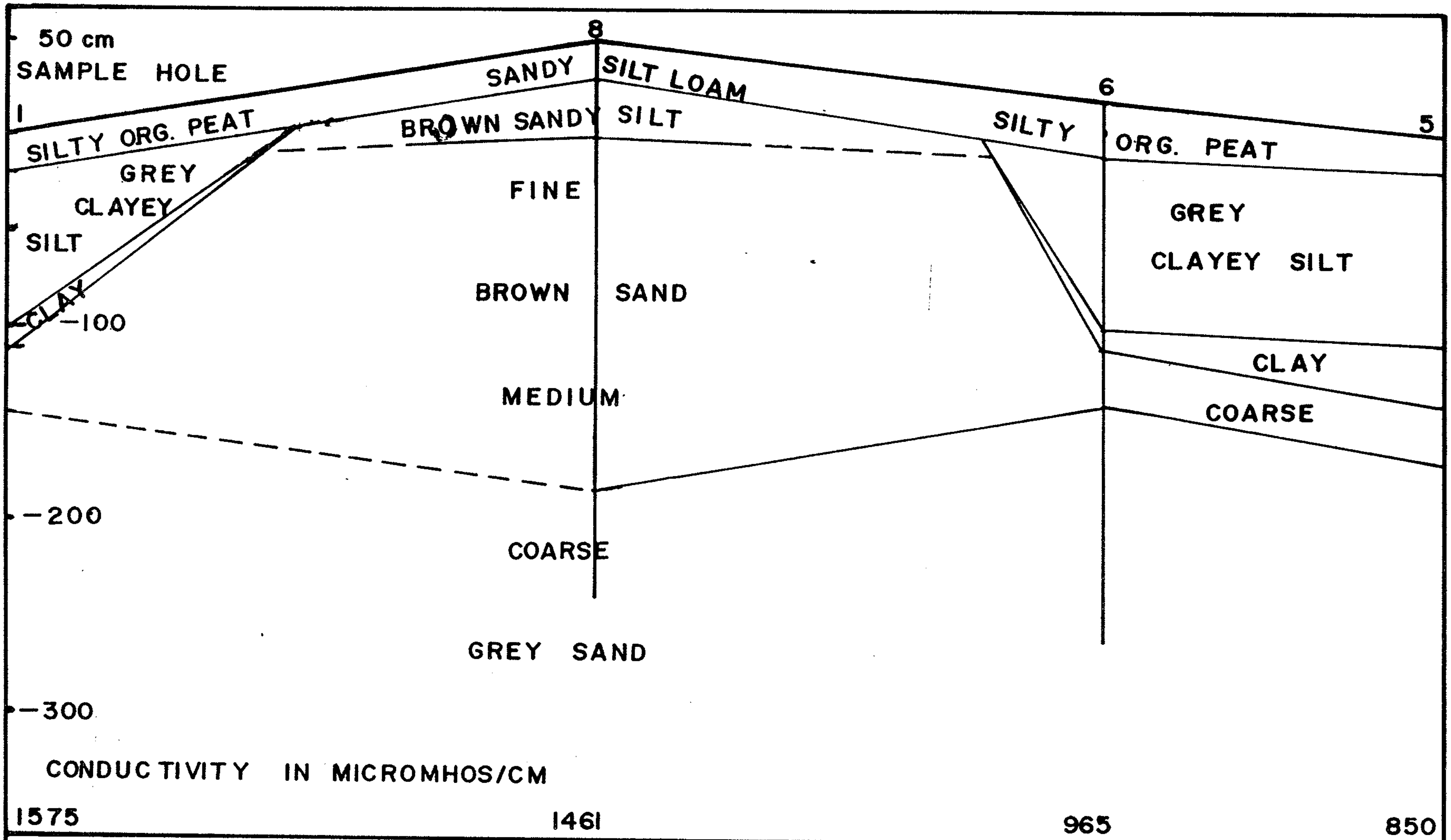

FIGURE 32. GRID CROSS—SECTION 1 — 5 Horiz. Scale 1:480

——— CONTACT (Interpolation)

– – – CONTACT (Infered)

by U. Roeper 1985

fining upwards, medium to fine further up and fine to very fine near the surface.

As an impedance structure, the sandbar is a significant feature for three reasons:

a) The saturation level decreases continuously from the water table to the surface, causing a continuous decrease in conductivity upwards.

b) Near the surface, the sands are drier and of relatively high resistance. Consequently,the electrode contact resistance is higher in this part of the grid than elsewhere. The electrodes are no longer situated in a homogeneous host.

c) Infiltration of precipitation through the sand causes flushing of contaminants downward. This may cause conductivities of the groundwater to be greater at depth.

The groundwater conductivities for each hole may be read from Figure 29 and the respective cross-sections (Figure 30, 31, 32). By inspection, it is apparent that conductivities in the target layer are highest to the north (close to landfill) and lowest to the south (in general). Conductivities are also higher beneath the sandbar (hole eight) than in the south part of the channel. For the small grid located in the channel, conductivities again are less to the south. A total conductivity contrast in the area sampled is greater than 2:1. By inspection of the measured conductivities in the monitoring wells (Figure 26), and the results of reconnaissance profile P1 (Section 5.3), the sampled conductivities prove to stand in good agreement. It is evident that real impedance structures exist beneath the study site.

5.6 Magnetometer Survey

On May 23, 1984 a magnetometer survey was conducted. It was thought possible that large metal objects such as culverts or car bodies might be buried in the channel fill. From the data obtained (Figure 33), presence of large ferromagnetic objects is not evident.

5.7 SUMMARY OF CHAPTER V

Two electrode grids were set up in the location suggested by a reconnaissance geophysical survey. Conventional Wenner and Electroscan type data were collected. Subsequently, a detailed subsurface investigation was carried out beneath the site. It was confirmed that significant impedance structures are present in the subsurface. While groundwater conductivity varies by more than 2:1, significant impedance structures exist in the form of sandbars and channel fill. In general, the contaminated groundwater forms the most conductive impedence structure; unsaturated sandbars form the least conductive impedance structure.

57	500	500	500	500	500	500	500	500	500	500	500	500	500	500	64
	500	500	500	500	500	500	450	500	550	500	450	550	500	500	
	500	450	450	500	500	500	500	500	500	500	500	500	500	450	
	500	500	500	500	500	500	500	500	500	450	500	500	500	500	
	500	500	500	500	500	500	500	500	500	500	500	500	500	500	
	500	500	500	500	500	500	500	500	tin cans	500	500	550	500	500	
	500	500	500	500	500	500	500	500	500	500	500	500	500	500	
1	500	500	500	500	500	500	500	500	500	500	500	500	500	500	8

MAGNETOMETER SURVEY

VALUES IN GAMMAS (DRIFT CORR.)

TOP OF PAGE IS EAST

FIGURE 33.

by U. Roeper 1985

Chapter VI

ELECTROSCAN RESULTS

6.1 INTRODUCTION

This chapter presents the results of the Wenner and Electroscan type data collected on the large and small grid. The existing impedance structures described in Chapter V, and the previously observed characteristic of the algorithm in Chapter III were used to assist in the interpretation and evaluation of the obtained results.

6.2 DATA PRESENTATION

The conventional Wenner data collected was hand contoured over the grid areas. Separate plots were made for each A-spacing on each grid. Some extrapolation was required for the larger A-spacing since only a limited number of points could be collected on each grid. The reader is reminded that all conventional data is representative of "bulk" conductivities only (see Section 2.1 for discussion).

Electroscan type data was processed on the computer facilities of the Electrical Engineering Department where previously all test-tank data had been run. Direct access to the computer program and the algorithm was not possible.

It should be noted that the Electroscan type data was first put into an 8 x 8 matrix format with the top left hand being the potential at electrode one and the bottom right being the potential electrode 64. Although the reverse of the grid notation, this was the requested input format. The output, as displayed on the contour plots is identical to the block positions on the field grids.

Since the 64 electrodes used circumscribe only 49 blocks for each layer, only that many blocks appear on each output. Each number represents the calculated conductivity of a block, not an electrode.

The Electroscan computer program, although a working algorithm, is still in the experimental stage. For this reason, some arbitrary scaling factors were used to fit the input data into a suitable magnitude for the program. Accordingly, the obtained output is in <u>unscaled conductivity values</u>.

Since the block size, or electrode separation, must be considered when calculating unit conductivities (not considered in the Electroscan program), the results on the contour plot for the larger and the small grid were normalized. The normalizing factor used was 12/3, based on the difference in electrode separations.

Consequently, all conductivities calculated by the Electroscan program for the small grid were multiplied by 4. This should allow for a direct comparison of conductivities on the two grids.

All contours of the Electroscan™ results were produced by an SAS (statistical analysis system) plotting program on a Xerox laser printer at the University of Manitoba computing facilities. Although output data from each iteration was available, only selected iteration results were plotted. The presentation of all data would have been vastly excessive and of little interpretational value. For all iteration results used (20, 100, 200 iterations), one plot is included per block level (computations to a depth of 4 and 5 levels were used).

6.3 WENNER CONTOURS OF SMALL GRID

The Wenner contours may be found on Plot 5 and Plot 6. Plot 5 shows the contouring results for the 3 m electrode separation on the Wenner array. Conductivities evenly increase east (top of page) to the center of the channel.

Given the small electrode spacing, this plot is a good indicator of the bulk conductivities in the upper, say 120 cm, of the silt zone (electrodes are 90 cm). Soil moisture is assumed to be the controlling factor of increased conductivity near the channel centre but soil contamination is equally plausible.

In general, the conductivities (565 micromhos) compare well to the sounding S2 at that electrode spacing (580 micromhos) (see Plot 2), conducted in the channel center, just north of the grids.

Plot 6, the 6 m electrode spacing, shows nearly identical results. The wider spacing with identical results is a good indicator that the bulk conductivity in the silt layer is changed only slightly with depth but more laterally. The expected penetration depth for this spacing should represent roughly the upper 2 m in the silt layer.

6.4 ELECTROSCAN CONTOURS OF SMALL GRID

The data collected on the small grid was run on the algorithm for 200 iterations. The depth was computed to 4 block layers. Since the block size is 3 m, the depth units should correspond to 0-3, 3-6, 6-9, and 9-12 m. Presented in Plots 7 to 18, are the 20th, 100th and 200th recursion results.

The first layer in each iteration (Plots 7, 11, 15) shows large changes in conductivity within the grid area. From the Wenner results above, and the knowledge of the silt layer, only small changes in conductivities should exist. Therefore, the top layer appears erroneous.

The second layer (Plot 8, 20 iterations) shows a ridge of higher conductivity towards the centre of the channel. This, to some degree corresponds to the Wenner results obtained for the silt layer; conductivities are generally lower to the west and higher towards the east.

The reconnaissance geophysical profile (Plot 3), and the groundwater conductivities sampled,indicate a conductivity decrease to the south of this grid. Since this layer represents a depth of 3 - 6 meters, the observed groundwater differences should appear; they do not.

Depth layer 3 and 4 (Plot 9, 10) show a continuation of the pattern observed in layer 2. Since the alluvial sands are underlain by basin clay, a more uniform conductivity distribution was expected. A shadow effect (discussed in Chapter III) appears to exist for these deeper layers.

Judging from the high conductivity values observed after 100 and 200 iterations, and the lack of recognizeable conductivity patterns, the recursion appears to show deterioration. Interpretation of Plots 11 to 18 is not useful. It appears that excessively high values for individual blocks were computed after 200 iterations.

6.5 WENNER CONTOURS OF LARGE GRID

The Wenner contours may be found on Plot 19 and 20. Plot 19 shows the contouring results for 12 m spacing; Plot 20 for 24 m spacing.

Several important conductivity features may be observed on both plots. For the 12 m spacing, a clear outline of the low conductivity sandbar is shown on the southwest part of the grid (top of page is east). When compared to the grid location map, Figure 28, it also becomes evident how the narrowing channel (narrowing to the south) is reflected in the east part of the plot.

A comparison with the subsurface conductivities sampled shows good correlation with the bulk conductivities of the Wenner data. The high conductivity observed beneath the sandbar is not reflected on this plot. This is easily attributable to the low surface conductivity of the sand overlying it. A masking of the conductivity in the groundwater is observed by collecting the bulk conductivities; this results in a strong reflection in soil moisture variations and less reflection of deeper features.

The 24 m spacing Wenner shows a similar contour pattern. Again, the sandbar is clearly evident. Also, the groundwater conductivities sampled are even more strongly reflected in this plot.

6.6 ELECTROSCAN CONTOURS OF LARGE GRID

The large grid was imaged using a computational depth of 4 (Plots 21 to 32) and 5 (Plots 33 to 47) layers. Since the block size is 12 m, the depth units should correspond to 0-12, 12-24, 24-36 and 36-48 m (also 48-60 for 5 layers). It can therefore be expected that layers 3, 4 and 5 would image the basin clays. Conductivities should be quite homogeneous for this underlying sediment.

By inspection of Plots 21, 22, 23, 24 (image after 20 iterations), a low conductivity area is clearly developed in the southwest (top of plots is east) corner of the grid. On the first and second layer, this clearly corresponds to the sandbar located in that part of the grid. However, this feature carries into all lower layers although at a smaller amplitude. It appears that this is the same "shadow" effect noted by Wexler (20) in earlier studies.

The main feature on these plots is a high conductivity structure in the centre of the grid. This feature is not explained by knowledge of the subsurface. The greatest conductivity peak is located in the center of layer 2 (Plot 22). With over 35000 conductivity units, this block should be 11 times more conductive than background; this is not deemed likely.

Plots 25 to 32 show how the images deteriorate with higher iterations. Conductivity contrasts of 20:1 are generated (Plot 30) in layer 2 with a low conductivity for layer 1 and shadow conductivities at depth.

For those results imaged to a depth of 5 layers (Plots 33 to 47) several observations were made. For 20 iterations, the results are nearly identical to the 4 layer computations; after 100 recursions, however, the results have more strongly deteriorated. Starting from layer 2 downward, increasingly large and fictitious conductivity peaks are created. In subsequent iterations, the increased conductivity appears to "carry" into the next lower layer.

6.7 DISCUSSION OF RESULTS

6.7.1 OBSERVATIONS

The geophysical results obtained with the Electroscan system are quite different from the results of earlier experimental work. Comparison and inspection of these results allows a number of valuable observations to be made on the behaviour and characteristics of this imaging system.

1) Images are constructed from the top down, layer by layer, with successive iterations.

2) Image errors introduced in an upper layer are carried into lower layers during subsequent iterations.

3) The first layer is consistently of poor quality in all images using physical measurement data, but not when using computer simulated data.

4) Shadows of conductivity features in the upper layers of an image appear in all subsequent levels even if the subsequent levels are of constant conductivity.

5) Horizontal shadows parallel to highly conductive objects can occur on some images.

6) Symmetric shadows occur in the corners of some images using aquifer test bed data.

7) When using physical measurement data, the imaging process diverges before a sufficient number of iterations have been completed to fully reconstruct the image.

In an attempt to identify the origin of these observations, it becomes apparent that the overall image quality using simulated data is excellent, using test tank data it is good, using aquifer test bed data it is fair, and using field data it is poor. This decrease in image quality is associated with an increase in shadows, a deterioration of the first layer and a considerable decrease in the amount of successful iterations before divergence. The nature of this decrease in image quality appears to be related to decreasing measurement data quality.

6.7.2 DATA QUALITY

The observations of this study appear to show that data quality is the primary factor controlling image quality. Before real improvements in the image quality can be made, it is essential to identify the causes of poor data quality. In this study, the main causes were equipment limitations, and geophysical factors which affect the potential measurements in the field.

The limitations of the earth-resistivity equipment are related to the grid geometry. Contrary to conventional earth-resistivity measurements, the majority of measurements on the Electroscan grid are carried out away from the major current path. The potential drops which need to be measured accurately become exceedingly small for the instrument precision available and force most of the measurements below 10 per cent, and many below one per cent of full scale. Somewhat greater precision could be obtained at the most sensitive scale, but as pointed out in Section 5.2 above, erratic meter fluctuations made reading this scale impossible, and even with its use, the precision of the equipment is still inadequate.

In addition to the equipment limitations, changes in the mathematical boundary conditions, complex impedance structure and geoelectric phenomenon distinguish the field study from the laboratory tests. These factors which are characteristic of the geophysical testing environment are suspected to be a major cause for the low data and image quality.

The change in the boundary condition results from the absence of the infinitely resistive cube boundaries of the acrylic test tank. The mathematical boundary condition of the Electroscan algorithms, the Neuman Boundary Condition, assumes no current flow across the cube boundaries to occur, but in the field, small amounts of current do cross the imaginary cube boundaries. Even if the net current inflow and outflow are balanced, some edge distortion is likely to occur. The symmetric shadows observed in the test tank images and the concentric nature of the field images may be evidence for this condition.

The complex impedance structures do not affect the measurement accuracy, but they do place an increased demand on measurement precision. The impedance contrast of these structures is less than 3:1 at the Portage site with several smaller contrasts to be detected. Since the Portage site is not untypical of other disposal sites, increased measurement precision may be essential to delineate the complex structures at such sites.

Lastly, geoelectric phenomenon may have a significant effect on measurement accuracy and data quality. Equipment manufacturers and researchers (10) (12) have reported on the effect of imbalanced electrodes, contact resistance and natural earth currents on earth-resistivity measurements. Natural earth currents are the likely cause for the meter fluctuations at the most sensitive scale as mentioned above. The currents may be present wherever natural potential differences exist; for example between the contaminant plume and clean groundwater, or between differentially saturated soil horizons. In the field of electric bore hole logging, natural earth currents between the drilling muds and some formations are in the tens of millivolts. Poor contact between the soil and the electrodes or an imbalance in the electrode contact due to lateral variations in soil conductivity and saturation further contribute to innacuracy in the measurements.

It is apparent that the factors influencing data quality are numerous and their effect on image quality is substantial. Although little can be done about the complexity of geophysical impedance structures, equipment capabilities may be improved and geoelectric phenomenon reduced. The influence of missing boundary conditions is something which may require consideration in the Electroscan system. It is, nevertheless, clear that an improved image quality will only result from improved data quality.

6.7.3 IMPROVING DATA QUALITY

Data quality may be improved by either compensating for geophysical influences or extending equipment capabilities. Compensating for geophysical influences is difficult since this implies quantifying geoelectric phenomenon and measuring such factors as natural earth currents. The greater potential for data quality lies in technical advances of equipment capabilities.

The earth-resistivity equipment used in this study has been on the market for over 25 years and does not represent state of the art technology. Present equipment is capable of much extended precision and accuracy by multiple digital data collection, and improved electronic compensation for imbalanced electrode contact. Implementing such equipment may already produce much improved image quality.

Further improvement may be possible by implementing such experimental techniques as phase locked frequency multiplexing. This would allow complete filtering out of natural earth currents and substantially increasing the speed of data collection by collecting simultaneous measurements.

Clearly, the major advances will come from the application of more sophisticated data collection methods which will provide the necessary baseline data for resolving the complex geophysical impedance structures. Such technologically advanced methods are essential if the Electroscan system is to be used for geophysical imaging.

6.8 CONCLUSION

The Portage la Prairie field study was the first application of the Electroscan imaging system in a geophysical testing environment. This testing environment was substantially more complex, and accordingly produced much lower quality images than previous laboratory experiments. However, valuable observations made on the nature of the testing environment and the results obtained indicate that considerably improved results are attainable.

The intention of the study was to image the impedance structure of an existing pollution plume from the adjacent Portage landfill site. The two electrode grids used to collect the potential measurements were therefore set up above the plume front which was located with conventional geophysical techniques. After the Electroscan data was collected, a detailed subsurface investigation was carried out. This investigation, which consisted of earth-resistivity measurements, sample holes, water conductivity measurements, and a magnetometer survey, confirmed the existence and location of the plume front and revealed a site geology much more complex than anticipated.

The Electroscan images derived from the two electrode grids are of poor quality. Although the images show distinct zones of elevated conductivities, the delineation of the pollution plume or the identification of the complex site geology is not readily possible. Five major discrepancies obscure and characterize the image quality.

1) The imaging process diverged before 100 iterations were reached. Earlier studies using simulated measurement data have shown that over 1000 iterations are required before even simple objects are fully reconstructed. This suggests that the complex images obtained from the field data were not developed before divergence occurred. Poor quality of the field data appears to be the cause of this divergence.

2) The top layer of the imaged cube appears distorted in all images and is generally not representative of existing impedance structures. This problem was also observed in earlier studies and was associated with measurement error. This study suggests that contact resistance at the electrodes and other geoelectric phenomenon may contribute to the distortion.

3) Shadows of highly conductive structures were often observed on images from earlier studies. The complexity of the source structure and the poor image quality do not allow these shadows to be identified in the field results. Shadows are likely to be hidden on the images; however, no explanation of their origin was found in this study.

4) All images obtained from this study are distinctly concentric in nature with a rise in conductivity towards the image center. The absence of a physical impedance boundary around the imaginary cube fails the Neuman boundary condition in the Electroscan algorithm and is held responsible for this image deficiency. A change in the boundary condition or a compensation for the current losses across the boundary may alleviate the problem.

5) Due to the experimental nature of the Electroscan algorithm, the conductivity values are in unscaled units. Although this has no direct impact on image quality it makes direct correlation of the images to water sample conductivities impossible. Scaled values should be available in the future.

The divergence of the imaging process, the distorted top layer and the conductivity shadows appear to be associated with poor data quality. The source of the poor data quality in this field study was caused by inadequate equipment capabilities for the size and geometry of the grid, and the presence of natural earth currents and other geoelectric phenomenon. These factors suggest that the field data is of considerably lower quality than previous laboratory data and responsible for the poor image quality.

While the boundary condition is a mathematical problem, the equipment limitations and geoelectric phenomenon are geophysical. Present state of the art technology and available equipment are capable of greatly reducing, if not eliminating, the geophysical problems encountered. Provided similar achievements are possible in handling the boundary condition, a considerable improvement in image quality is likely.

The Electroscan system is undoubtedly a powerful and unique approach to geophysical imaging. Its merit lies in the simplicity of obtaining a fully three-dimensional subsurface image using only surface potential data. Its deficiency lies in the demand placed on measurement precision and accuracy which is required to obtain a useful image. Clearly, if the latter can be overcome, the Electroscan system provides a major achievement in hydrogeologic subsurface investigations and contaminant studies.

GEOPHYSICAL PLOTS

SOUNDING ONE

CONVENTIONAL WENNER ARRAY

SOUTH IN GEORGE LAKE

CONVENTIONAL WENNER ARRAY

A-SPACING (meters)	BULK RESISTIVITY (ohm-meter)	MICROMHOS (umho/cm)
3.0	15.7	637
6.1	14.3	699
9.1	19.7	507
12.2	19.3	518
15.2	18.9	530
18.3	16.1	621
21.3	13.0	772
24.4	12.0	832

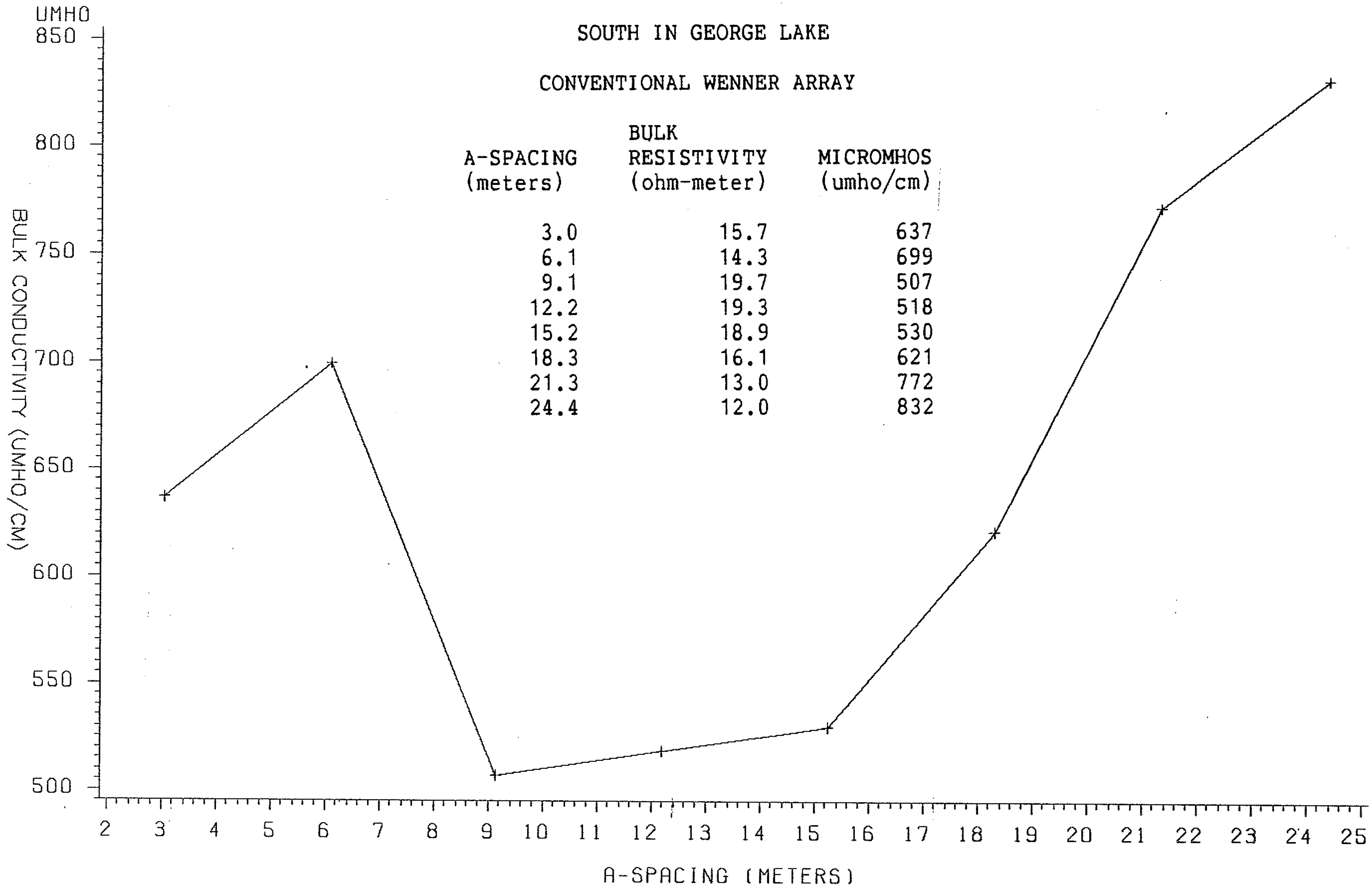

Plot 1

Plot 2

SOUNDING TWO

CONVENTIONAL WENNER ARRAY

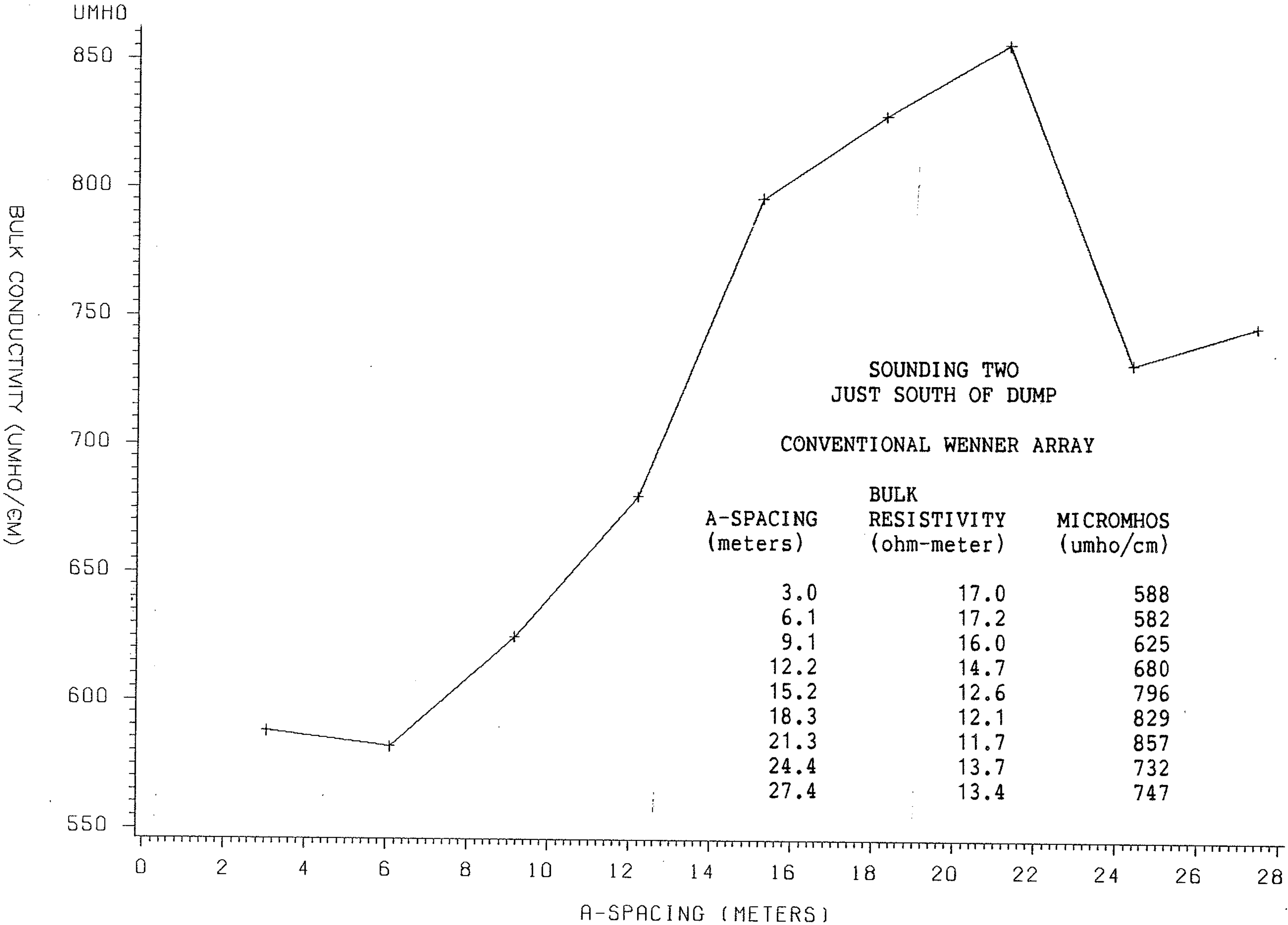

SOUNDING TWO
JUST SOUTH OF DUMP

CONVENTIONAL WENNER ARRAY

A-SPACING (meters)	BULK RESISTIVITY (ohm-meter)	MICROMHOS (umho/cm)
3.0	17.0	588
6.1	17.2	582
9.1	16.0	625
12.2	14.7	680
15.2	12.6	796
18.3	12.1	829
21.3	11.7	857
24.4	13.7	732
27.4	13.4	747

Plot 3

PROFILE ONE

A-SPACING OF 18.3 METERS

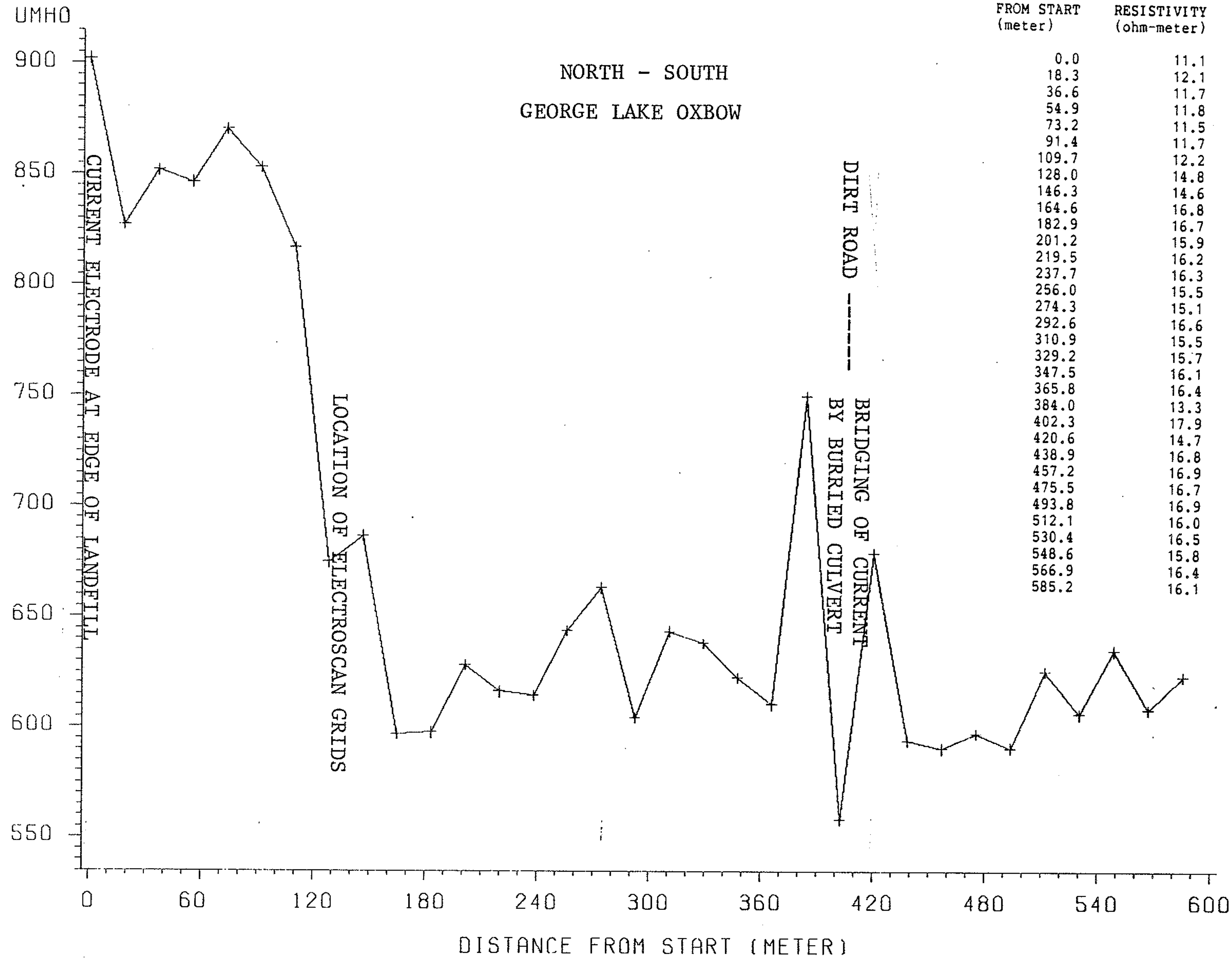

RESISTIVITY PROFILE ONE
MOVING SOUTH AWAY FROM THE DUMP

A-SPACING OF 18.3 METERS

DISTANCE FROM START (meter)	BULK RESISTIVITY (ohm-meter)	BULK MICROMHOS (umho/cm)
0.0	11.1	902
18.3	12.1	827
36.6	11.7	852
54.9	11.8	846
73.2	11.5	870
91.4	11.7	853
109.7	12.2	817
128.0	14.8	675
146.3	14.6	687
164.6	16.8	597
182.9	16.7	597
201.2	15.9	628
219.5	16.2	616
237.7	16.3	614
256.0	15.5	644
274.3	15.1	663
292.6	16.6	604
310.9	15.5	644
329.2	15.7	638
347.5	16.1	622
365.8	16.4	610
384.0	13.3	750
402.3	17.9	558
420.6	14.7	679
438.9	16.8	594
457.2	16.9	591
475.5	16.7	597
493.8	16.9	591
512.1	16.0	625
530.4	16.5	606
548.6	15.8	634
566.9	16.4	608
585.2	16.1	623

PROFILE TWO

A-SPACING OF 18.3 METERS

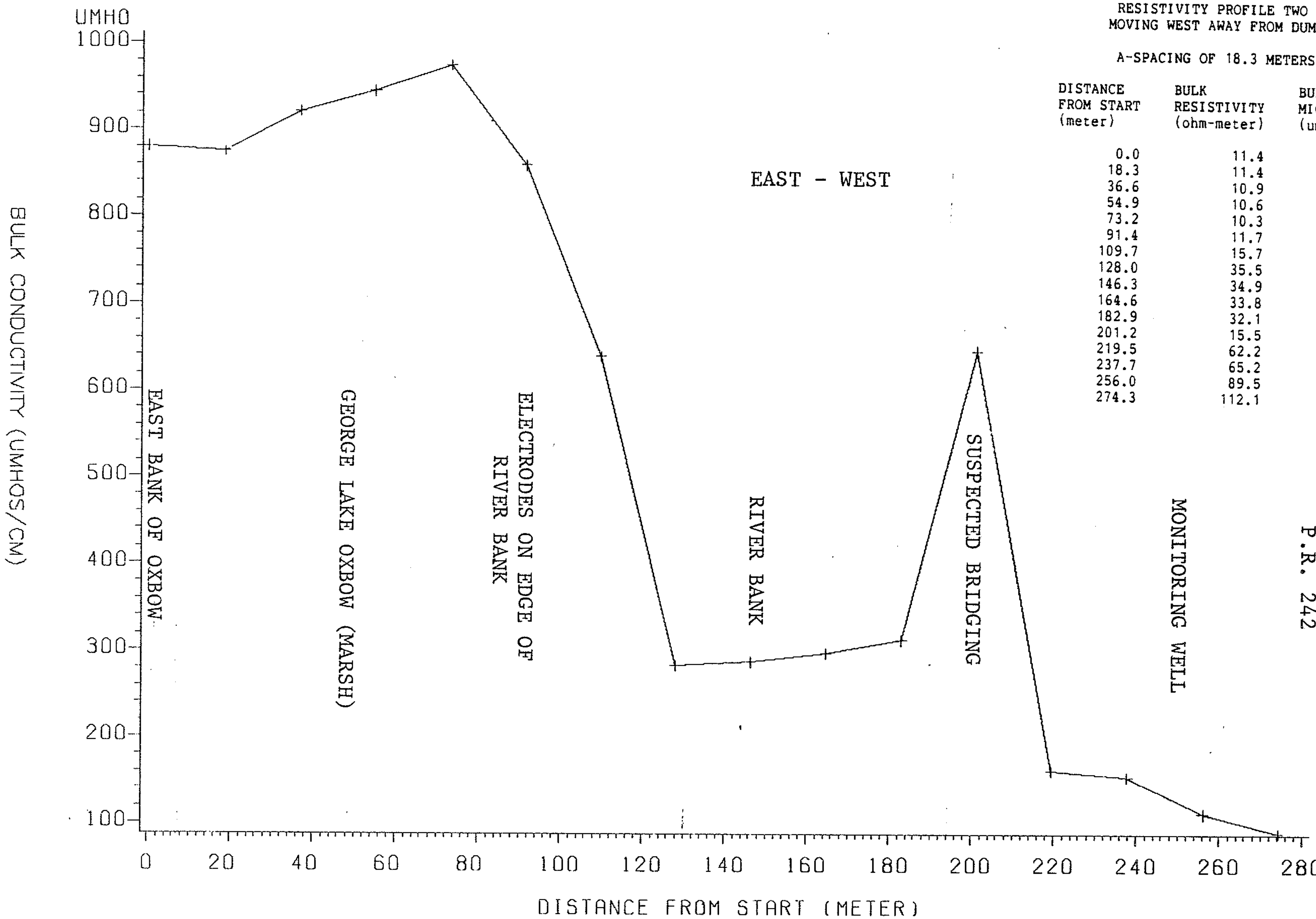

RESISTIVITY PROFILE TWO
MOVING WEST AWAY FROM DUMP

A-SPACING OF 18.3 METERS

DISTANCE FROM START (meter)	BULK RESISTIVITY (ohm-meter)	BULK MICROMHOS (umho/cm)
0.0	11.4	880
18.3	11.4	875
36.6	10.9	921
54.9	10.6	943
73.2	10.3	974
91.4	11.7	858
109.7	15.7	638
128.0	35.5	282
146.3	34.9	286
164.6	33.8	296
182.9	32.1	311
201.2	15.5	644
219.5	62.2	161
237.7	65.2	153
256.0	89.5	112
274.3	112.1	89

Plot 5

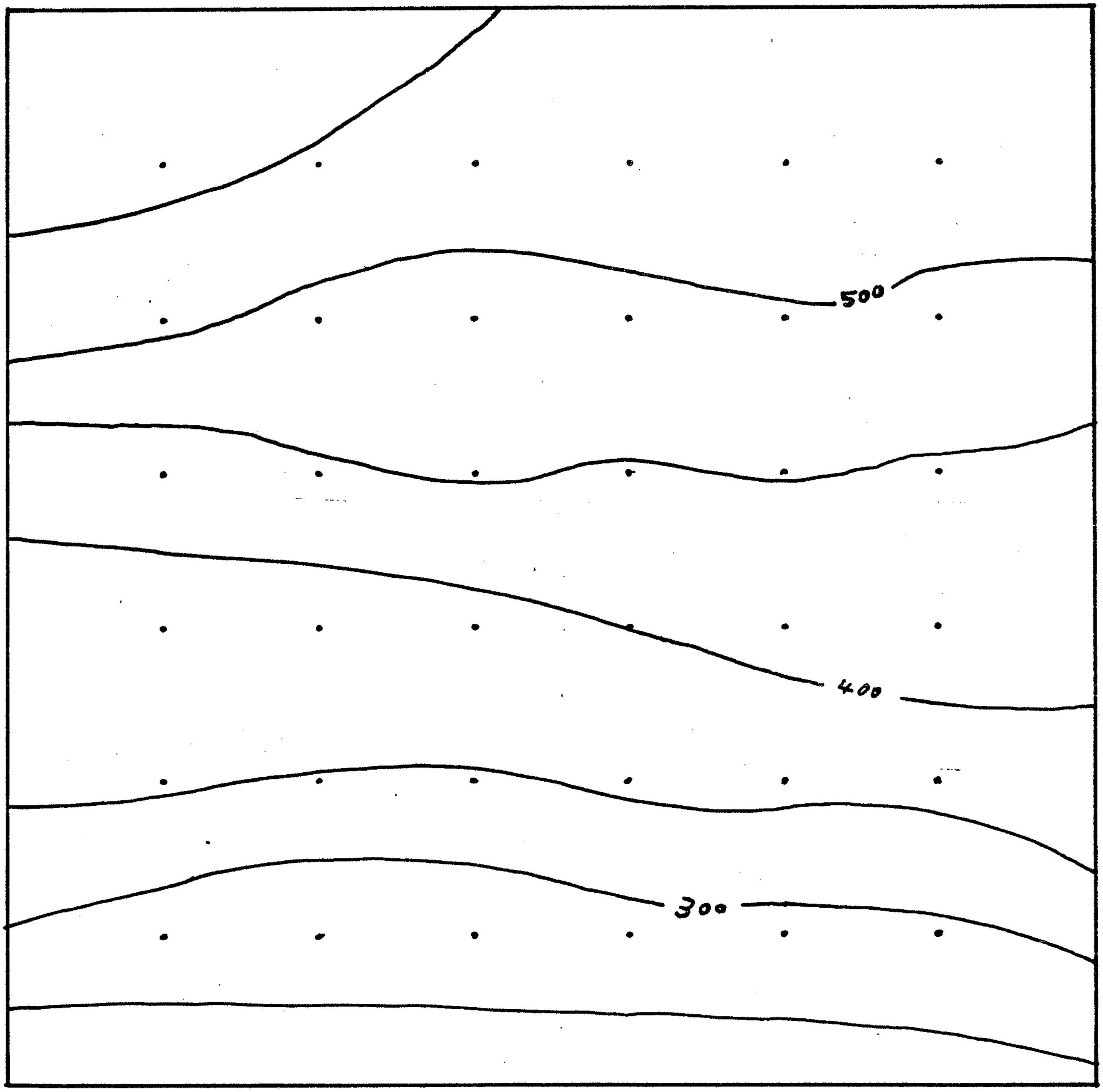

WENNER PARTIAL CONTOUR – SMALL GRID – A=3m
CONDUCTIVITIES IN MICROMHOS/CENTIMETER
TOP OF PAGE IS EAST

Plot 6

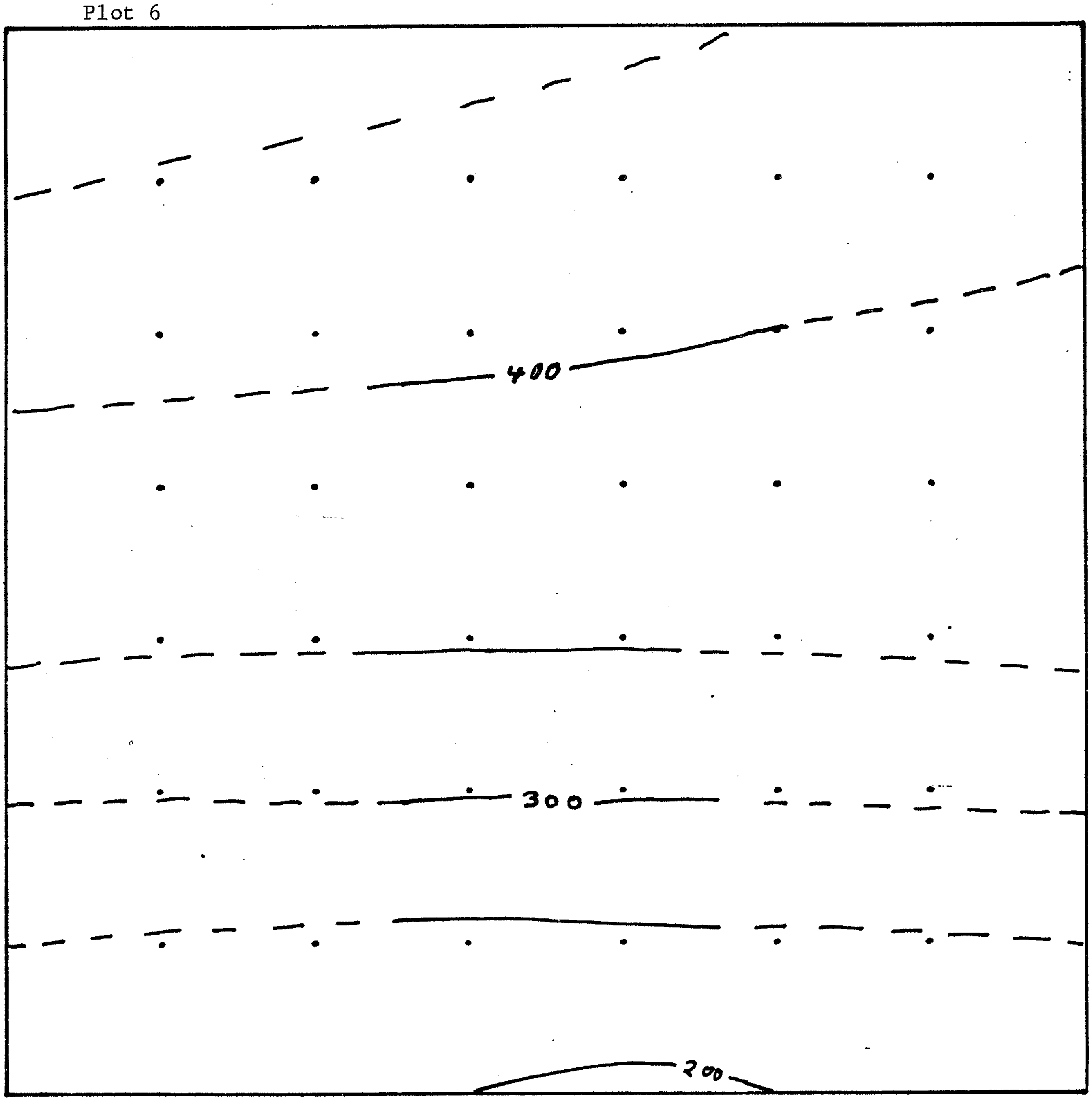

WENNER PARTIAL CONTOURS – SMALL GRID – A = 6m

CONDUCTIVITIES IN MICROMHOS / CENTIMETER

TOP OF PAGE IS EAST

Plot 7

CONDUCTIVITY CONTOURS OF ELECTROSCAN DATA
PORTAGE, SMALL GRID, FOUR LEVELS

PHI-KAPPA ITERATIONS PERFORMED=20   DEPTH UNIT=1

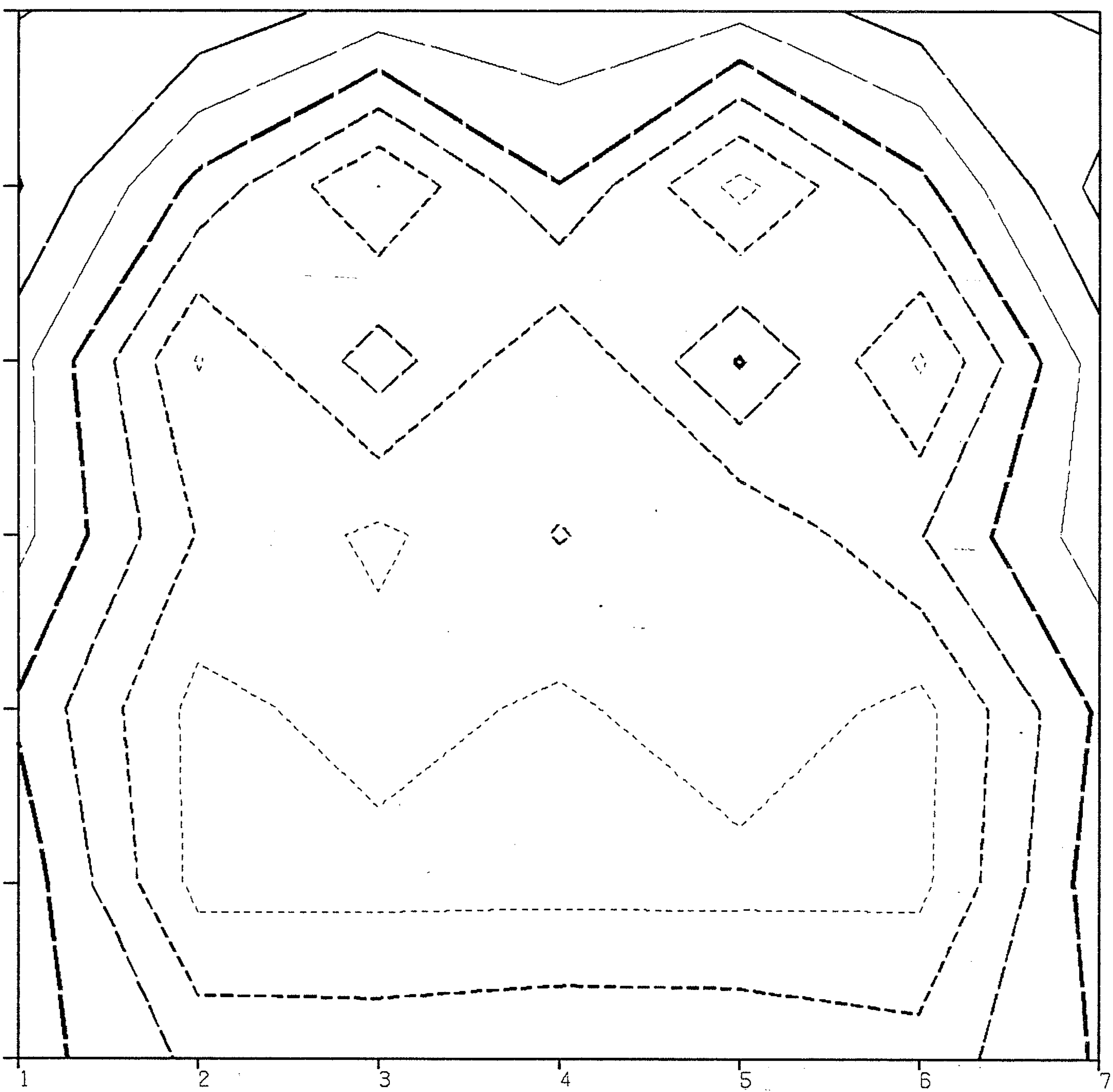

LEGEND: KAPPA ------- 61 ---- 124 — — 187 ▬ ▬ 250 ——— 313 ——— 376 ——— 439

CONTOURS IN UNSCALED CONDUCTIVITY UNITS

TOP OF PAGE IS EAST

Plot 8

CONDUCTIVITY CONTOURS OF ELECTROSCAN DATA
PORTAGE, SMALL GRID, FOUR LEVELS

PHI-KAPPA ITERATIONS PERFORMED=20 DEPTH UNIT=2

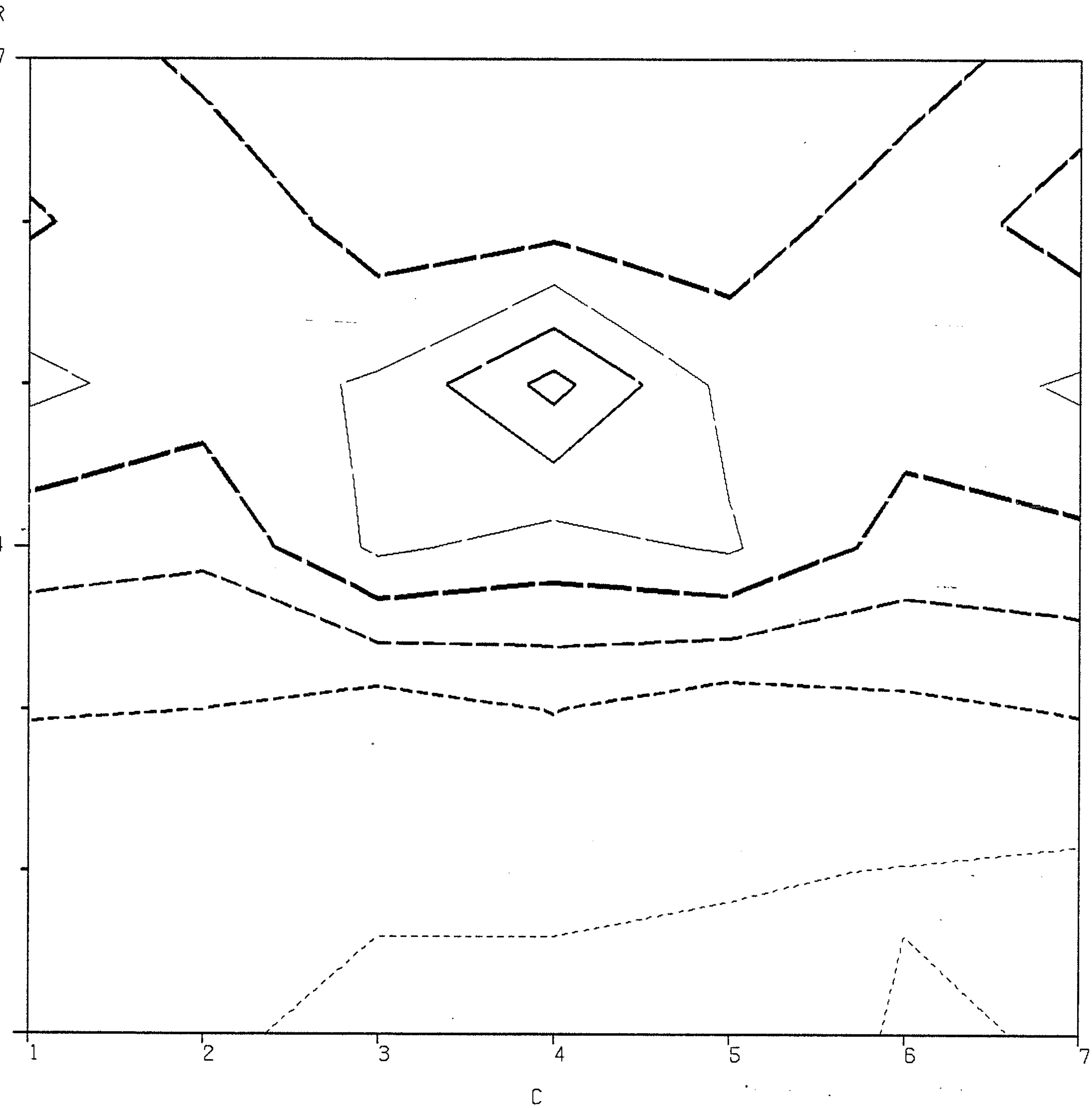

LEGEND: KAPPA

124.8	271.2	417.6
564.0	710.4	856.8
1003.2		

CONTOURS IN UNSCALED CONDUCTIVITY UNITS

TOP OF PAGE IS EAST

Plot 9

CONDUCTIVITY CONTOURS OF ELECTROSCAN DATA
PORTAGE, SMALL GRID, FOUR LEVELS

PHI-KAPPA ITERATIONS PERFORMED=20   DEPTH UNIT=3

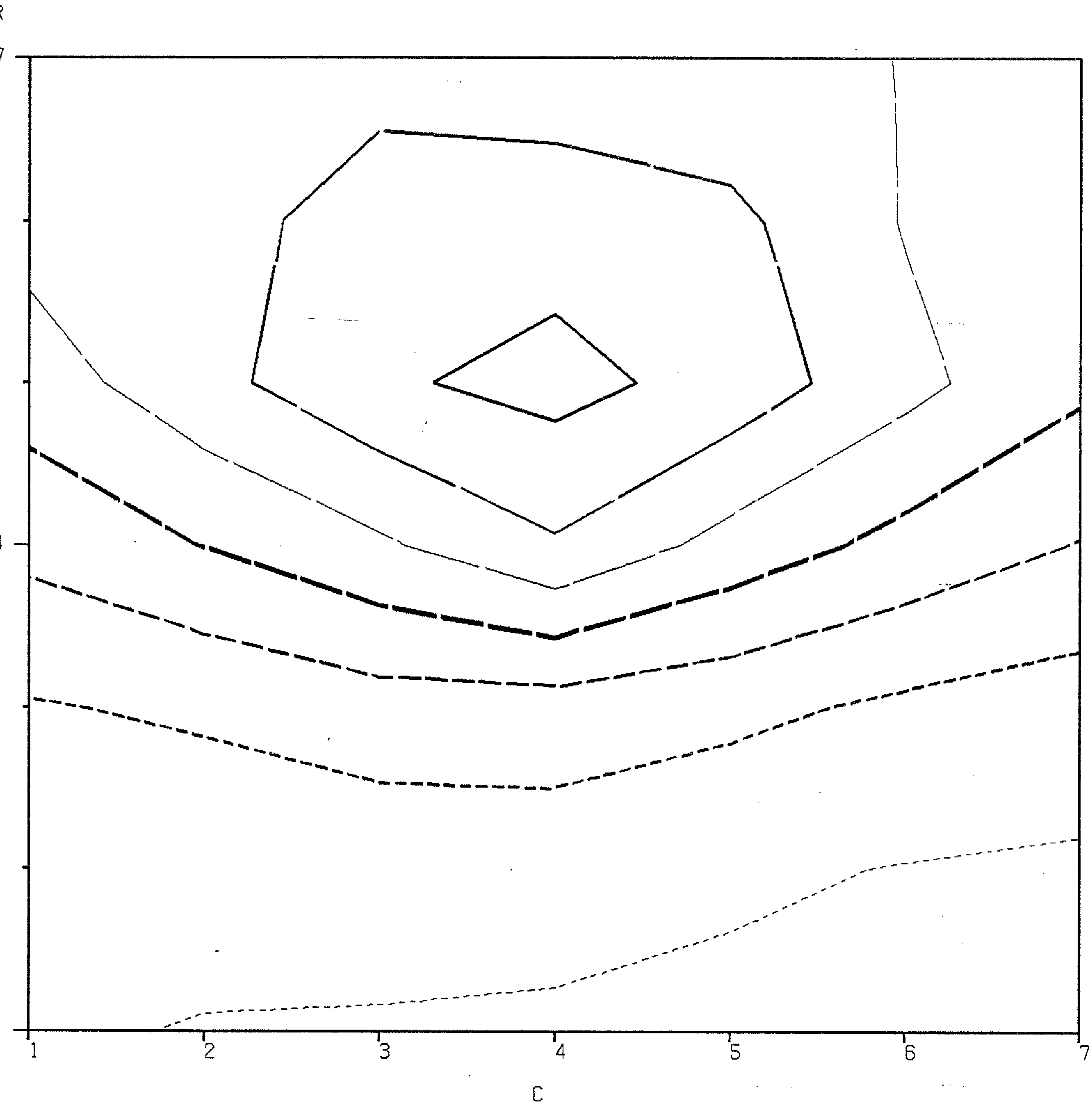

LEGEND: KAPPA 132.4 265.6 398.8 532.0 665.2 798.4 931.6

CONTOURS IN UNSCALED CONDUCTIVITY UNITS

TOP OF PAGE IS EAST

Plot 10

CONDUCTIVITY CONTOURS OF ELECTROSCAN DATA
PORTAGE, SMALL GRID, FOUR LEVELS

PHI-KAPPA ITERATIONS PERFORMED=20 DEPTH UNIT=4

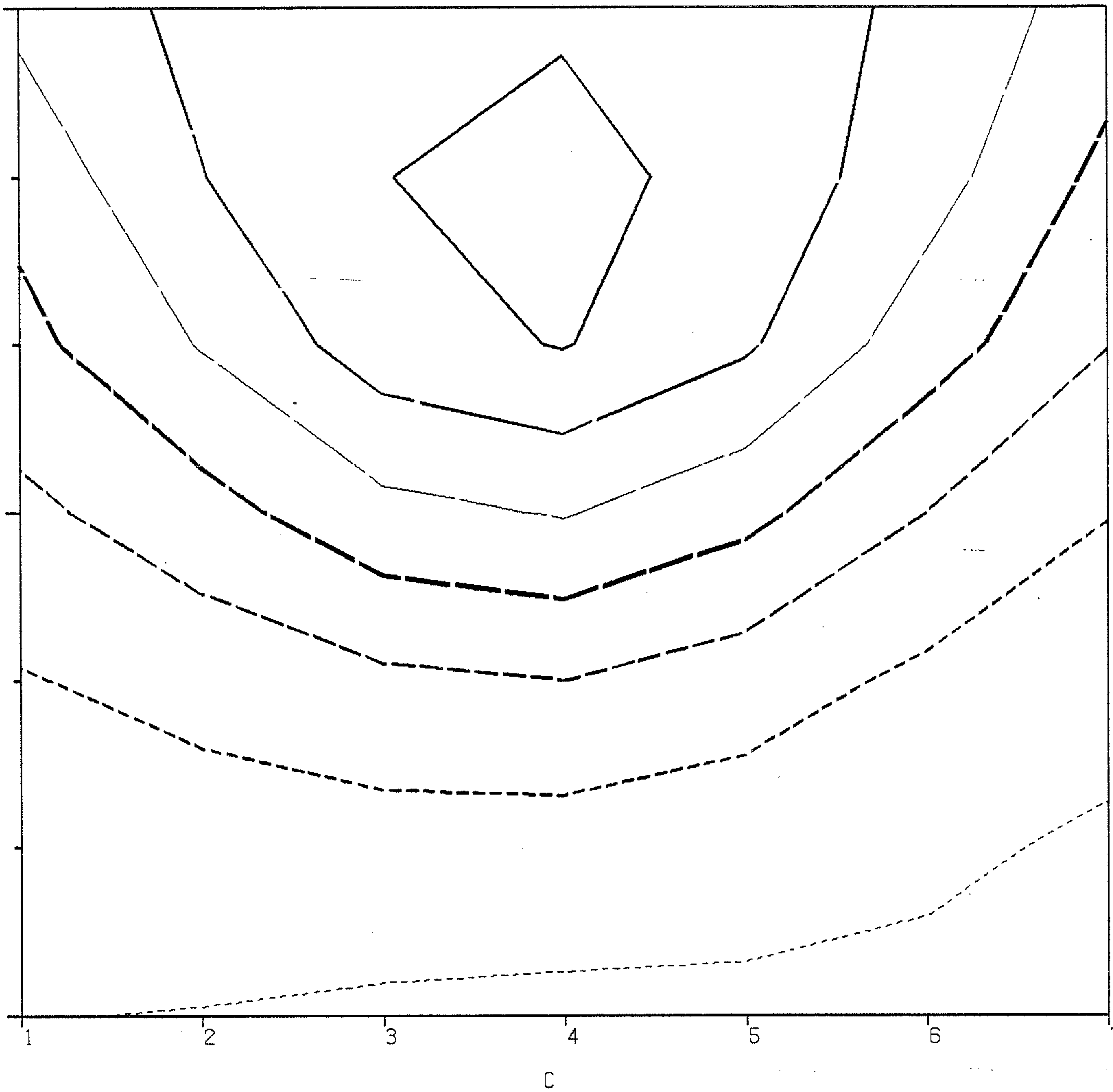

LEGEND: KAPPA

156.4	301.6	446.8
592.0	737.2	882.4
1027.6		

CONTOURS IN UNSCALED CONDUCTIVITY UNITS

TOP OF PAGE IS EAST

Plot 11

CONDUCTIVITY CONTOURS OF ELECTROSCAN DATA
PORTAGE, SMALL GRID, FOUR LEVELS

PHI-KAPPA ITERATIONS PERFORMED=100   DEPTH UNIT=1

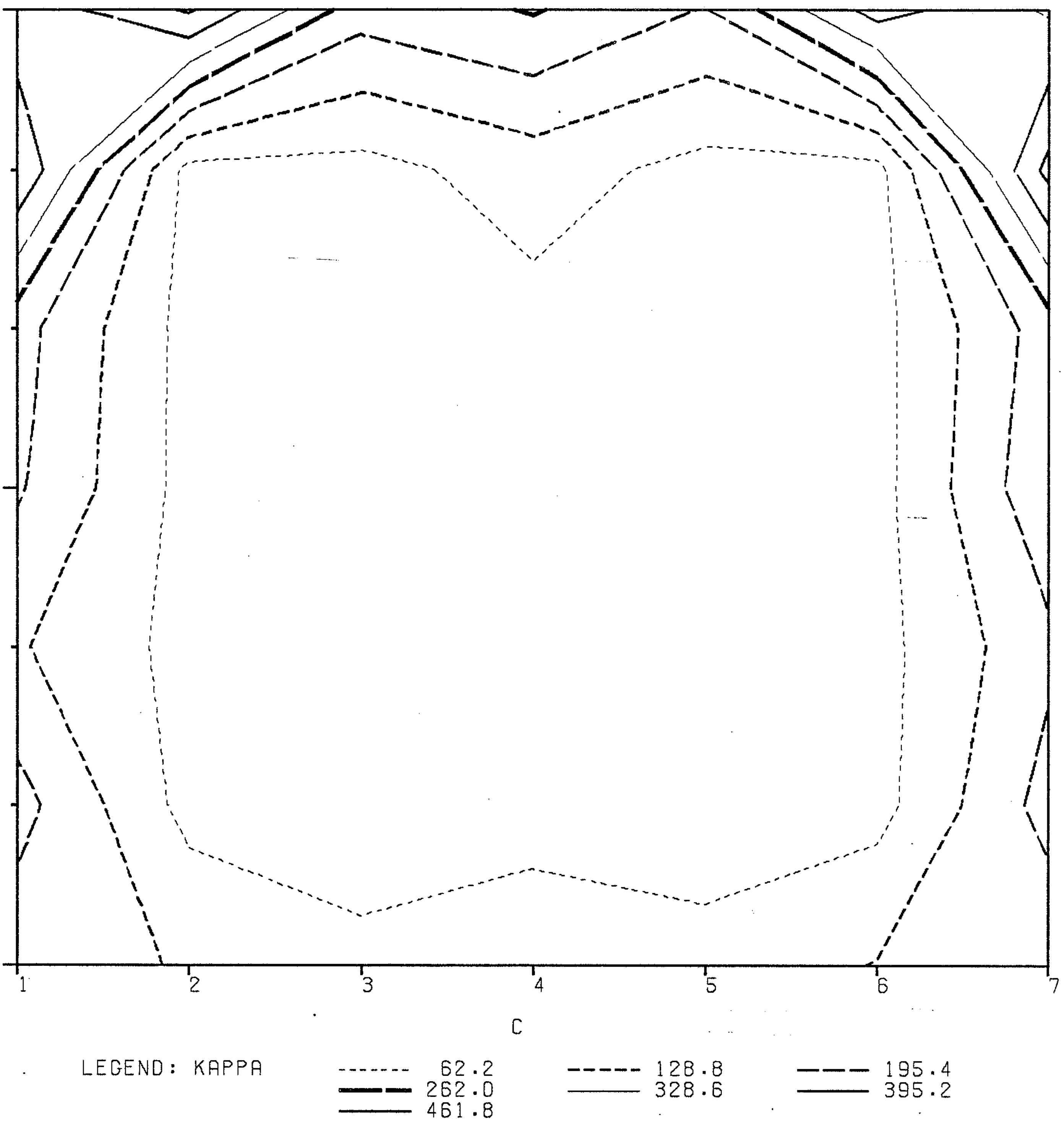

CONTOURS IN UNSCALED CONDUCTIVITY UNITS

TOP OF PAGE IS EAST

Plot 12

CONDUCTIVITY CONTOURS OF ELECTROSCAN DATA
PORTAGE, SMALL GRID, FOUR LEVELS

PHI-KAPPA ITERATIONS PERFORMED=100   DEPTH UNIT=2

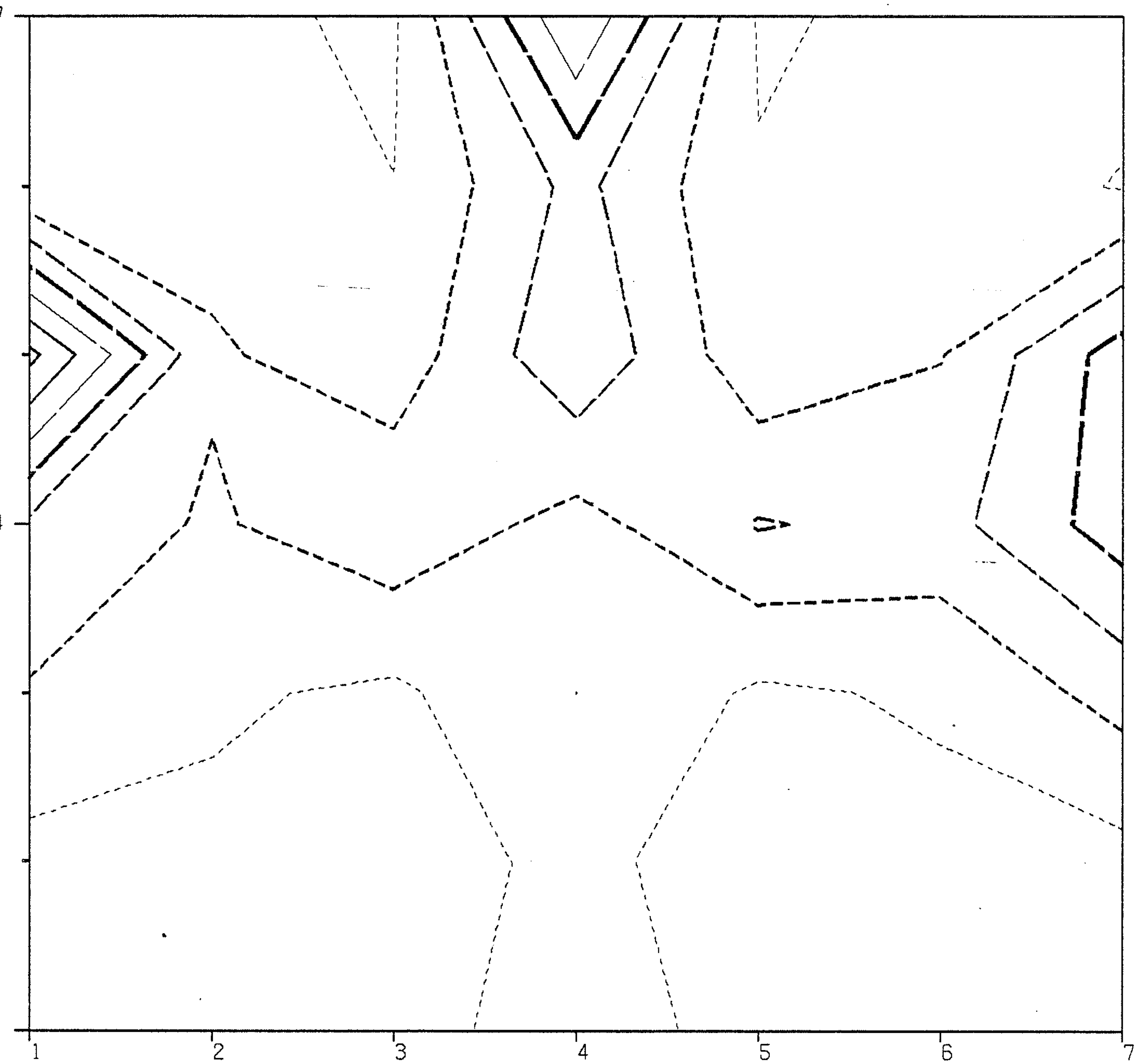

LEGEND: KAPPA
323.6
1174.4
2025.2
2876.0
3726.8
4577.6
5428.4

CONTOURS IN UNSCALED CONDUCTIVITY UNITS

TOP OF PAGE IS EAST

Plot 13

CONDUCTIVITY CONTOURS OF ELECTROSCAN DATA
PORTAGE, SMALL GRID, FOUR LEVELS

PHI-KAPPA ITERATIONS PERFORMED=100   DEPTH UNIT=3

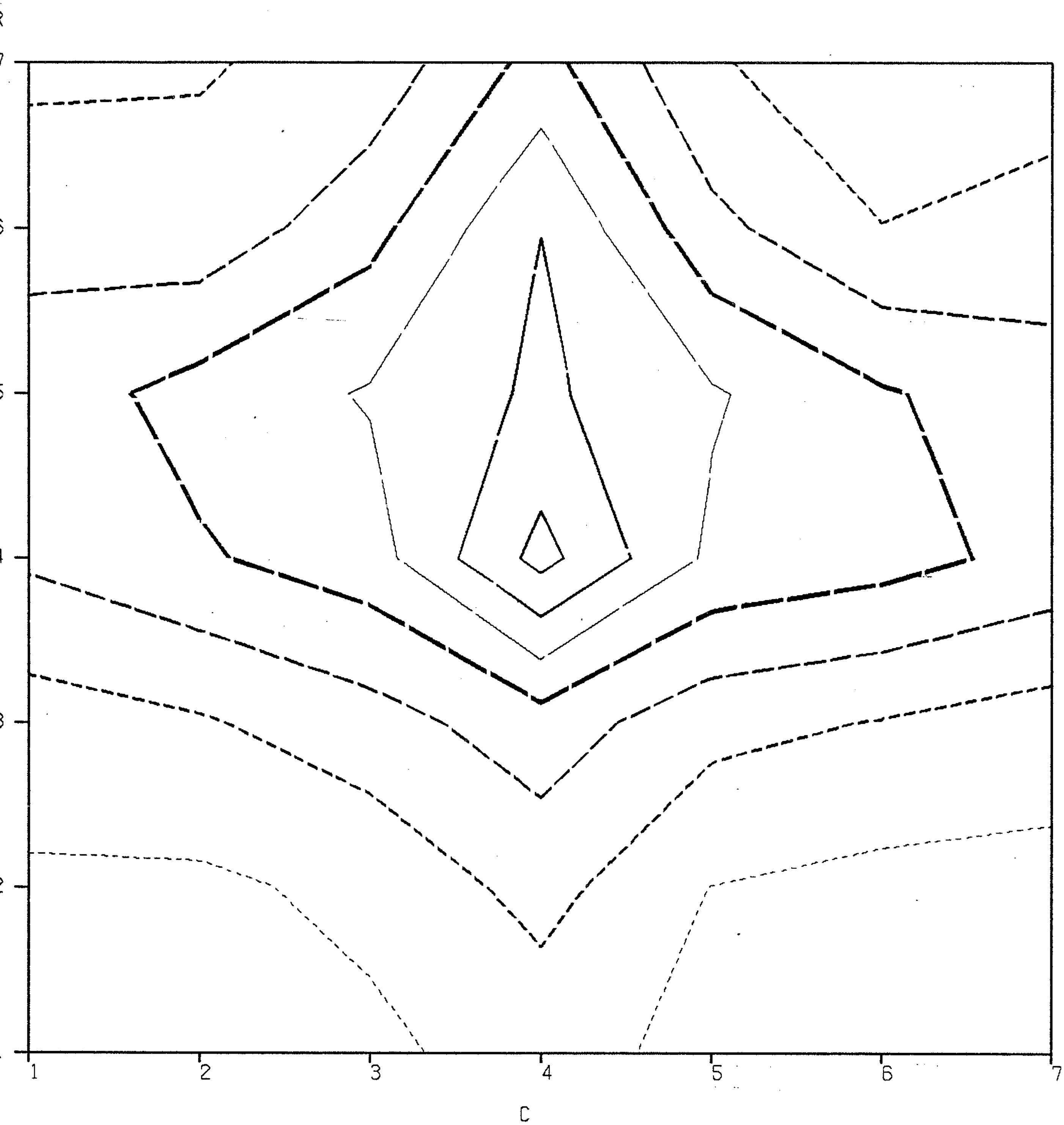

LEGEND: KAPPA ------- 154 ---- 496 — — 838 — — 1180
——— 1522 ——— 1864 ——— 2206

CONTOURS IN UNSCALED CONDUCTIVITY UNITS

TOP OF PAGE IS EAST

Plot 14

CONDUCTIVITY CONTOURS OF ELECTROSCAN DATA PORTAGE, SMALL GRID, FOUR LEVELS

PHI-KAPPA ITERATIONS PERFORMED=100   DEPTH UNIT=4

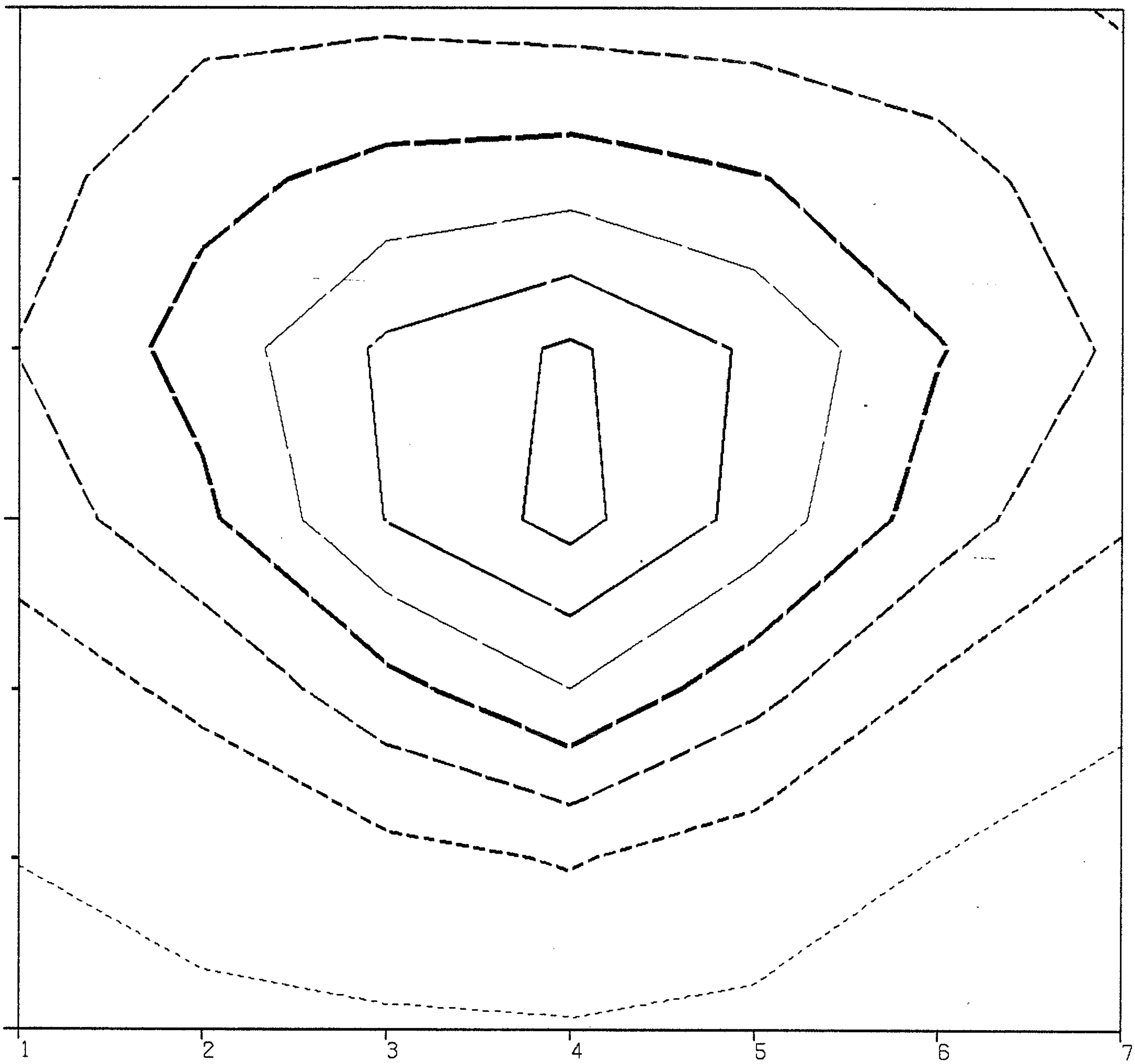

LEGEND: KAPPA

161.2	512.8	864.4
1216.0	1567.6	1919.2
2270.8		

CONTOURS IN UNSCALED CONDUCTIVITY UNITS

TOP OF PAGE IS EAST

Plot 15

CONDUCTIVITY CONTOURS OF ELECTROSCAN DATA
PORTAGE, SMALL GRID, FOUR LEVELS

PHI-KAPPA ITERATIONS PERFORMED=200   DEPTH UNIT=1

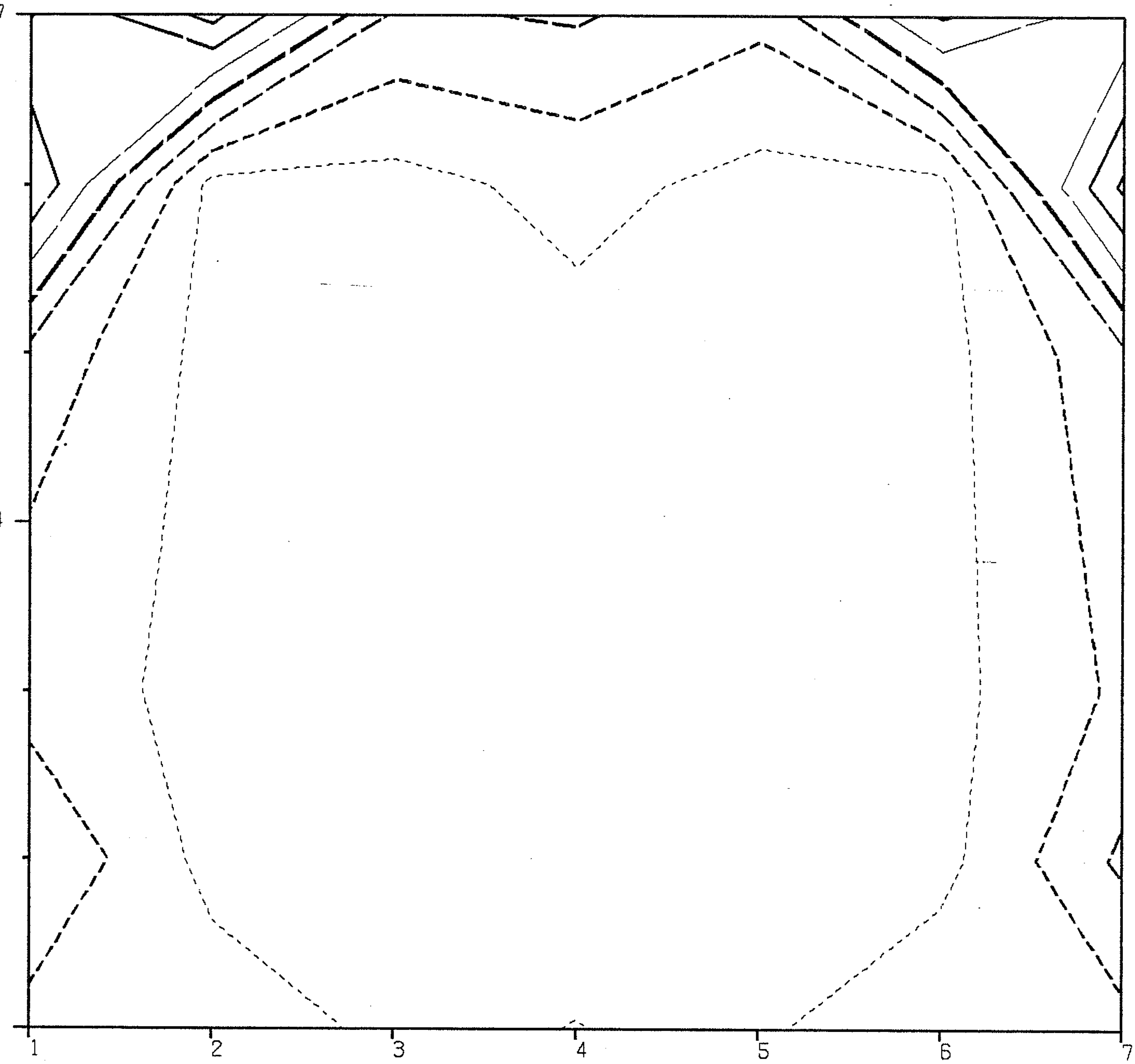

LEGEND: KAPPA 62.8 131.2 199.6 268.0 336.4 404.8 473.2

CONTOURS IN UNSCALED CONDUCTIVITY UNITS

TOP OF PAGE IS EAST

Plot 16

CONDUCTIVITY CONTOURS OF ELECTROSCAN DATA
PORTAGE, SMALL GRID, FOUR LEVELS

PHI-KAPPA ITERATIONS PERFORMED=200   DEPTH UNIT=2

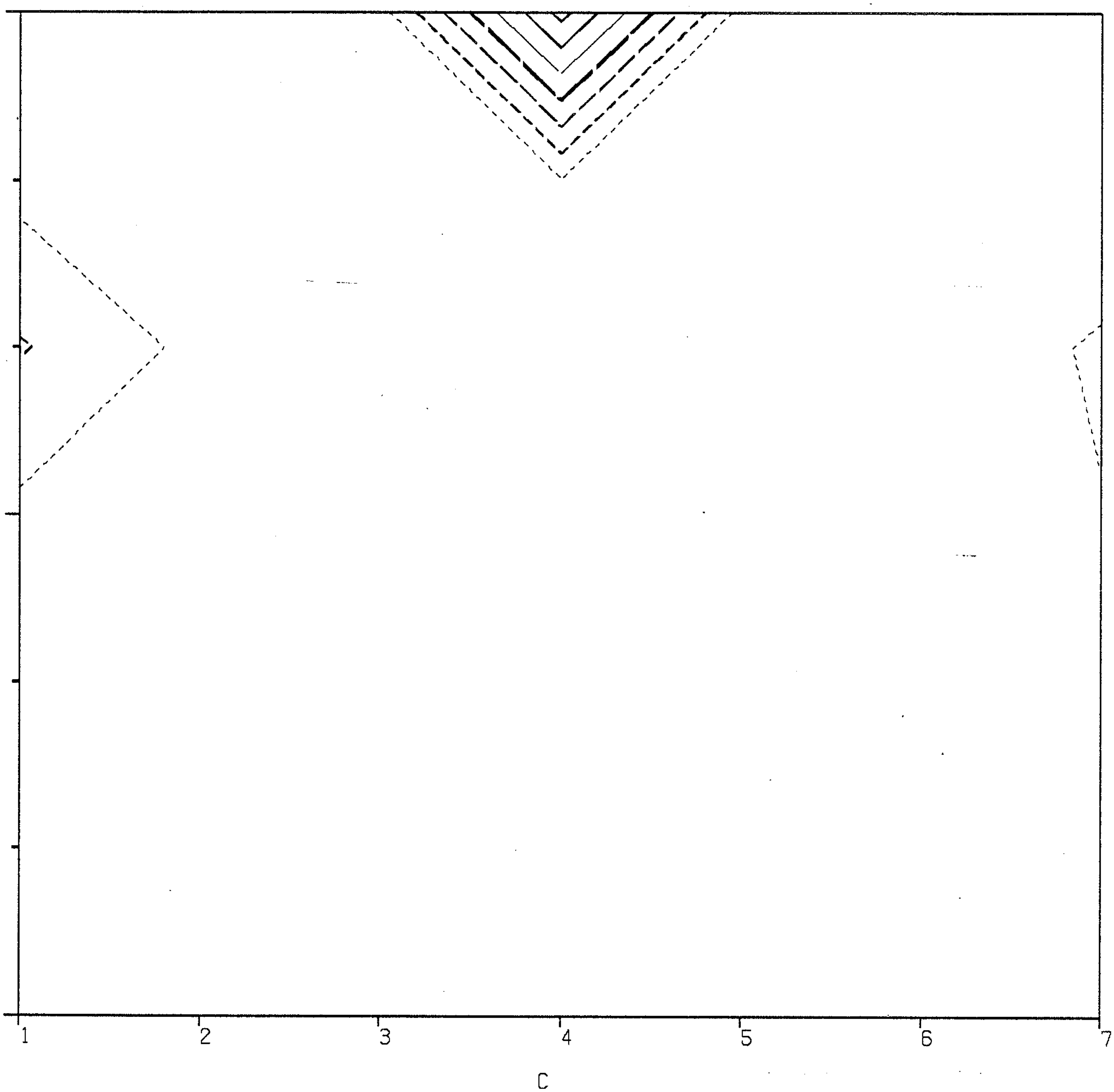

LEGEND: KAPPA

10998.6	43874.4	76750.2
109626.0	142501.8	175377.6
208253.4		

CONTOURS IN UNSCALED CONDUCTIVITY UNITS

TOP OF PAGE IS EAST

Plot 17

CONDUCTIVITY CONTOURS OF ELECTROSCAN DATA
PORTAGE, SMALL GRID, FOUR LEVELS

PHI-KAPPA ITERATIONS PERFORMED=200   DEPTH UNIT=3

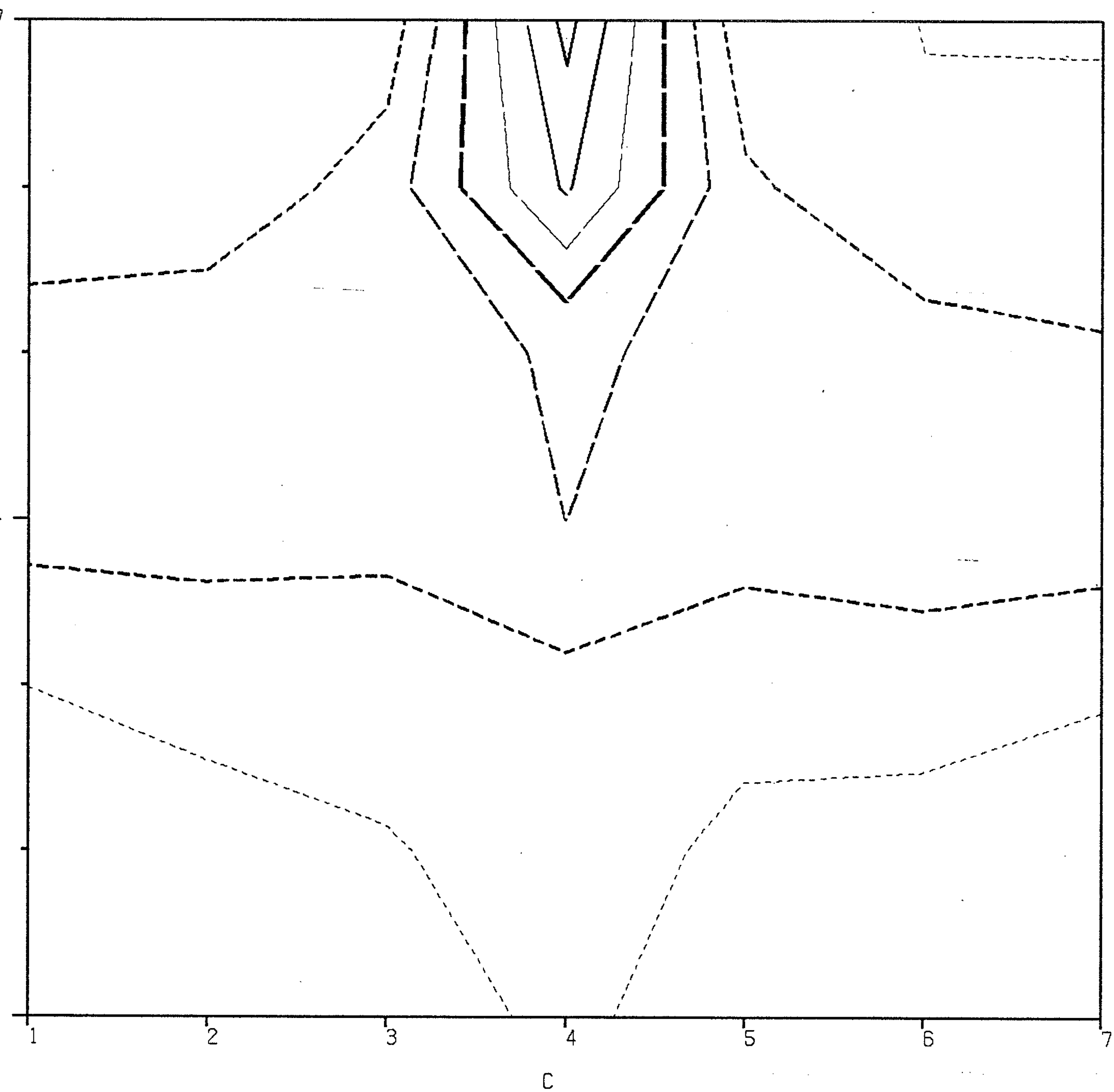

LEGEND: KAPPA

-------	303.8
-----	1095.2
— — —	1886.6
▬ ▬	2678.0
———	3469.4
———	4260.8
———	5052.2

CONTOURS IN UNSCALED CONDUCTIVITY UNITS

TOP OF PAGE IS EAST

Plot 18

CONDUCTIVITY CONTOURS OF ELECTROSCAN DATA
PORTAGE, SMALL GRID, FOUR LEVELS

PHI-KAPPA ITERATIONS PERFORMED=200   DEPTH UNIT=4

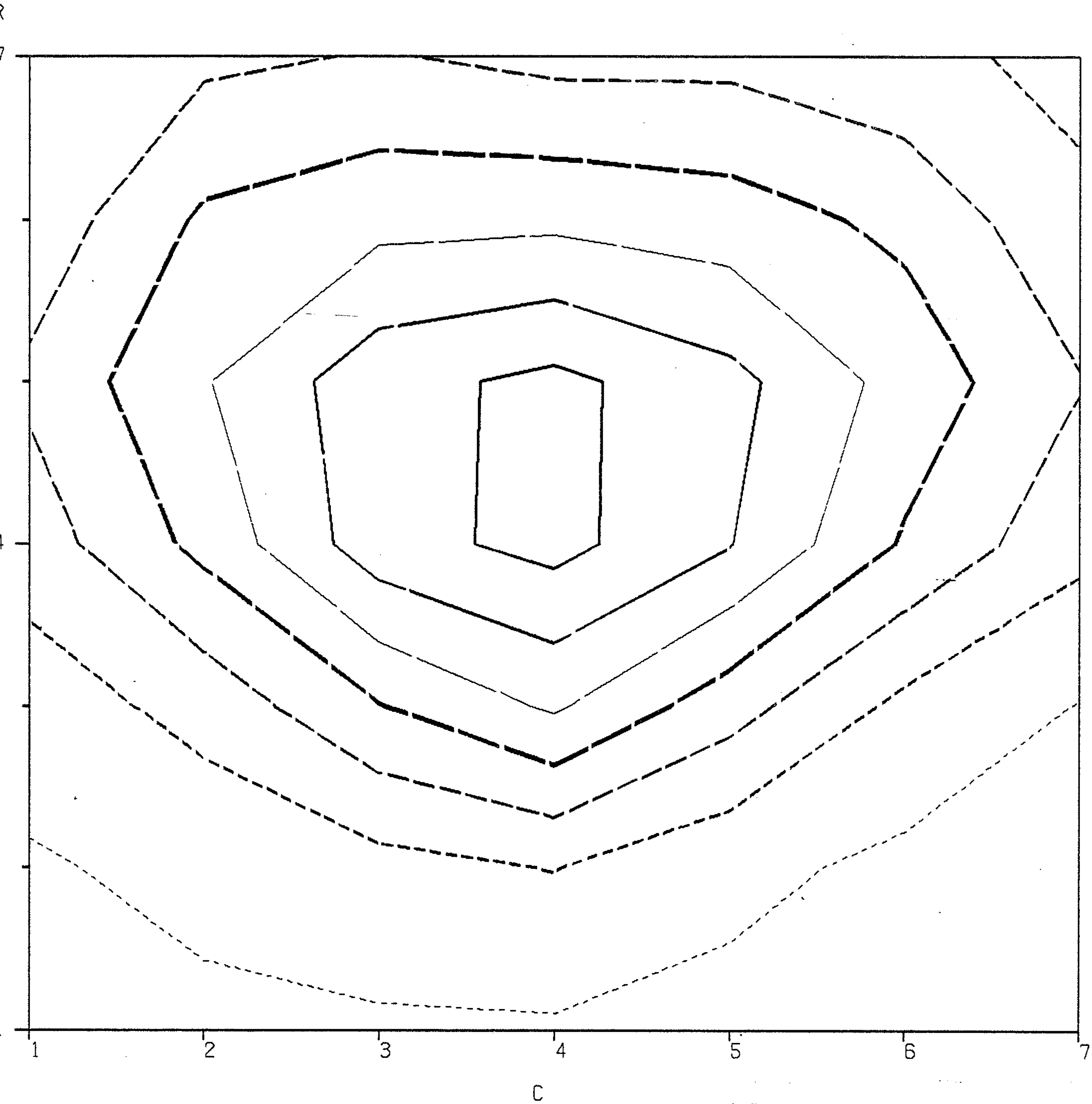

LEGEND: KAPPA

156.8 · 507.2 · 857.6 · 1208.0 · 1558.4 · 1908.8 · 2259.2

CONTOURS IN UNSCALED CONDUCTIVITY UNITS

TOP OF PAGE IS EAST

Plot 19

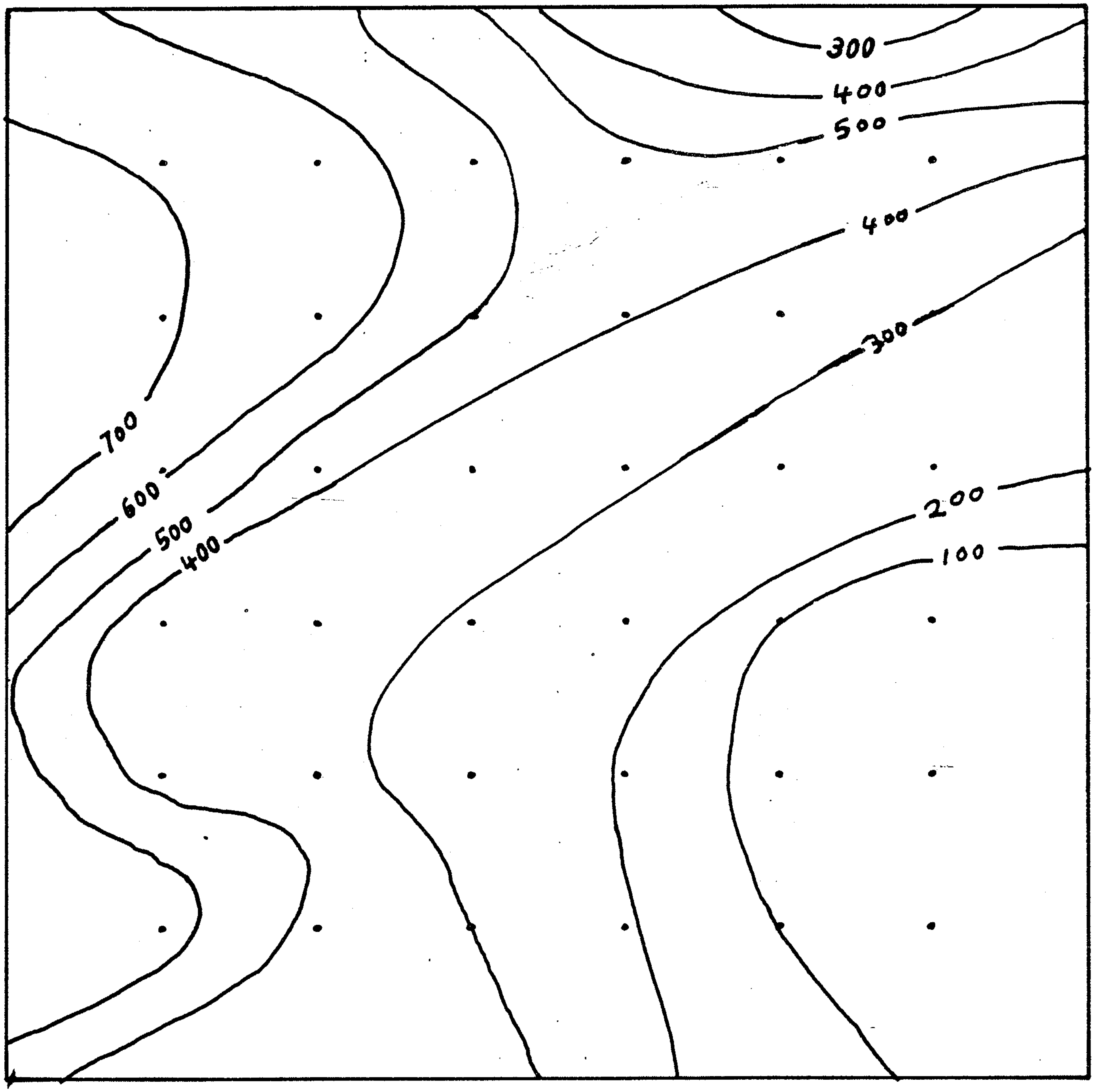

WENNER PARTIAL CONTOURS — LARGE GRID — A=12 m

CONDUCTIVITIES IN MICROMHOS / CENTIMETERS

TOP OF PAGE IS EAST

Plot 20

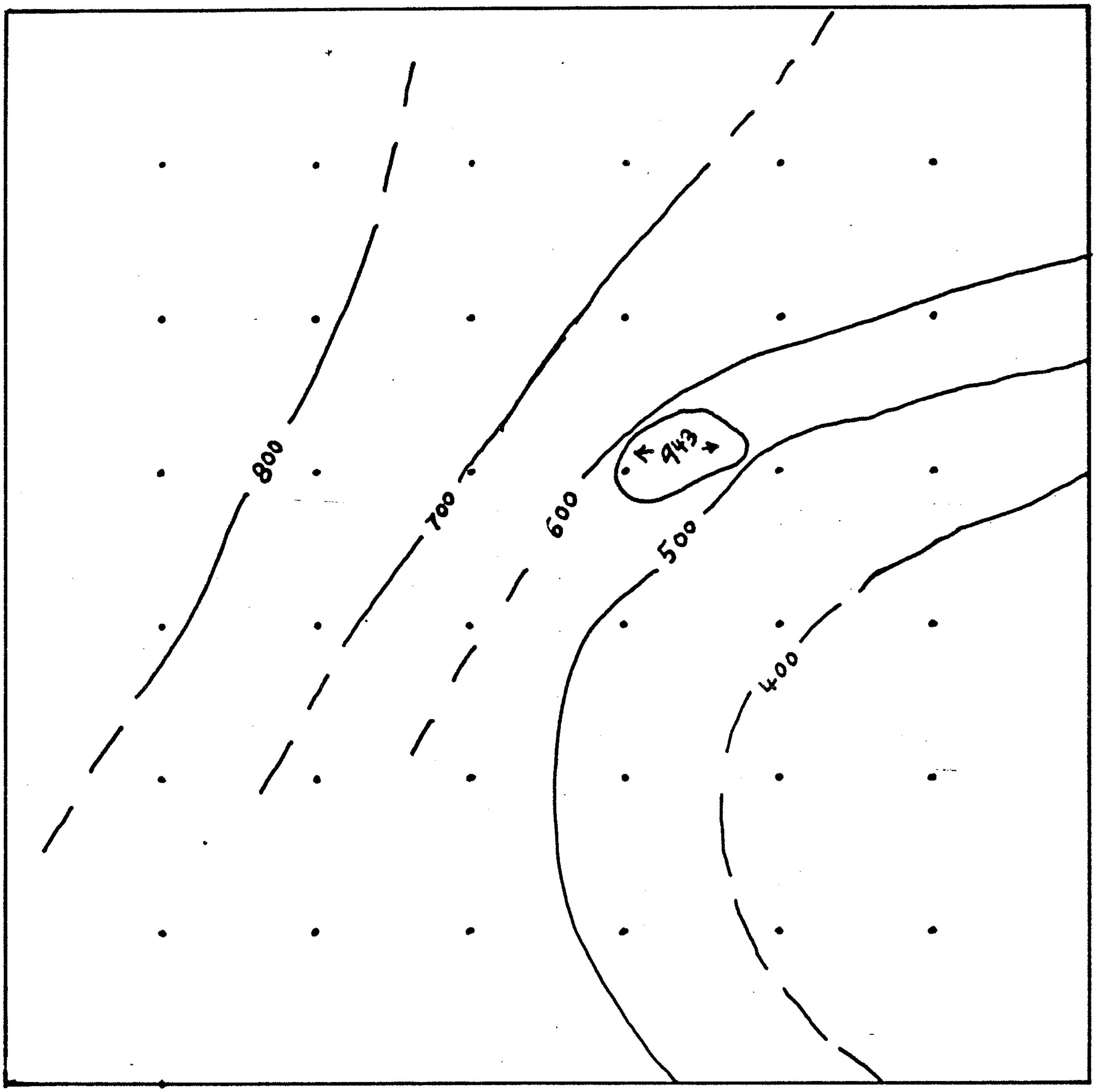

WENNER PARTIAL CONTOURS — LARGE GRID — A=24 m

CONDUCTIVITIES IN MICROMHOS / CENTIMETER

TOP OF PAGE IS EAST

Plot 21

CONDUCTIVITY CONTOURS OF ELECTROSCAN DATA
PORTAGE, LARGE GRID, FOUR LEVELS

PHI-KAPPA ITERATIONS PERFORMED=20   DEPTH UNIT=1

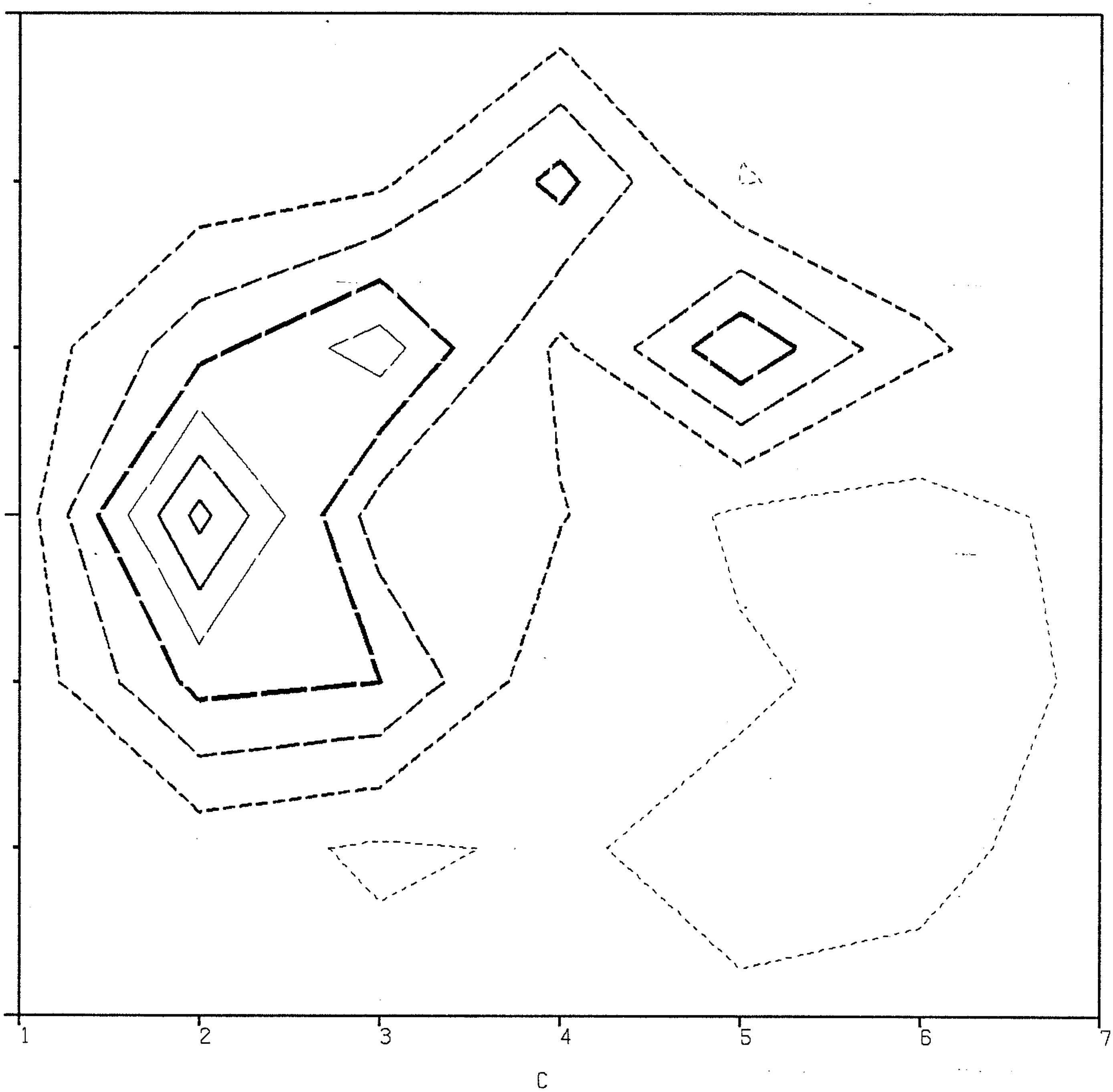

LEGEND: KAPPA
51.5
176.0
300.5
425.0
549.5
674.0
798.5

CONTOURS IN UNSCALED CONDUCTIVITY UNITS

TOP OF PAGE IS EAST

Plot 22

CONDUCTIVITY CONTOURS OF ELECTROSCAN DATA
PORTAGE, LARGE GRID, FOUR LEVELS

PHI-KAPPA ITERATIONS PERFORMED=20   DEPTH UNIT=2

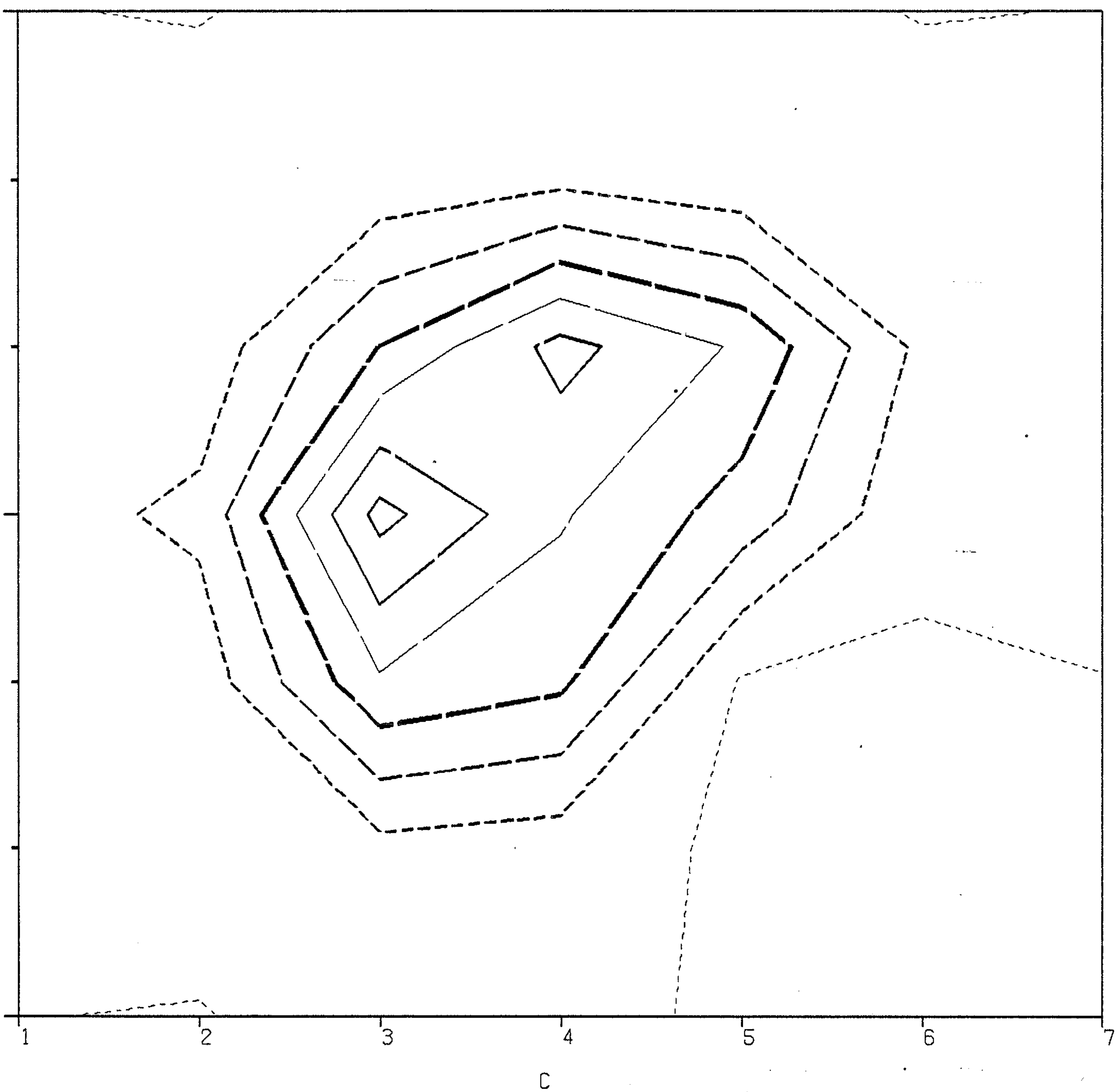

LEGEND: KAPPA

295.95	814.80	1333.65
1852.50	2371.35	2890.20
3409.05		

CONTOURS IN UNSCALED CONDUCTIVITY UNITS

TOP OF PAGE IS EAST

Plot 23

CONDUCTIVITY CONTOURS OF ELECTROSCAN DATA
PORTAGE, LARGE GRID, FOUR LEVELS

PHI-KAPPA ITERATIONS PERFORMED=20   DEPTH UNIT=3

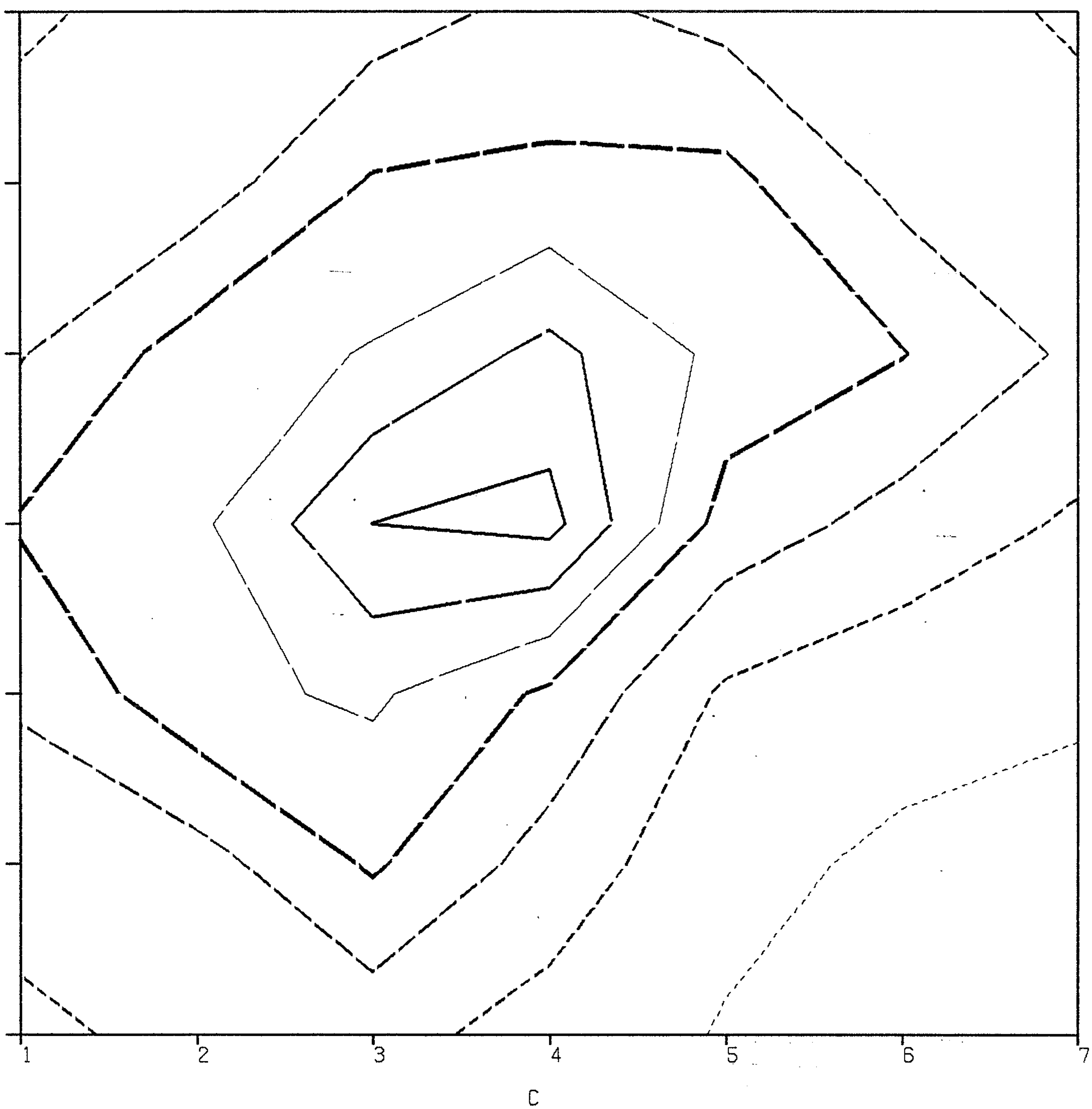

LEGEND: KAPPA ------- 264 ------ 564 — — — 864 ▬ ▬ 1164 ——— 1464 ——— 1764 ——— 2064

CONTOURS IN UNSCALED CONDUCTIVITY UNITS

TOP OF PAGE IS EAST

Plot 24

CONDUCTIVITY CONTOURS OF ELECTROSCAN DATA
PORTAGE, LARGE GRID, FOUR LEVELS

PHI-KAPPA ITERATIONS PERFORMED=20 DEPTH UNIT=4

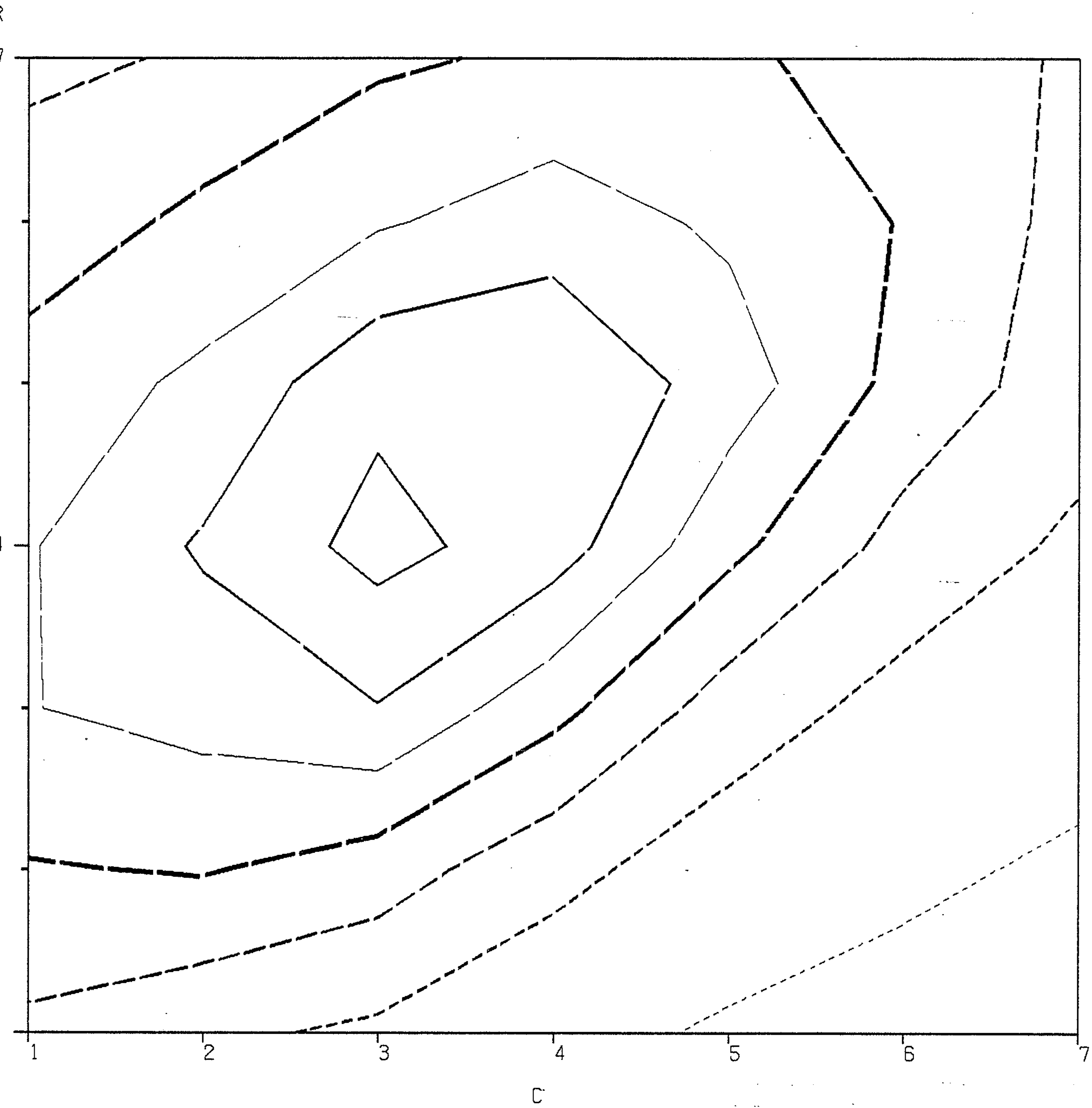

LEGEND: KAPPA

297.15	552.60	808.05
1063.50	1318.95	1574.40
1829.85		

CONTOURS IN UNSCALED CONDUCTIVITY UNITS

TOP OF PAGE IS EAST

Plot 25

CONDUCTIVITY CONTOURS OF ELECTROSCAN DATA
PORTAGE, LARGE GRID, FOUR LEVELS

PHI-KAPPA ITERATIONS PERFORMED=100   DEPTH UNIT=1

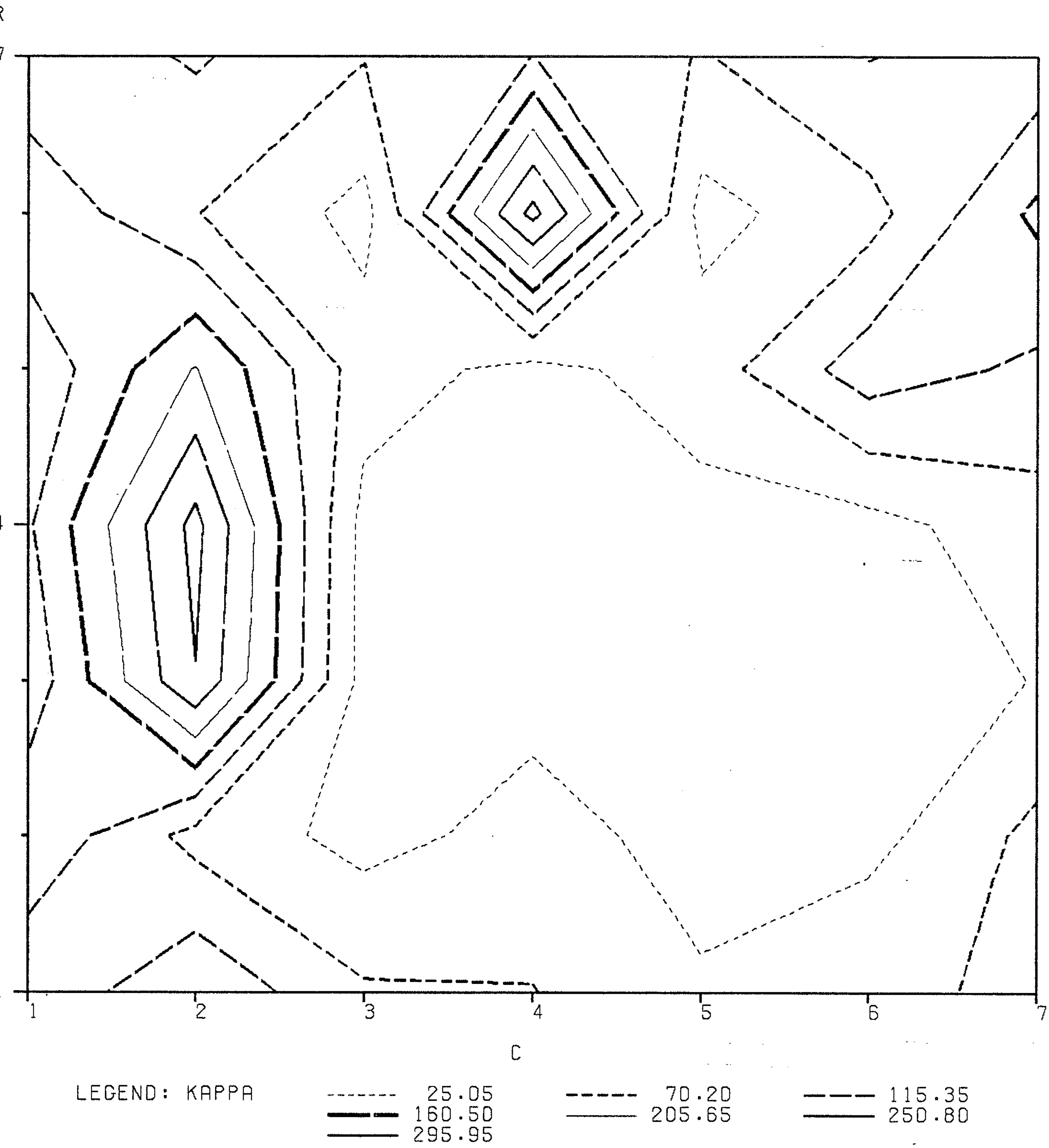

CONTOURS IN UNSCALED CONDUCTIVITY UNITS

TOP OF PAGE IS EAST

Plot 26

CONDUCTIVITY CONTOURS OF ELECTROSCAN DATA
PORTAGE, LARGE GRID, FOUR LEVELS

PHI-KAPPA ITERATIONS PERFORMED=100 DEPTH UNIT=2

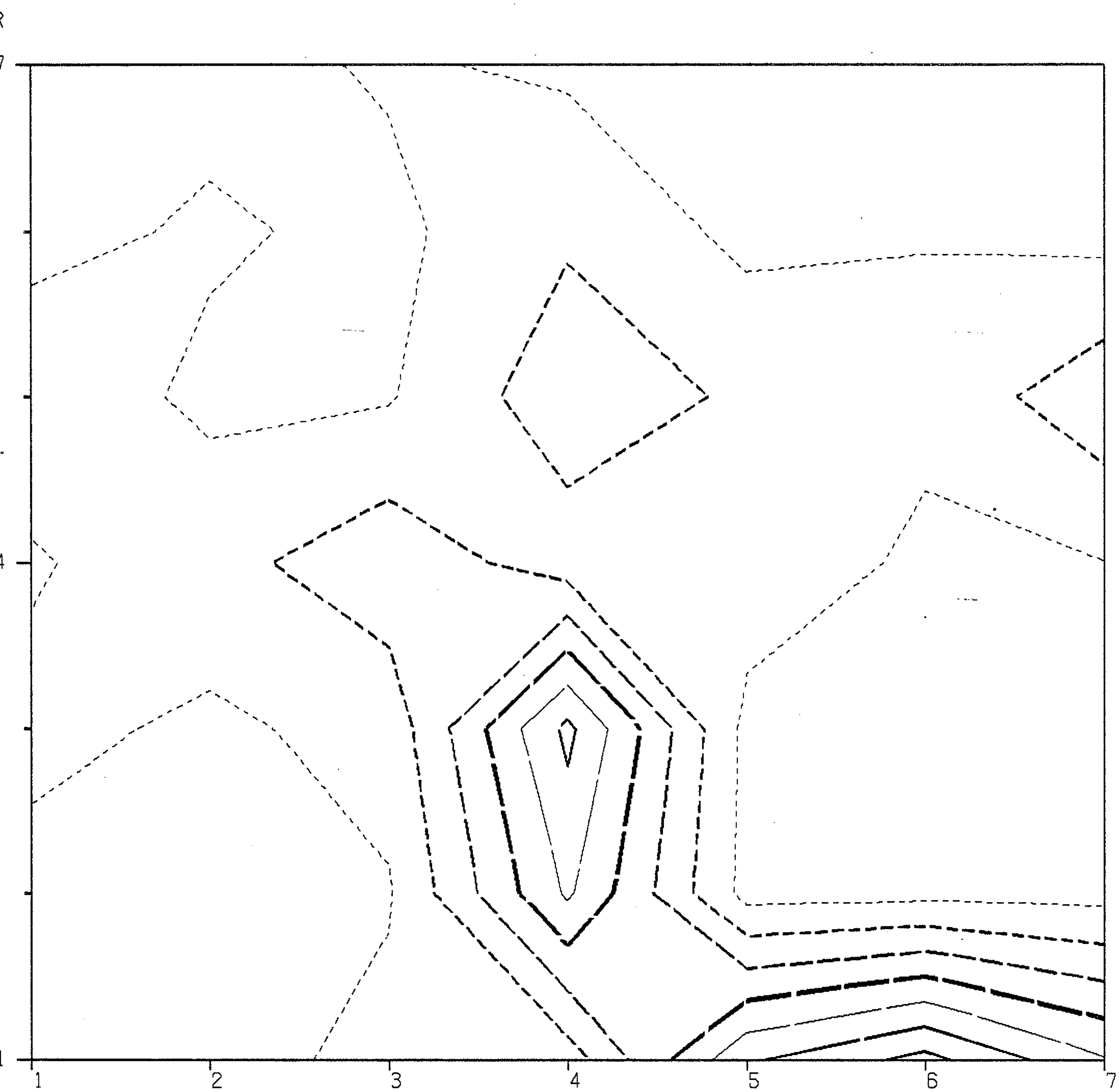

LEGEND: KAPPA

4537.5
18033.0
31528.5
45024.0
58519.5
72015.0
85510.5

CONTOURS IN UNSCALED CONDUCTIVITY UNITS

TOP OF PAGE IS EAST

Plot 27

CONDUCTIVITY CONTOURS OF ELECTROSCAN DATA
PORTAGE, LARGE GRID, FOUR LEVELS

PHI-KAPPA ITERATIONS PERFORMED=100   DEPTH UNIT=3

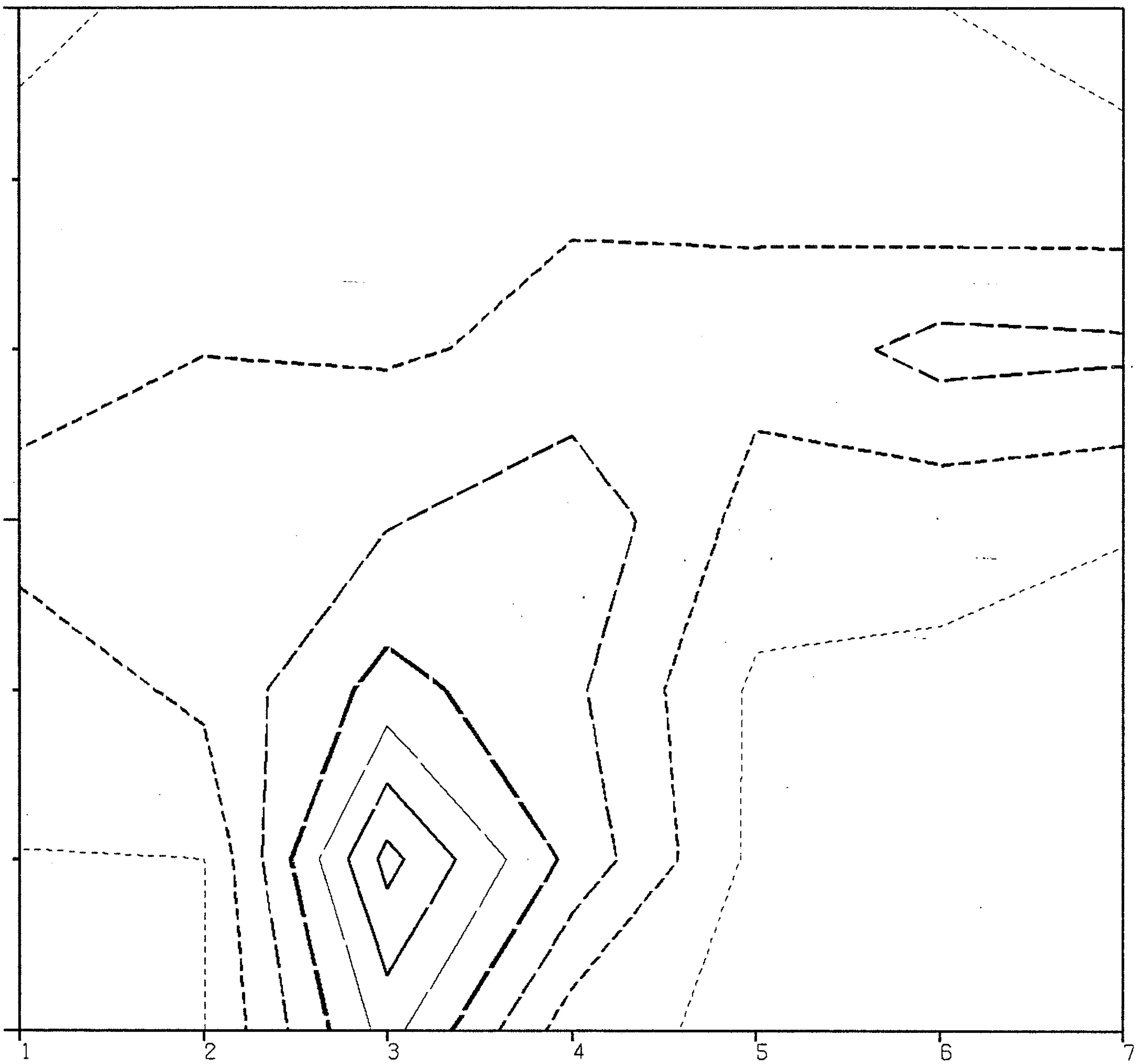

LEGEND: KAPPA

1385.7	5230.8	9075.9
12921.0	16766.1	20611.2
24456.3		

CONTOURS IN UNSCALED CONDUCTIVITY UNITS

TOP OF PAGE IS EAST

Plot 28

CONDUCTIVITY CONTOURS OF ELECTROSCAN DATA
PORTAGE, LARGE GRID, FOUR LEVELS

PHI-KAPPA ITERATIONS PERFORMED=100 DEPTH UNIT=4

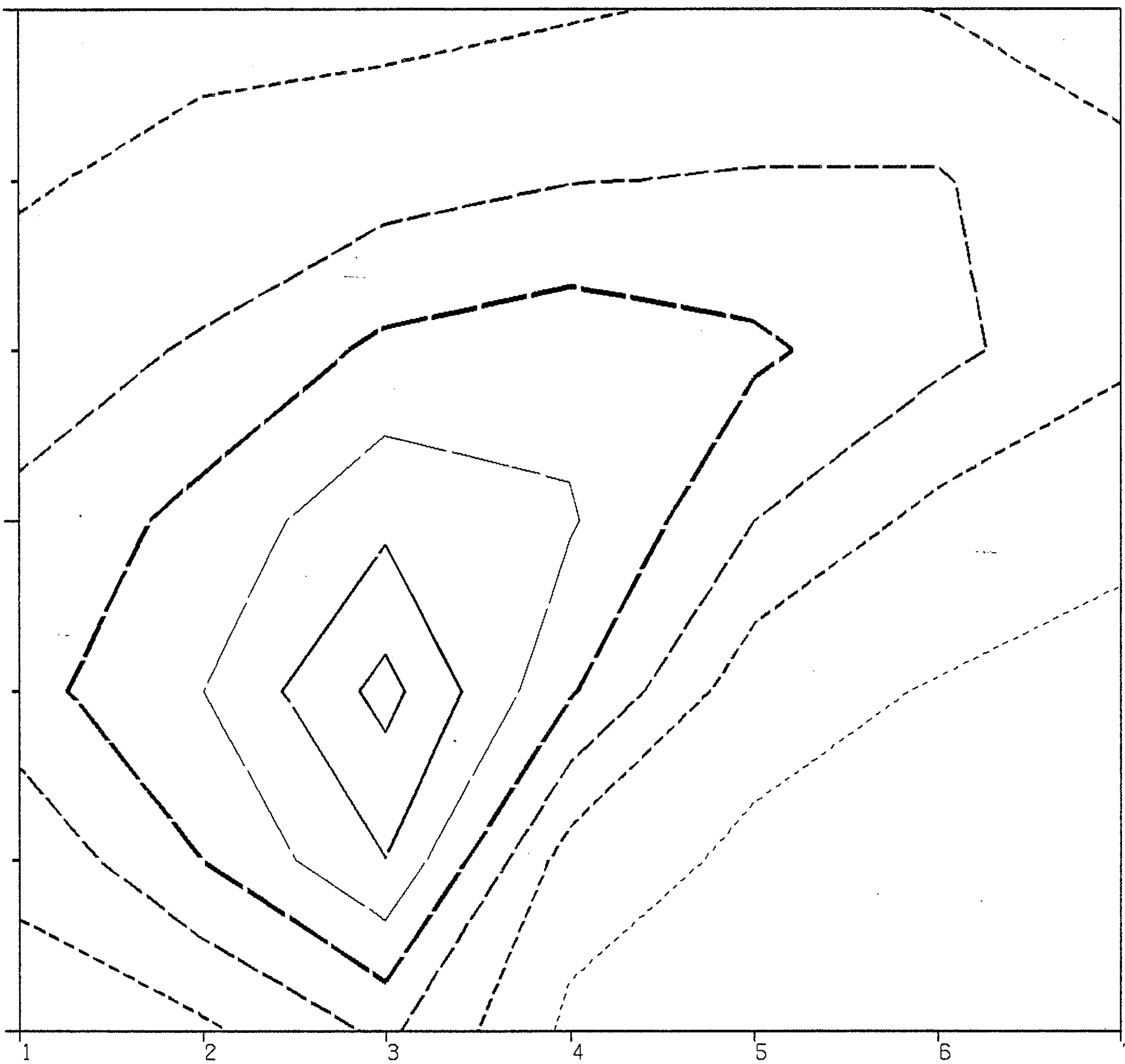

LEGEND: KAPPA

703.4	2312.6	3921.8
5531.0	7140.2	8749.4
10358.6		

CONTOURS IN UNSCALED CONDUCTIVITY UNITS

TOP OF PAGE IS EAST

Plot 29

CONDUCTIVITY CONTOURS OF ELECTROSCAN DATA
PORTAGE, LARGE GRID, FOUR LEVELS

PHI-KAPPA ITERATIONS PERFORMED=200   DEPTH UNIT=1

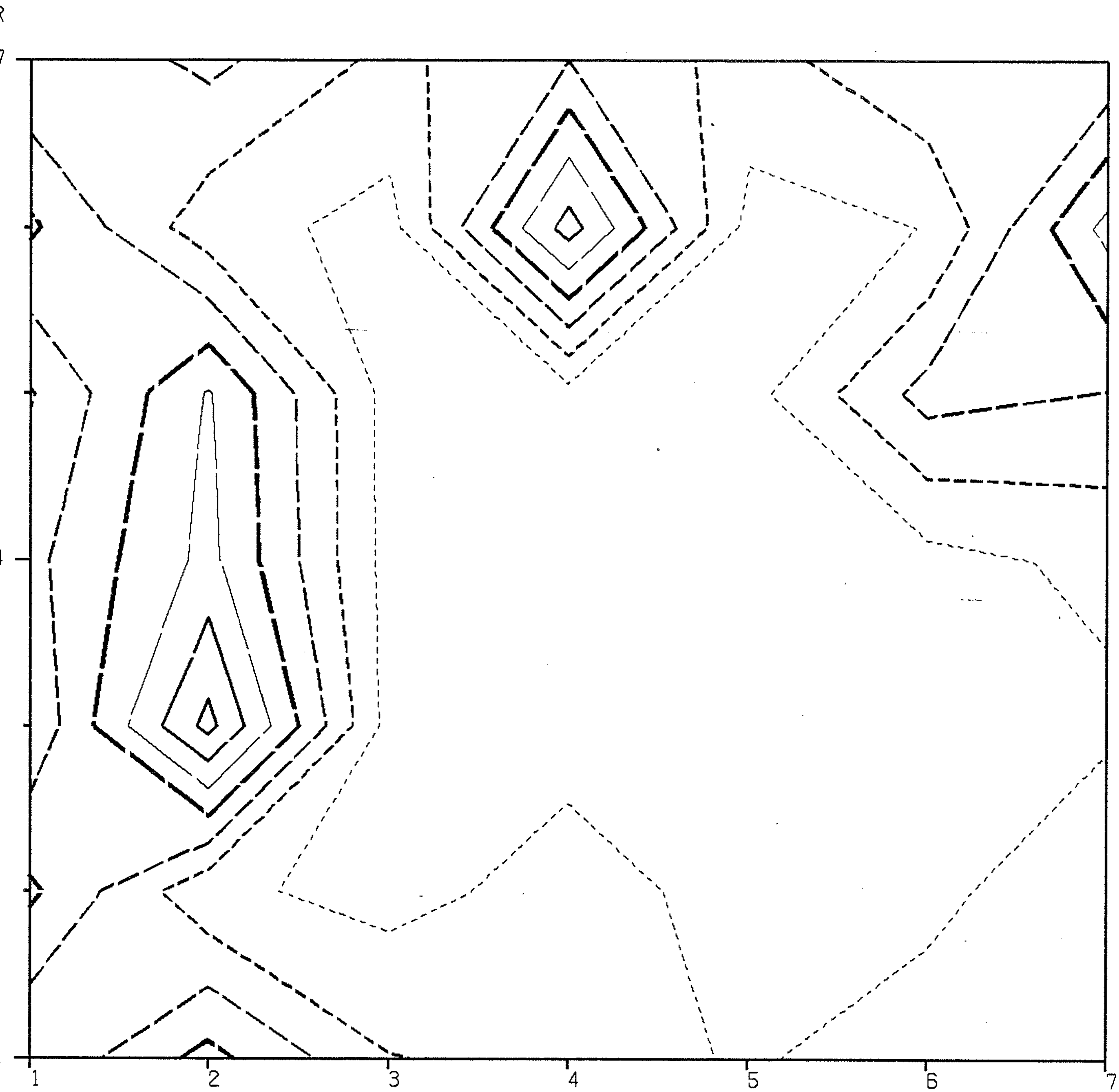

LEGEND: KAPPA

25.9	73.6	121.3
169.0	216.7	264.4
312.1		

CONTOURS IN UNSCALED CONDUCTIVITY UNITS

TOP OF PAGE IS EAST

Plot 30

CONDUCTIVITY CONTOURS OF ELECTROSCAN DATA
PORTAGE, LARGE GRID, FOUR LEVELS

PHI-KAPPA ITERATIONS PERFORMED=200   DEPTH UNIT=2

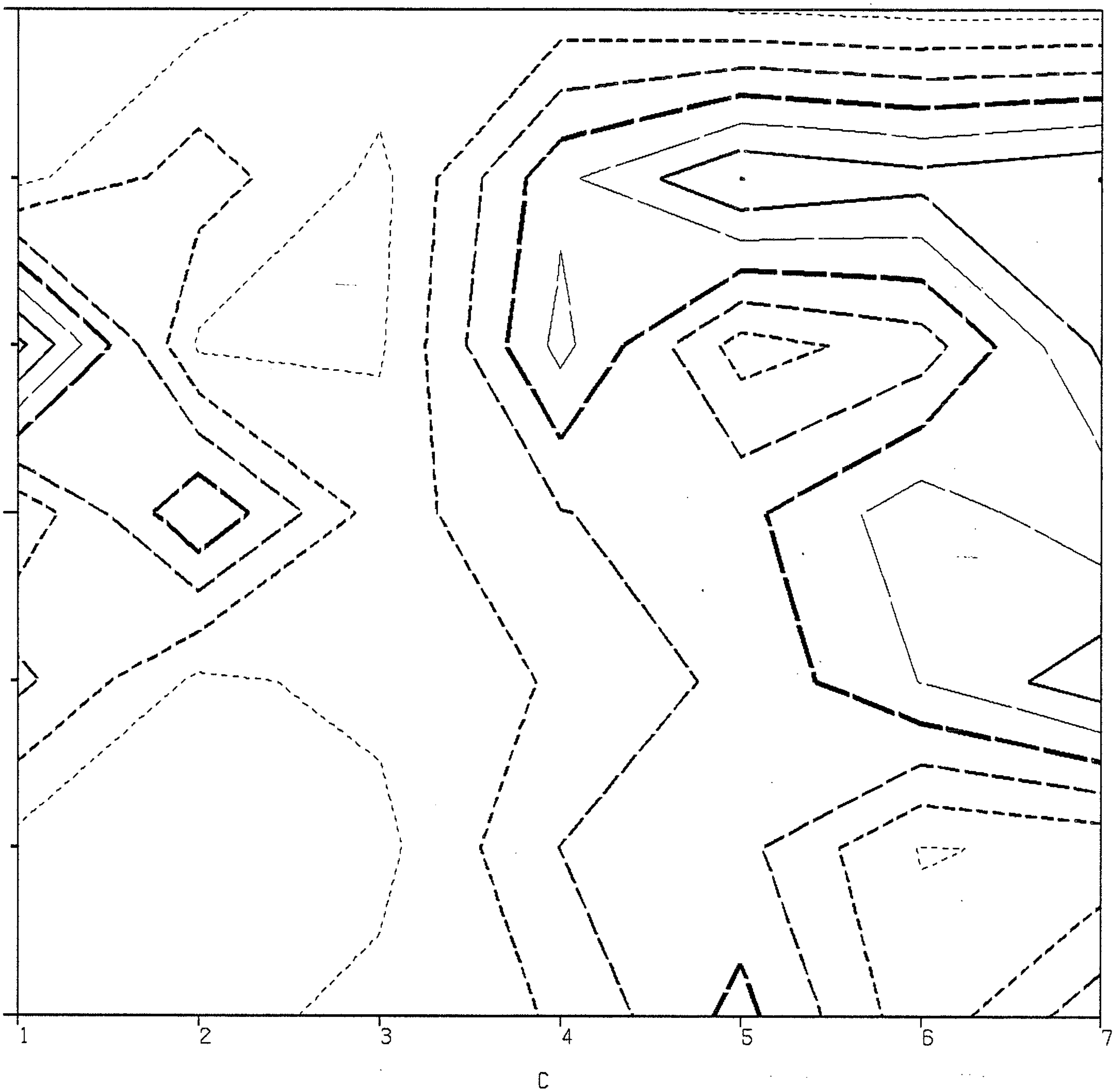

LEGEND: KAPPA 4779.1 18954.4 33129.7 47305.0 61480.3 75655.6 89830.9

CONTOURS IN UNSCALED CONDUCTIVITY UNITS

TOP OF PAGE IS EAST

Plot 31

CONDUCTIVITY CONTOURS OF ELECTROSCAN DATA
PORTAGE, LARGE GRID, FOUR LEVELS

PHI-KAPPA ITERATIONS PERFORMED=200   DEPTH UNIT=3

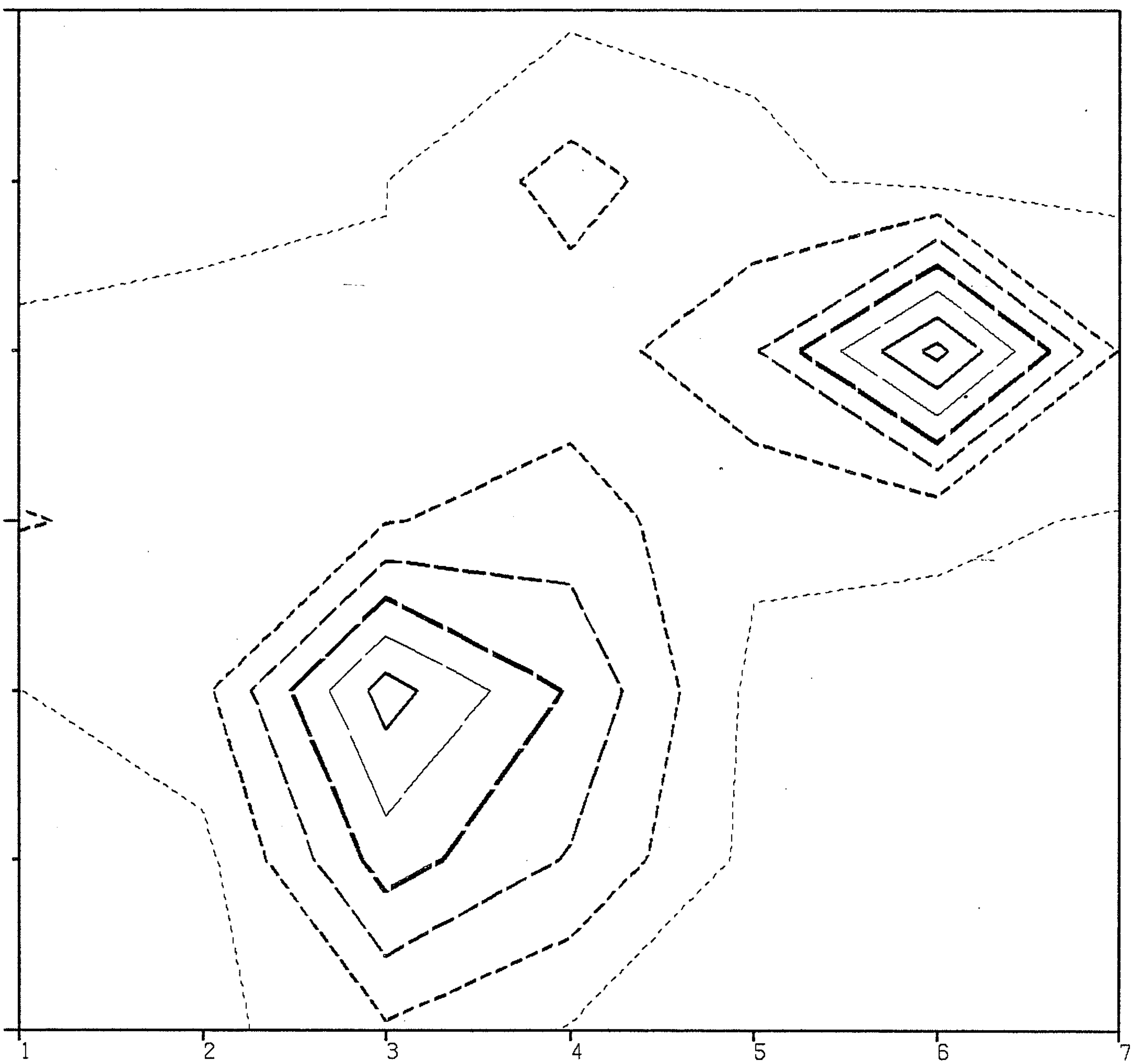

LEGEND: KAPPA

4152.85	16431.40	28709.95
40988.50	53267.05	65545.60
77824.15		

CONTOURS IN UNSCALED CONDUCTIVITY UNITS

TOP OF PAGE IS EAST

Plot 32

CONDUCTIVITY CONTOURS OF ELECTROSCAN DATA
PORTAGE, LARGE GRID, FOUR LEVELS

PHI-KAPPA ITERATIONS PERFORMED=200   DEPTH UNIT=4

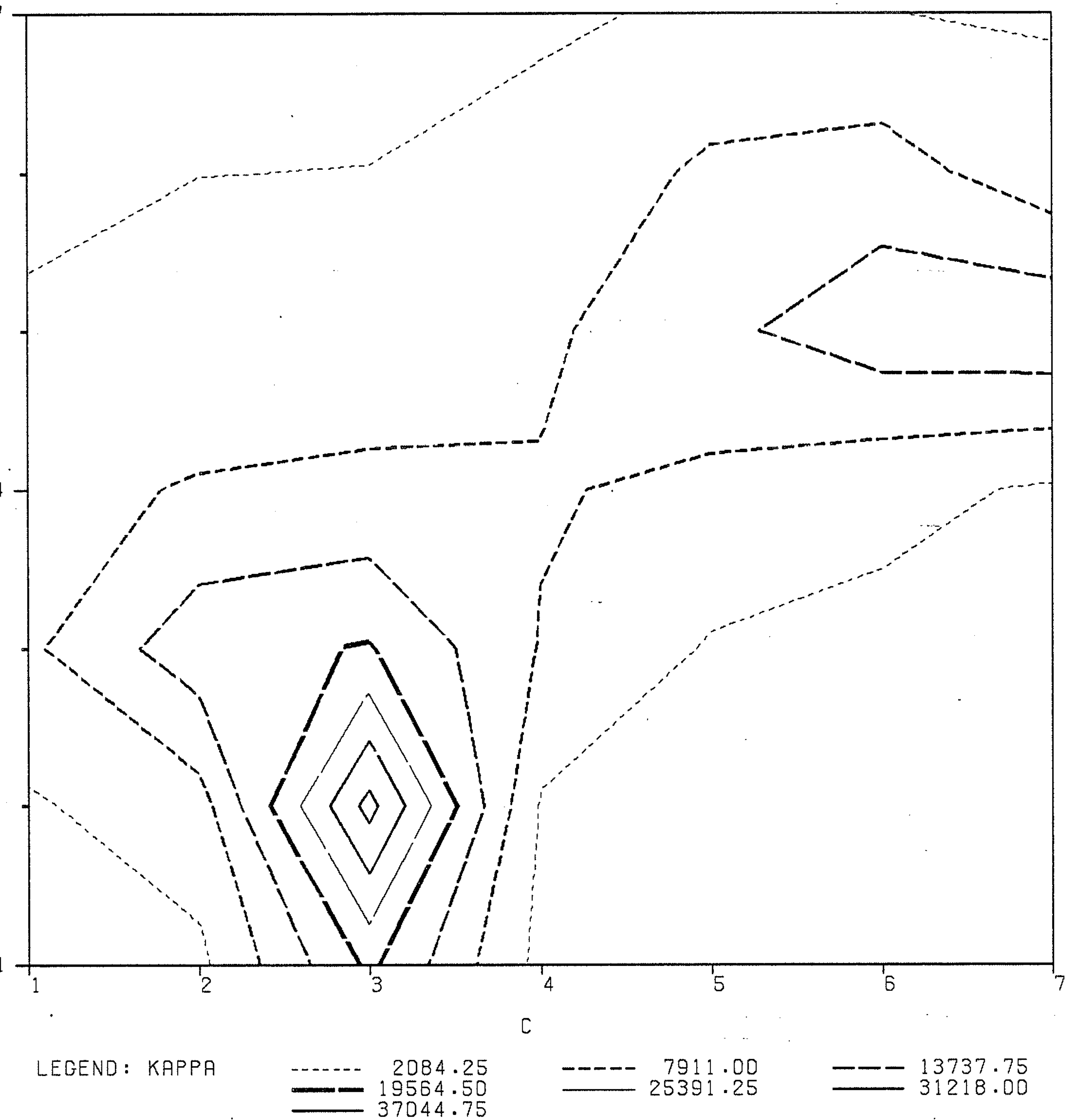

CONTOURS IN UNSCALED CONDUCTIVITY UNITS

TOP OF PAGE IS EAST

Plot 33

CONDUCTIVITY CONTOURS OF ELECTROSCAN DATA
PORTAGE, LARGE GRID, FIVE LEVELS

PHI-KAPPA ITERATIONS PERFORMED=20   DEPTH UNIT=1

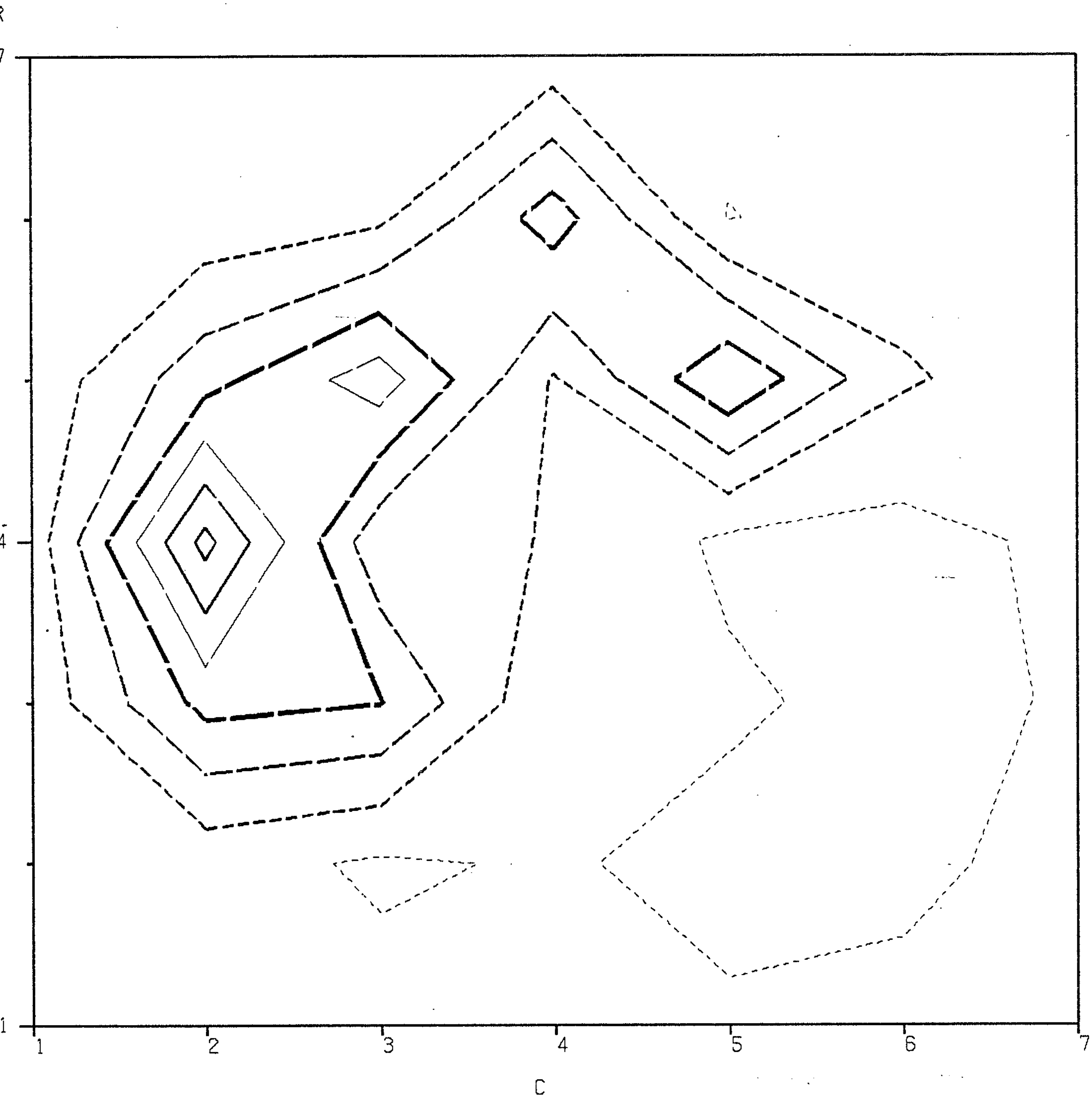

LEGEND: KAPPA   51.05   174.20   297.35   420.50   543.65   666.80   789.95

CONTOURS IN UNSCALED CONDUCTIVITY UNITS

TOP OF PAGE IS EAST

Plot 34

CONDUCTIVITY CONTOURS OF ELECTROSCAN DATA
PORTAGE, LARGE GRID, FIVE LEVELS

PHI-KAPPA ITERATIONS PERFORMED=20   DEPTH UNIT=2

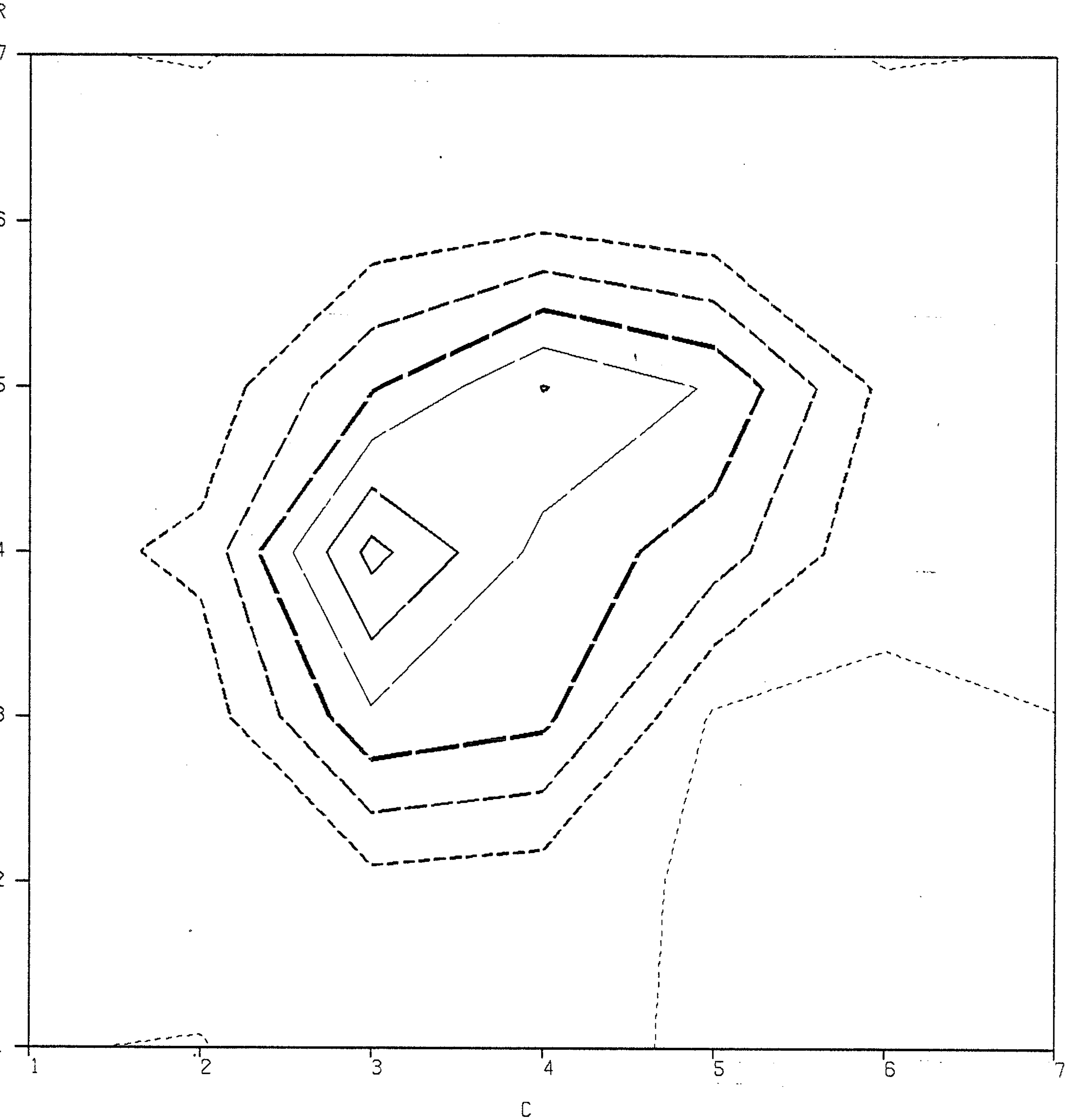

LEGEND: KAPPA ------- 287 ----- 785 — — — 1283 ━━ ━━ 1781 ——— 2279 ——— 2777 ——— 3275

CONTOURS IN UNSCALED CONDUCTIVITY UNITS

TOP OF PAGE IS EAST

Plot 35

CONDUCTIVITY CONTOURS OF ELECTROSCAN DATA
PORTAGE, LARGE GRID, FIVE LEVELS

PHI-KAPPA ITERATIONS PERFORMED=20 DEPTH UNIT=3

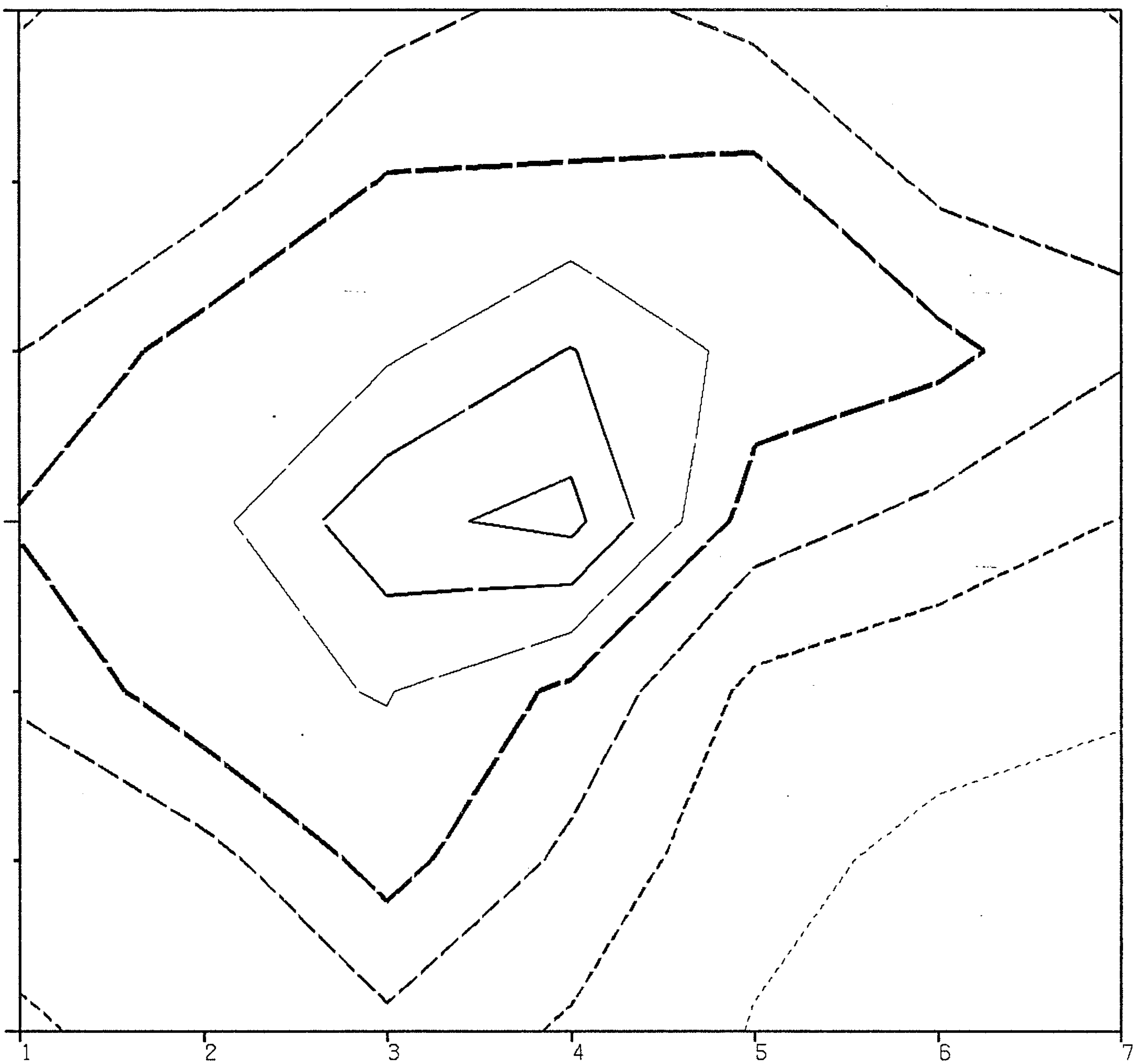

LEGEND: KAPPA

256.1	532.4	808.7
1085.0	1361.3	1637.6
1913.9		

CONTOURS IN UNSCALED CONDUCTIVITY UNITS

TOP OF PAGE IS EAST

Plot 36

CONDUCTIVITY CONTOURS OF ELECTROSCAN DATA
PORTAGE,LARGE GRID, FIVE LEVELS

PHI-KAPPA ITERATIONS PERFORMED=20 DEPTH UNIT=4

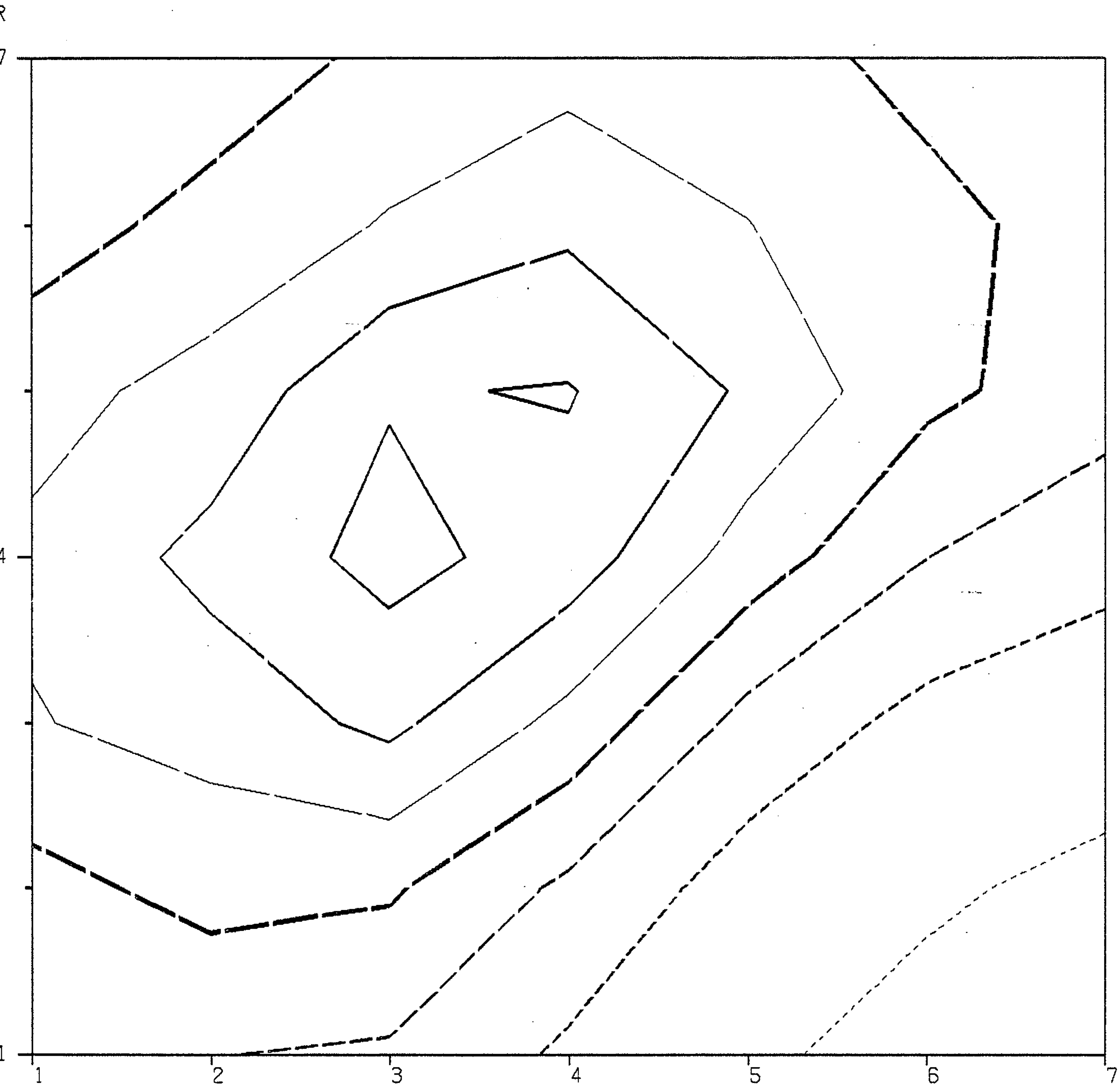

LEGEND: KAPPA

276.65	500.60	724.55
948.50	1172.45	1396.40
1620.35		

CONTOURS IN UNSCALED CONDUCTIVITY UNITS

TOP OF PAGE IS EAST

Plot 37

CONDUCTIVITY CONTOURS OF ELECTROSCAN DATA PORTAGE,LARGE GRID, FIVE LEVELS

PHI-KAPPA ITERATIONS PERFORMED=20 DEPTH UNIT=5

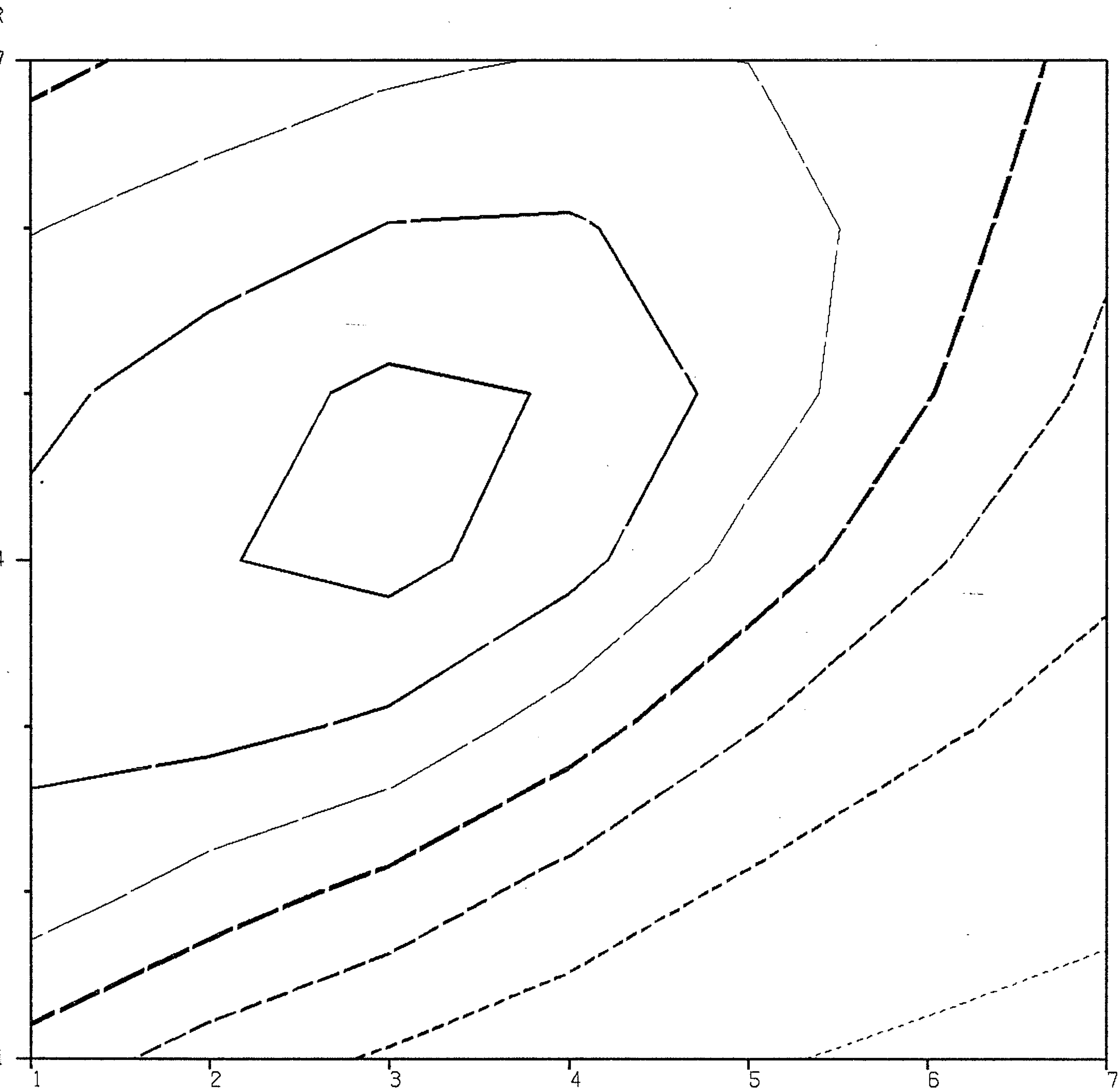

LEGEND: KAPPA 318.65 533.60 748.55 963.50 1178.45 1393.40 1608.35

CONTOURS IN UNSCALED CONDUCTIVITY UNITS

TOP OF PAGE IS EAST

Plot 38

CONDUCTIVITY CONTOURS OF ELECTROSCAN DATA
PORTAGE, LARGE GRID, FIVE LEVELS

PHI-KAPPA ITERATIONS PERFORMED=100   DEPTH UNIT=1

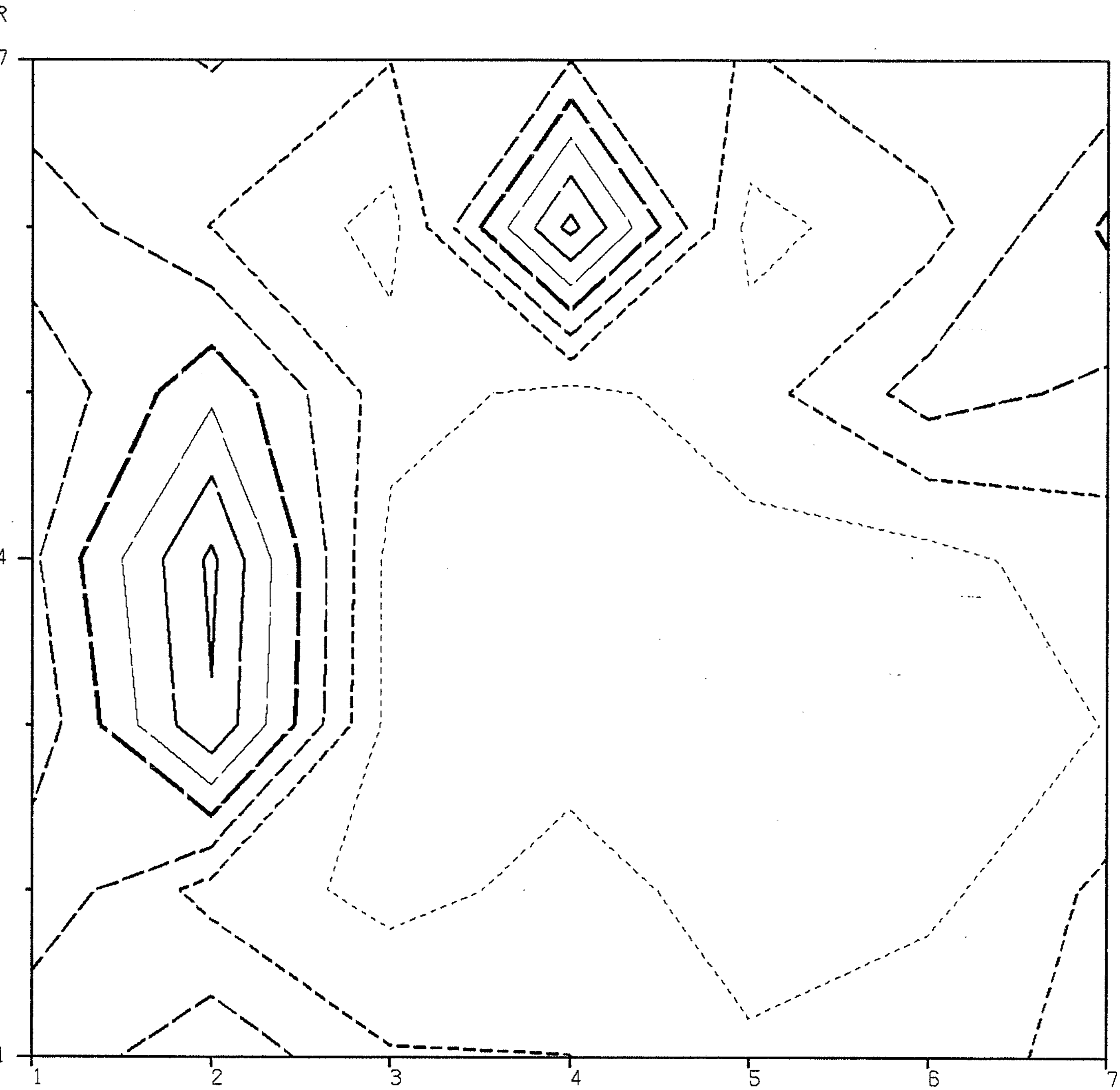

LEGEND: KAPPA

25.35	71.40	117.45
163.50	209.55	255.60
301.65		

CONTOURS IN UNSCALED CONDUCTIVITY UNITS

TOP OF PAGE IS EAST

Plot 39

CONDUCTIVITY CONTOURS OF ELECTROSCAN DATA
PORTAGE,LARGE GRID, FIVE LEVELS

PHI-KAPPA ITERATIONS PERFORMED=100   DEPTH UNIT=2

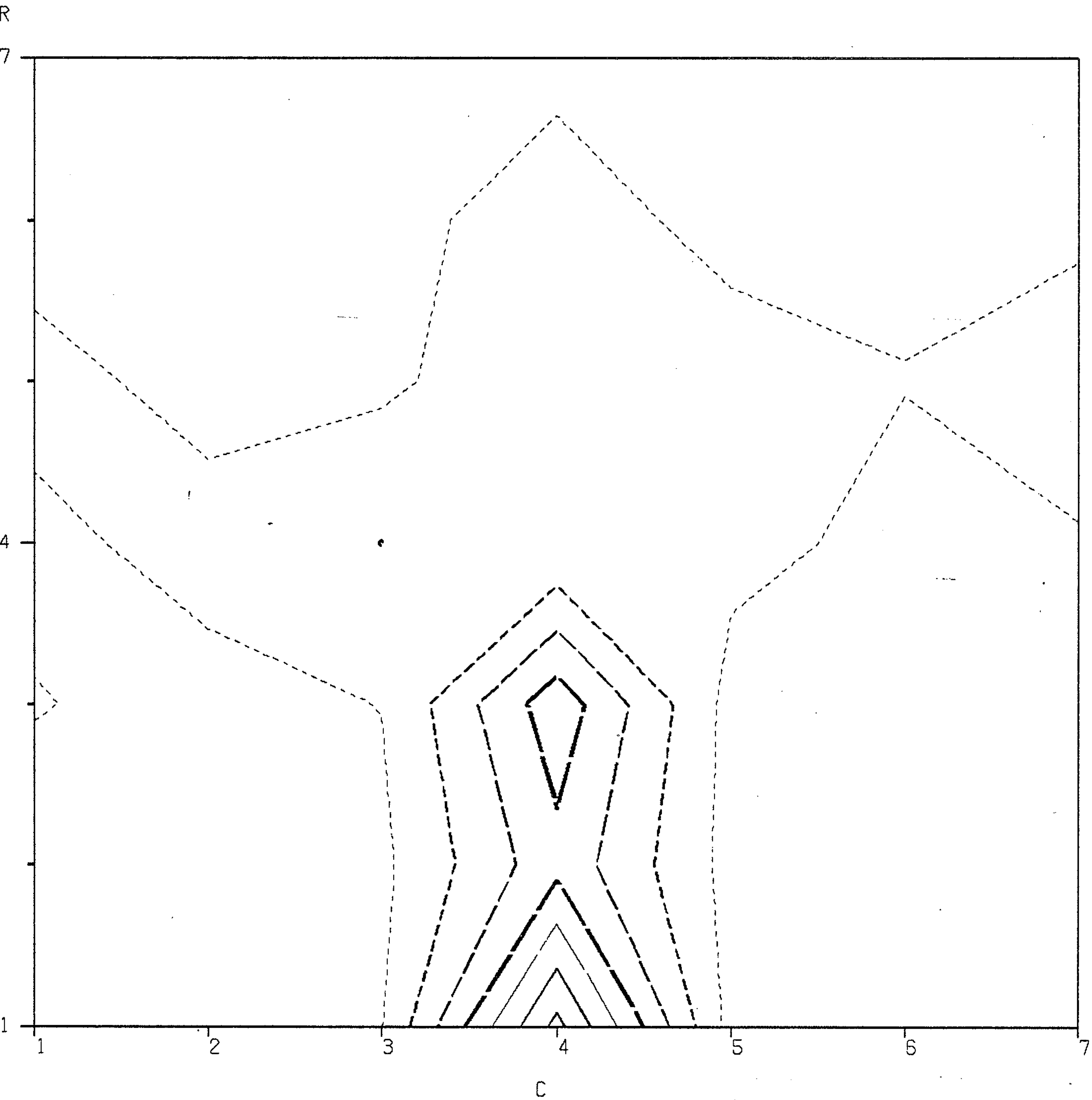

LEGEND: KAPPA

7276.9	29050.6	50824.3
72598.0	94371.7	116145.4
137919.1		

CONTOURS IN UNSCALED CONDUCTIVITY UNITS

TOP OF PAGE IS EAST

Plot 40

CONDUCTIVITY CONTOURS OF ELECTROSCAN DATA
PORTAGE,LARGE GRID, FIVE LEVELS

PHI-KAPPA ITERATIONS PERFORMED=100 DEPTH UNIT=3

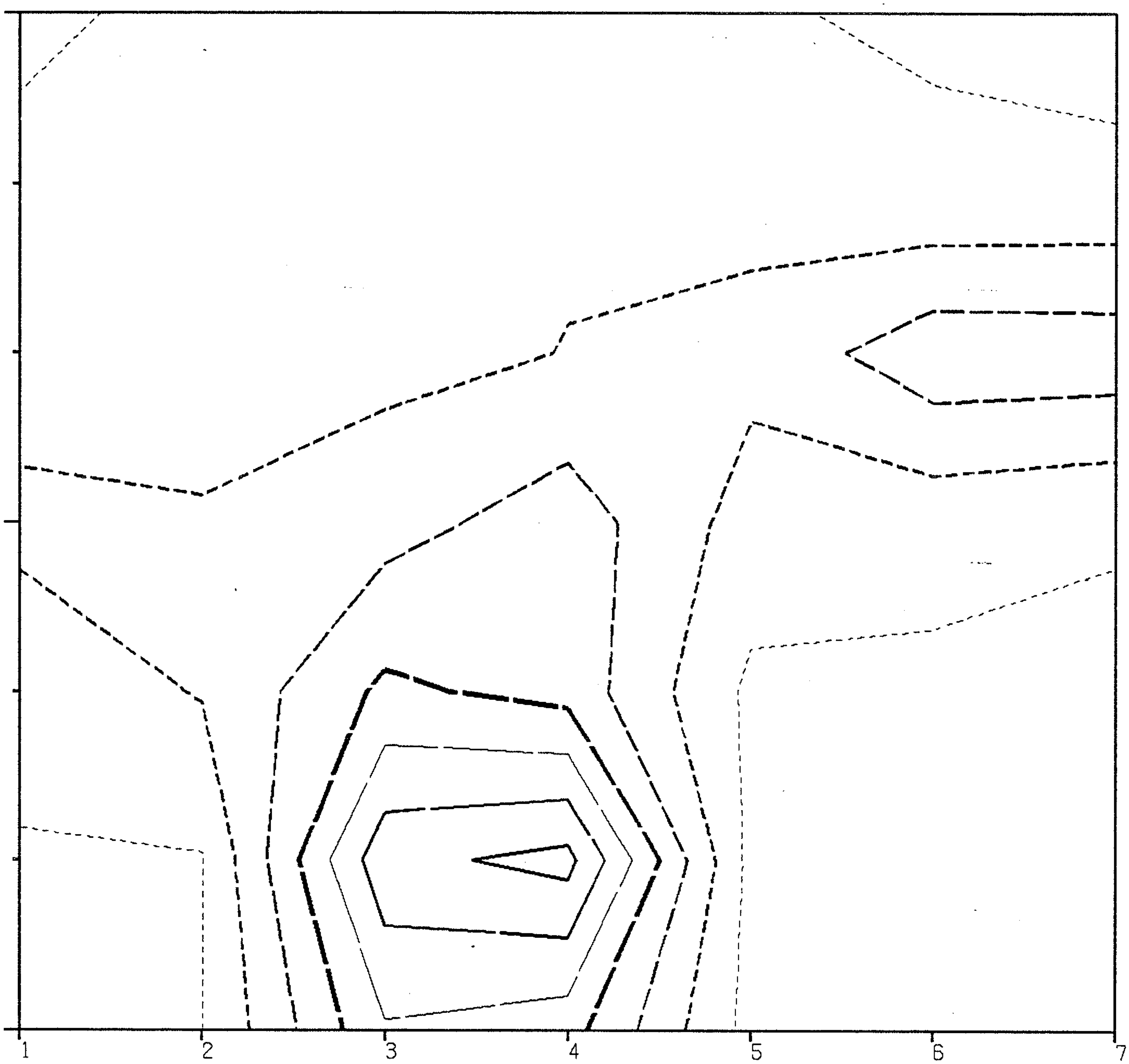

LEGEND: KAPPA

	KAPPA
-------	1368.95
-----	5151.80
— — —	8934.65
heavy dashed	12717.50
thin solid	16500.35
solid	20283.20
heavy solid	24066.05

CONTOURS IN UNSCALED CONDUCTIVITY UNITS

TOP OF PAGE IS EAST

Plot 41

CONDUCTIVITY CONTOURS OF ELECTROSCAN DATA
PORTAGE,LARGE GRID, FIVE LEVELS

PHI-KAPPA ITERATIONS PERFORMED=100 DEPTH UNIT=4

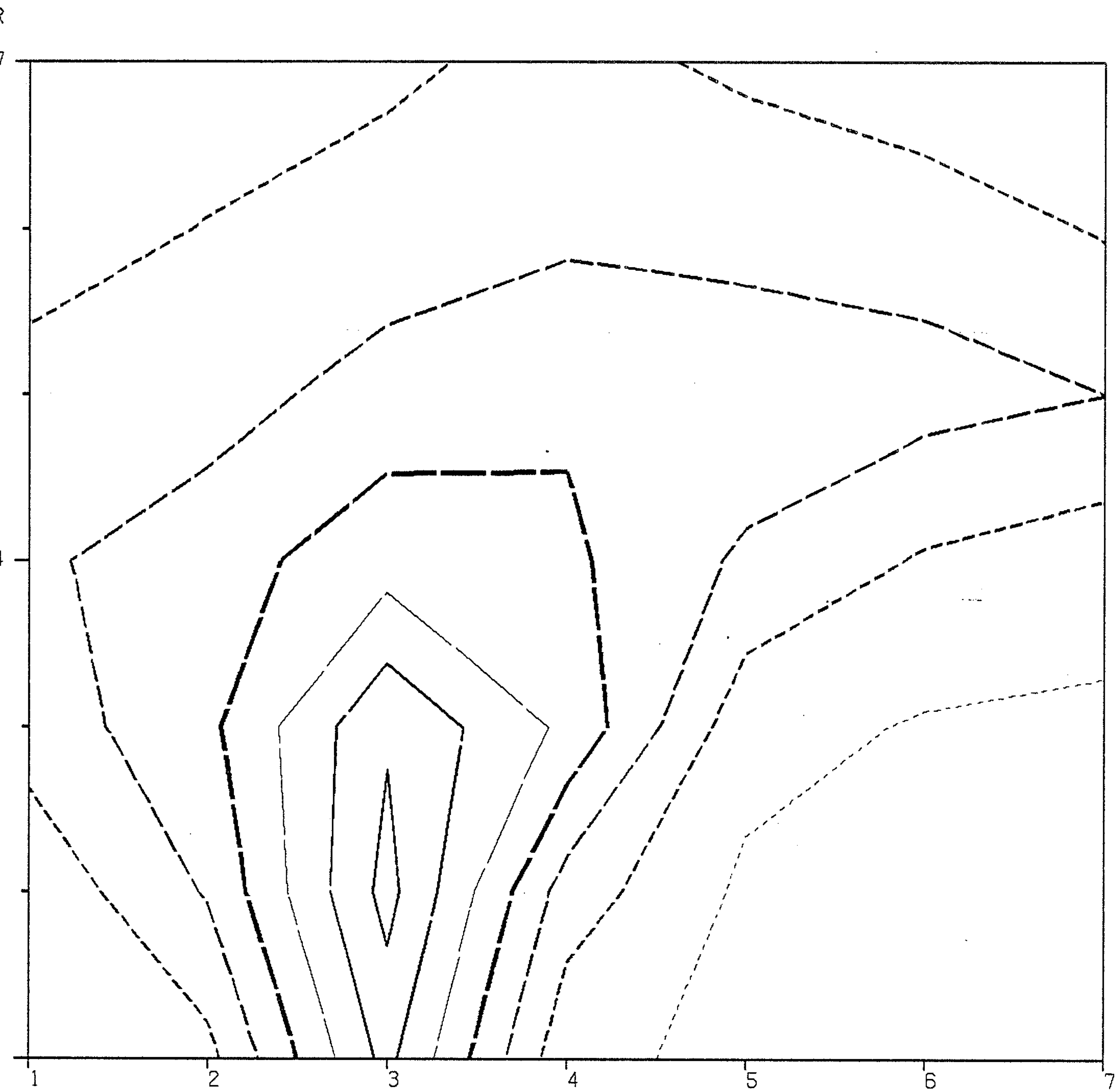

LEGEND: KAPPA

755.65	2539.60	4323.55
6107.50	7891.45	9675.40
11459.35		

CONTOURS IN UNSCALED CONDUCTIVITY UNITS

TOP OF PAGE IS EAST

Plot 42

CONDUCTIVITY CONTOURS OF ELECTROSCAN DATA
PORTAGE,LARGE GRID, FIVE LEVELS

PHI-KAPPA ITERATIONS PERFORMED=100 DEPTH UNIT=5

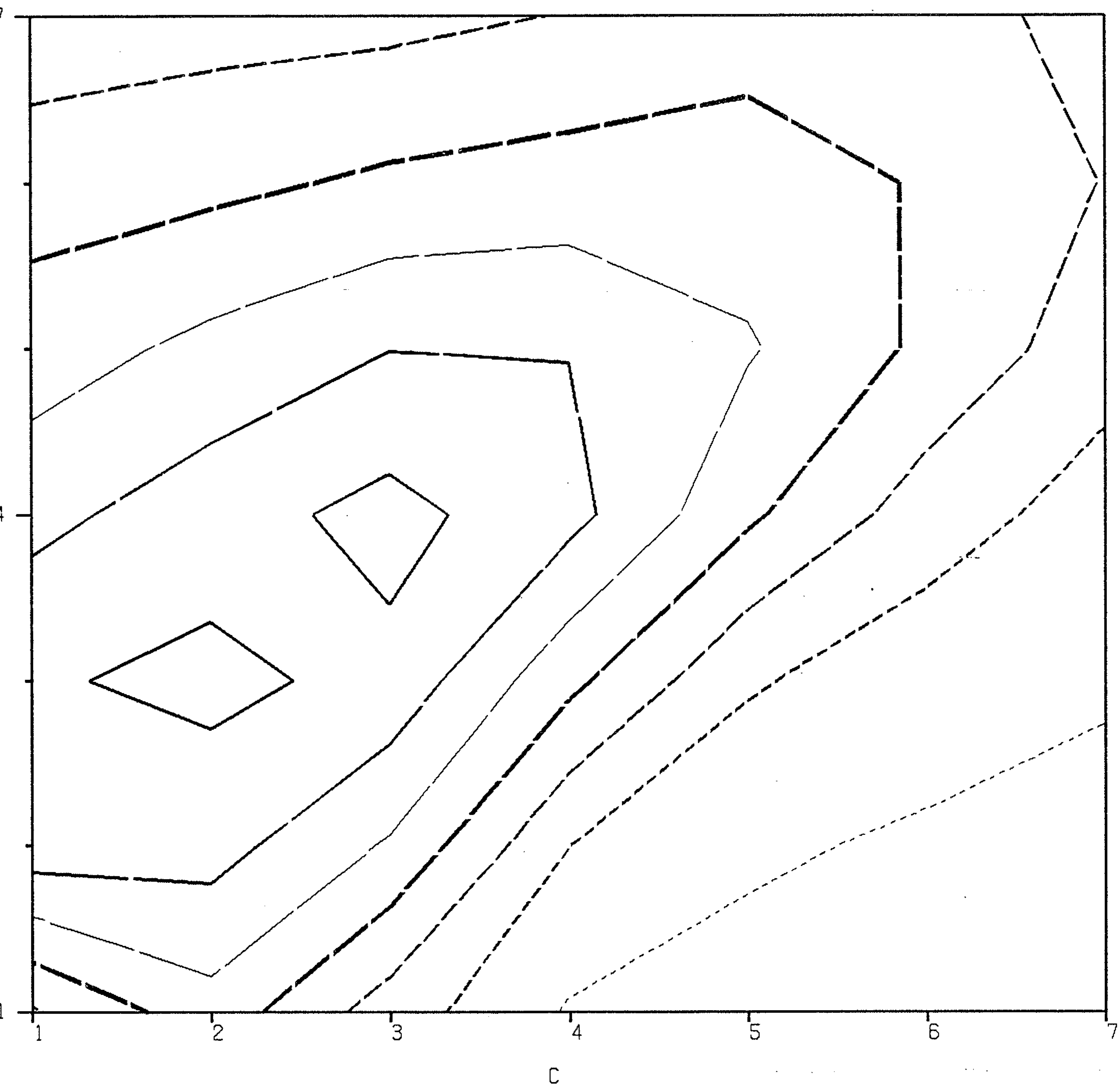

LEGEND: KAPPA

------- 576.45
----- 1666.80
— — — 2757.15
— — 3847.50
——— 4937.85
——— 6028.20
——— 7118.55

CONTOURS IN UNSCALED CONDUCTIVITY UNITS

TOP OF PAGE IS EAST

Plot 43

CONDUCTIVITY CONTOURS OF ELECTROSCAN DATA
PORTAGE,LARGE GRID, FIVE LEVELS

PHI-KAPPA ITERATIONS PERFORMED=200 DEPTH UNIT=1

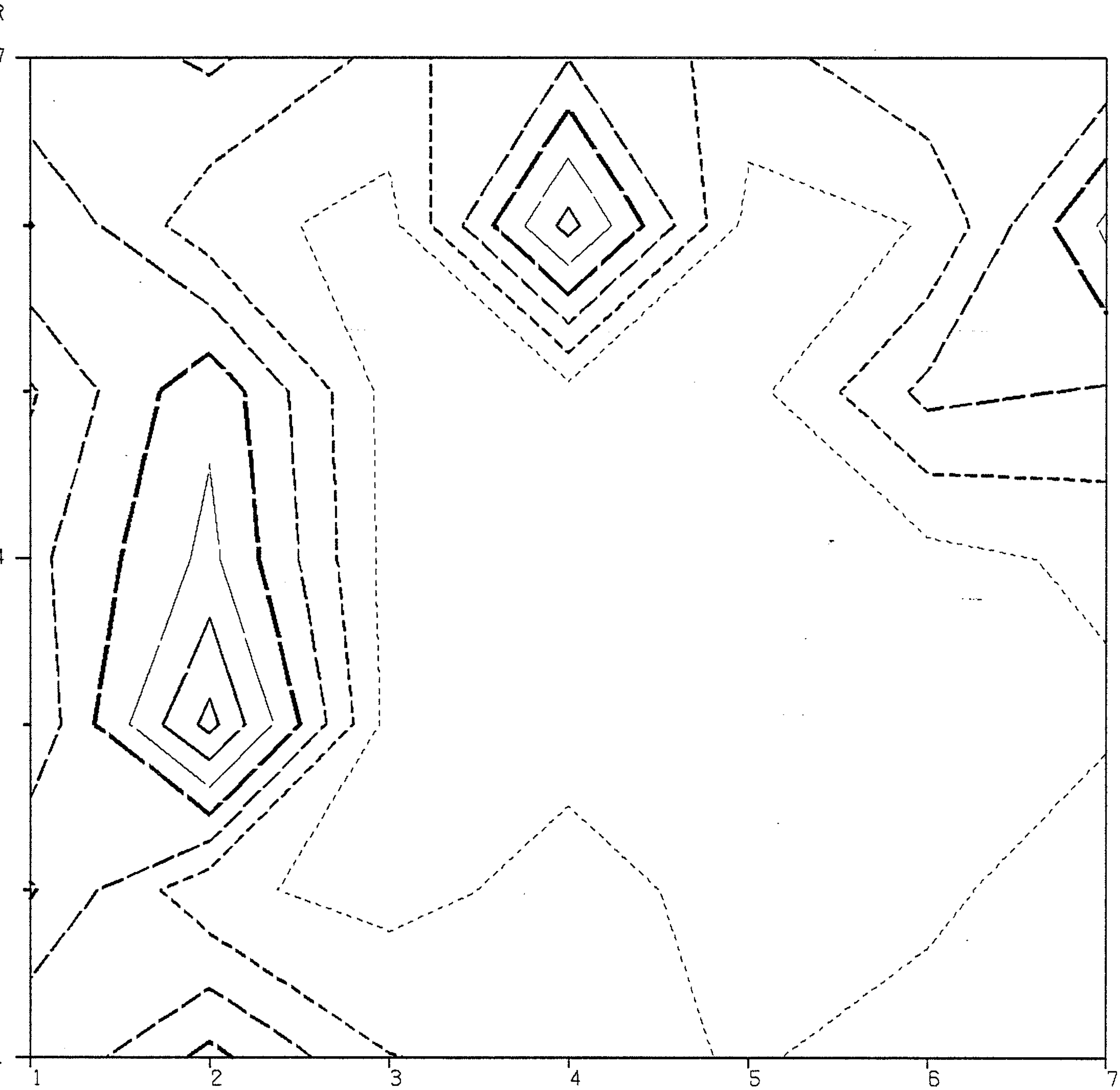

LEGEND: KAPPA 26.3 75.2 124.1 173.0 221.9 270.8 319.7

CONTOURS IN UNSCALED CONDUCTIVITY UNITS

TOP OF PAGE IS EAST

Plot 44

CONDUCTIVITY CONTOURS OF ELECTROSCAN DATA
PORTAGE, LARGE GRID, FIVE LEVELS

PHI-KAPPA ITERATIONS PERFORMED=200   DEPTH UNIT=2

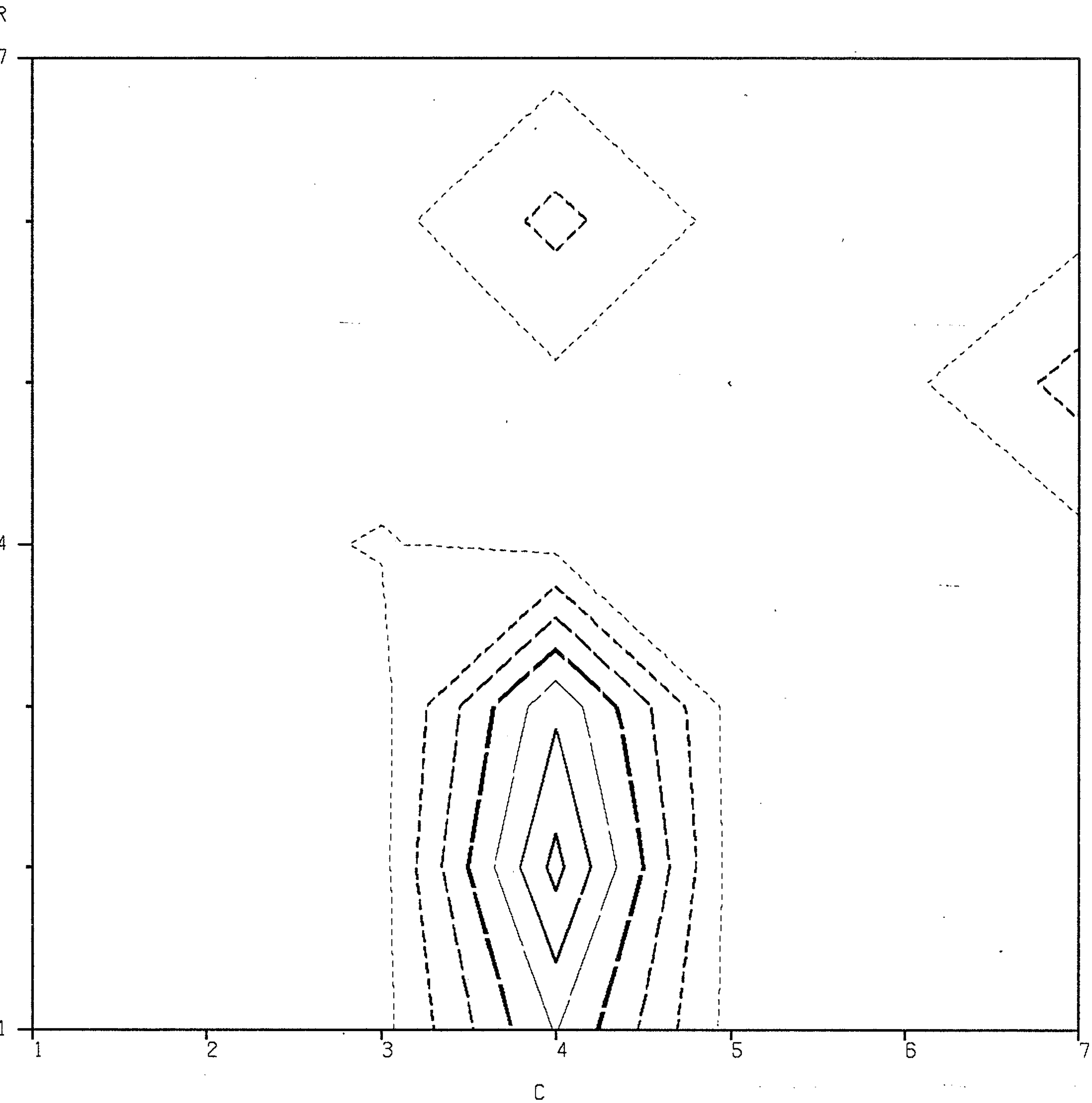

LEGEND: KAPPA

161695.8	646753.2	1131810.6
1616868.0	2101925.4	2586982.8
3072040.2		

CONTOURS IN UNSCALED CONDUCTIVITY UNITS

TOP OF PAGE IS EAST

Plot 45

CONDUCTIVITY CONTOURS OF ELECTROSCAN DATA
PORTAGE,LARGE GRID, FIVE LEVELS

PHI-KAPPA ITERATIONS PERFORMED=200 DEPTH UNIT=3

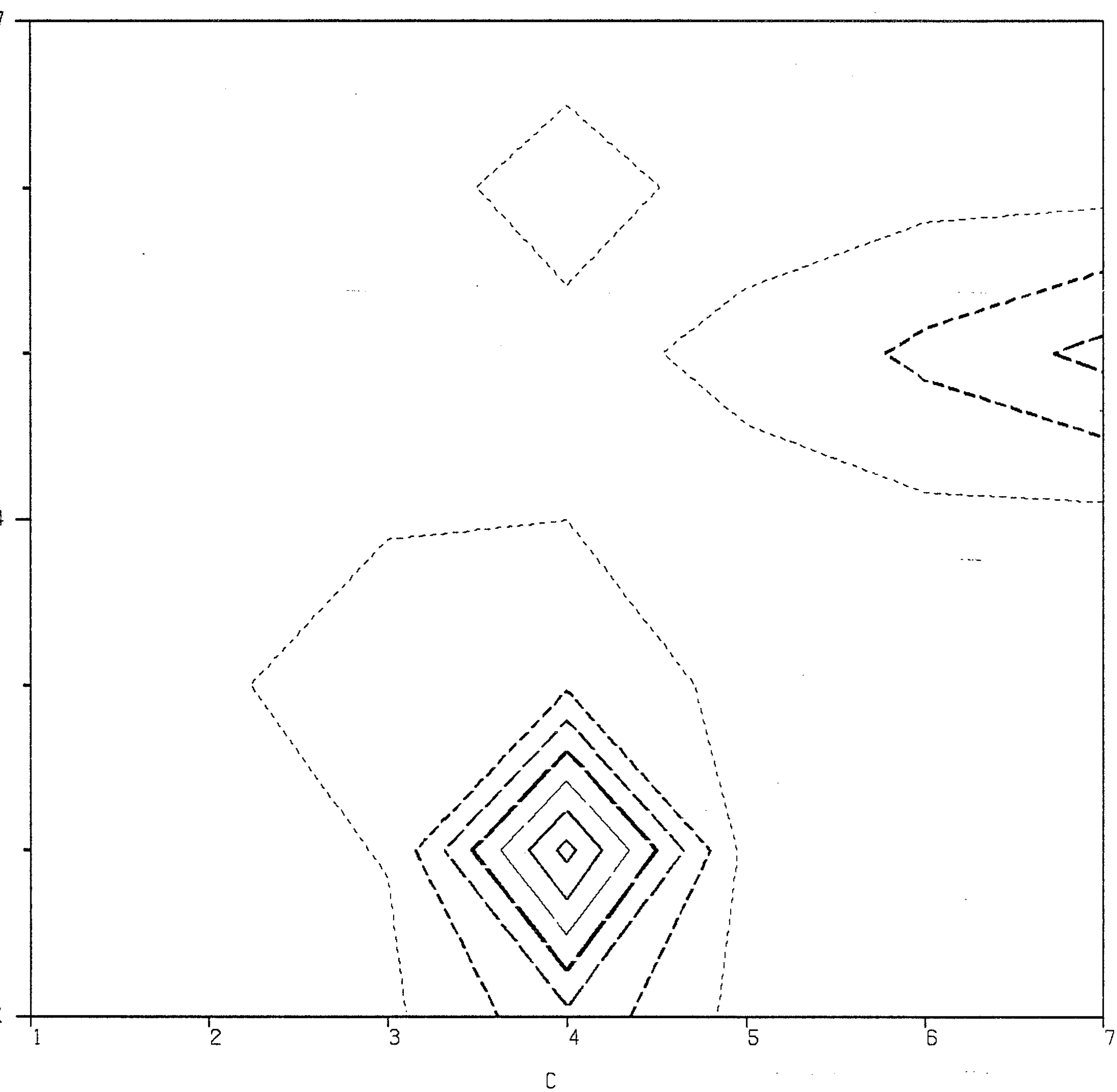

LEGEND: KAPPA

-------	20749.45
– – – –	82808.80
— — —	144868.15
▬ ▬	206927.50
———	268986.85
———	331046.20
———	393105.55

CONTOURS IN UNSCALED CONDUCTIVITY UNITS

TOP OF PAGE IS EAST

Plot 46

CONDUCTIVITY CONTOURS OF ELECTROSCAN DATA
PORTAGE, LARGE GRID, FIVE LEVELS

PHI-KAPPA ITERATIONS PERFORMED=200 DEPTH UNIT=4

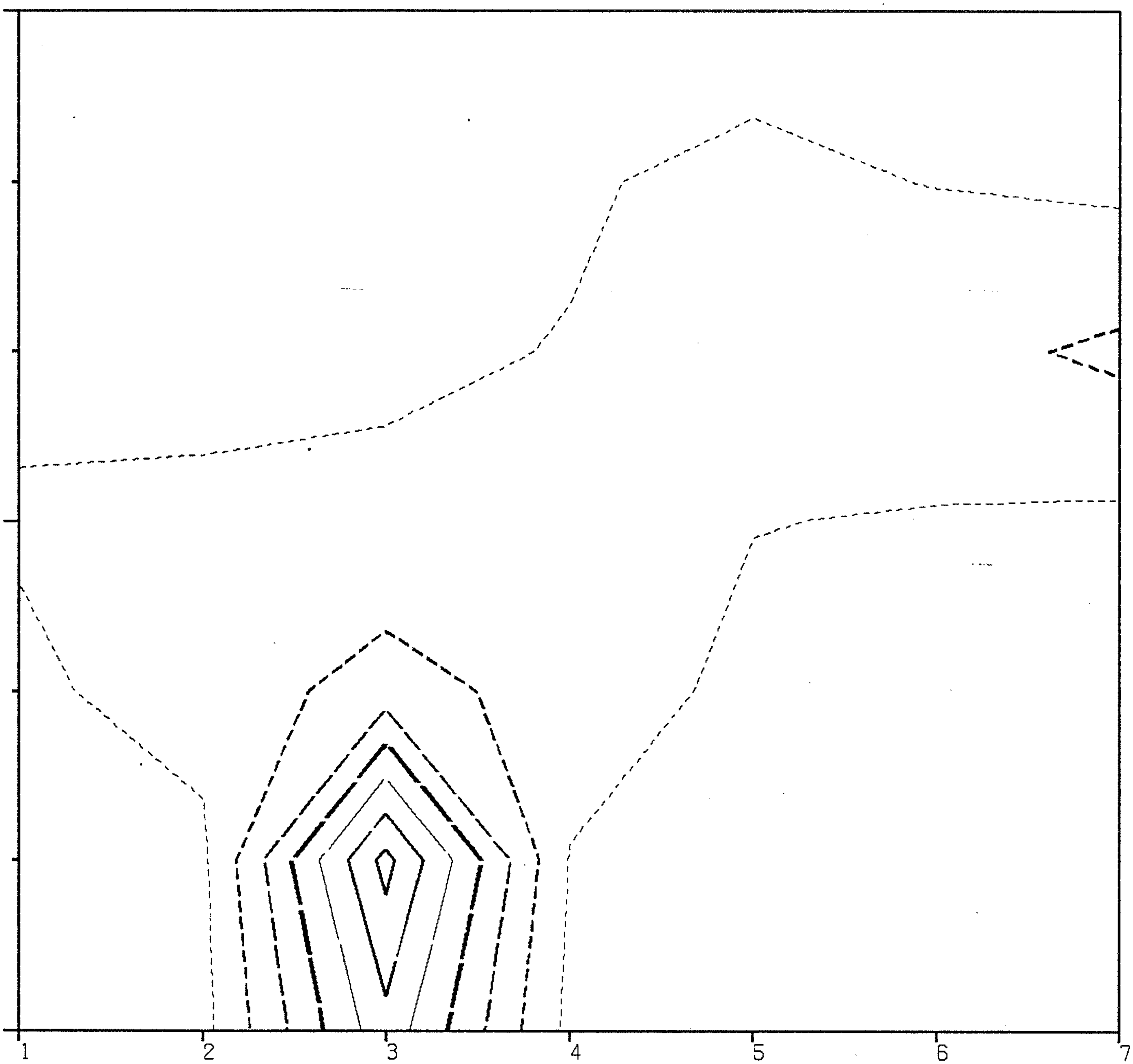

LEGEND: KAPPA

-------	6504.45
-----	25597.80
— — —	44691.15
━━ ━━	63784.50
———	82877.85
———	101971.20
———	121064.55

CONTOURS IN UNSCALED CONDUCTIVITY UNITS

TOP OF PAGE IS EAST

Plot 47

CONDUCTIVITY CONTOURS OF ELECTROSCAN DATA
PORTAGE,LARGE GRID, FIVE LEVELS

PHI-KAPPA ITERATIONS PERFORMED=200 DEPTH UNIT=5

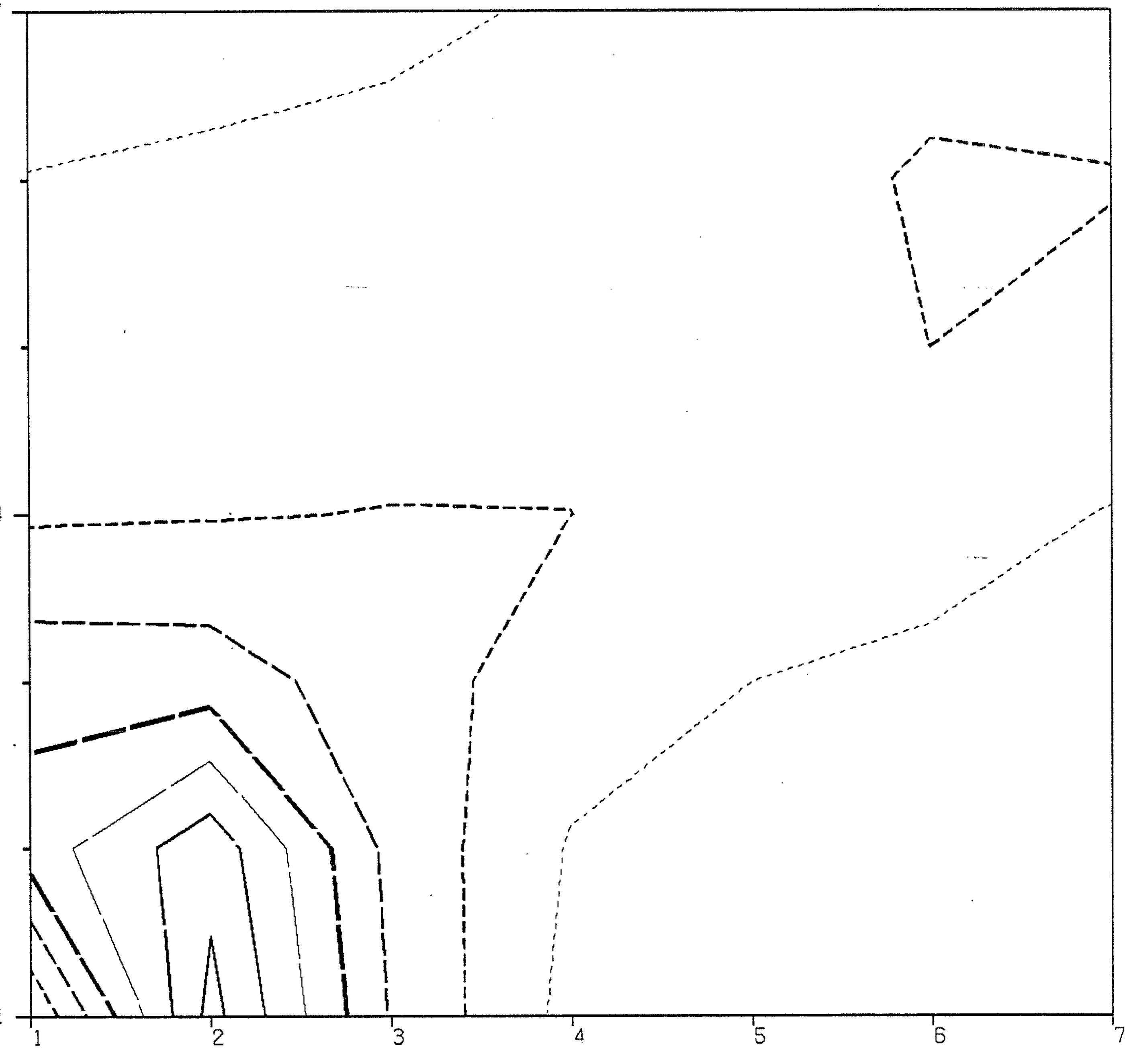

LEGEND: KAPPA

- 2094.7
- 7823.8
- 13552.9
- 19282.0
- 25011.1
- 30740.2
- 36469.3

CONTOURS IN UNSCALED CONDUCTIVITY UNITS

TOP OF PAGE IS EAST

APPENDIX A

SAMPLE HOLE LOGS

APPENDIX A

SAMPLE HOLE LOGS

SAMPLE HOLE 1

DEPTH	SOIL DESCRIPTION
0 - 20 cm	Silty organic topsoil, black swampy peat.
20 - 100 cm	Grey mottled clayey silt, even distribution of rust stains in 1 - 3 cm spots, soft, some fine sand.
100 - 110 cm	Thinly bedded grey clay, medium consistency, medium to high plasticity.
110 - 365 cm	Medium to coarse grained sand, light yellow brown in upper part, grey in lower part. Saturated to above grey sand.

CONDUCTIVITY SAMPLES

CONDUCTIVITY	TEMPERATURE	CORRECTION @ 25 C	CONDUCTIVITY (micromhos)
990	6.0	1.530	1515
1000	4.5	1.600	1600
1000	4.0	1.610	1610
		AVERAGE:	1575

SAMPLE HOLE 2

DEPTH	SOIL DESCRIPTION
0 - 20 cm	Silty organic topsoil, black swampy peat
20 - 105 cm	Grey mottled clayey silt, rust spots as before
105 - 110 cm	Thinly bedded grey clay, medium consistency, medium to high plasticity
110 - 300 cm	Medium to coarse grained sand. Light yellow brown in upper part, grey in lower part. Saturated to above grey sand.

CONDUCTIVITY SAMPLES

CONDUCTIVITY	TEMPERATURE	CORRECTION @25 C	CONDUCTIVITY (micromhos)
1090	5	1.570	1711
1090	5	1.570	1711
1090	4.5	1.600	1744
		AVERAGE:	1722

SAMPLE HOLE 3

DEPTH	SOIL DESCRIPTION
0 - 100 cm	Topsoil and swampy peat with black organic clay.
100 - 170 cm	Dark grey to black organic clayey silt with some brown staining
170 - 220 cm	Grey, medium to coarse sand
220 -	Sand point drive to 360 cm

CONDUCTIVITY SAMPLES

CONDUCTIVITY	TEMPERATURE	CORRECTION @ 25 C	CONDUCTIVITY (micromhos)
1200	5.5	1.555	1866
1150	7.0	1.500	1725
1320	9.0	1.420	1874

AVERAGE: 1821

SAMPLE HOLE 4

DEPTH	SOIL DESCRIPTION
0 - 70 cm	Organic topsoil and swampy peat, silty
70 - 140 cm	Grey mottled clayey silt, rust spots (as before)
140 - 145 cm	Thinly bedded grey clay, medium consistency, medium to high plasticity
145 - 175 cm	Light yellow brown sand, medium to coarse grain size
175 - 300 cm	Grey, medium to coarse sand

CONDUCTIVITY SAMPLES

CONDUCTIVITY	TEMPERATURE	CORRECTION @ 25 C	CONDUCTIVITY (micromhos)
790	9.0	1.420	1122
790	7.0	1.500	1105
790	7.0	1.500	1170
		AVERAGE:	1159

SAMPLE HOLE 5

DEPTH	SOIL DESCRIPTION
0 - 20 cm	Organic black topsoil
20 - 110 cm	Grey mottled clayey silt, rust stains (as before)
110 - 140 cm	Thinly bedded grey clay, plastic, soft to medium consistency
140 - 170 cm	Light brown yellow sand, medium to coarse grained
170 - 300 cm	Dark grey sand, medium to coarse grained

CONDUCTIVITY SAMPLES

CONDUCTIVITY	TEMPERATURE	CORRECTION @ 25 C	CONDUCTIVITY (micromhos)
600	7.0	1.500	900
620	11.5	1.335	828
680	15.5	1.217	828
		AVERAGE:	850

SAMPLE HOLE 6

DEPTH	SOIL DESCRIPTION
0 - 30 cm	Organic black topsoil and swampy peat
30 - 120 cm	Grey mottled clayey silt, rust stains (as before)
120 - 130 cm	Thinly bedded grey clay, plastic, soft to medium consistency
130 - 160 cm	Light yellow brown sand, medium to coarse grained
160 - 260 cm	Grey, medium to coarse sand

CONDUCTIVITY SAMPLES

CONDUCTIVITY	TEMPERATURE	CORRECTION* @ 25 C	CONDUCTIVITY (micromhos)
620 **	3.0	1.650	1023
590 **	3.0	1.650	974
620	7.0	1.500	930
610	6.0	1.530	933
		AVERAGE:	965

** Sampled in bottom of excavation directly

SAMPLE HOLE 7

DEPTH	SOIL DESCRIPTION
0 - 20 cm	Organic topsoil, black swampy peat
20 - 100 cm	Grey mottled clayey silt, rust stained (as before)
100 - 115 cm	Thinly bedded grey clay, plastic, soft to medium consistency
115 - 145 cm	Light yellow brown sand, medium grained
145 - 320 cm	Grey, medium to coarse sand

CONDUCTIVITY SAMPLES

CONDUCTIVITY	TEMPERATURE	CORRECTION @ 25 C	CONDUCTIVITY (micromhos)
760	5	1.570	1193
750	5	1.570	1178
780	6	1.530	1193
		AVERAGE:	1188

SAMPLE HOLE 8

DEPTH	SOIL DESCRIPTION
0 - 20 cm	Organic topsoil, black silty loam
20 - 50 cm	Brown sandy silt
50 - 250 cm	Light yellow brown sand, fining upward from medium sand at the bottom to fine and very fine sand at the top
250 -	Grey, medium to coarse sand

CONDUCTIVITY SAMPLES

CONDUCTIVITY	TEMPERATURE	CORRECTION @ 25 C	CONDUCTIVITY (micromhos)
890	5	1.570	1397
910	3	1.650	1502
900	3	1.650	1485
		AVERAGE:	1461

APPENDIX B

ELECTROSCAN FIELD DATA

POTENTIAL MEASUREMENTS FOR SMALL GRID
OCTOBER 14,1984

	PATTERN =1			PATTERN =2		
ELECTRODE LOCATION	CURRENT INPUT	CURRENT OUTPUT	NORMALIZED POTENTIAL (2 PI V/I)	CURRENT INPUT	CURRENT OUTPUT	NORMALIZED POTENTIAL (2 PI V/I)
2	1	57	21.9700	8	64	0.4190
7	1	57	0.6200	8	64	24.6300
11	1	57	4.9670	8	64	0.7470
12	1	57	2.4850	8	64	1.4550
13	1	57	1.3090	8	64	3.1180
14	1	57	0.7610	8	64	6.5030
18	1	57	4.0890	8	64	0.2530
19	1	57	2.3640	8	64	0.4940
20	1	57	1.3860	8	64	0.9110
21	1	57	0.8120	8	64	1.7840
22	1	57	0.5200	8	64	3.2280
23	1	57	0.3530	8	64	5.2310
26	1	57	1.4130	8	64	0.1390
27	1	57	1.0270	8	64	0.2580
28	1	57	0.6880	8	64	0.4710
29	1	57	0.4380	8	64	0.8020
30	1	57	0.3070	8	64	1.2210
31	1	57	0.2190	8	64	1.7330
34	1	57	-0.2630	8	64	-0.0680
35	1	57	-0.1430	8	64	-0.0430
36	1	57	0.0000	8	64	0.0000
37	1	57	0.0650	8	64	-0.0650
38	1	57	0.0940	8	64	-0.1510
39	1	57	0.0960	8	64	-0.2790
42	1	57	-1.6980	8	64	-0.1980
43	1	57	-1.0830	8	64	-0.2750
44	1	57	-0.6060	8	64	-0.4200
45	1	57	-0.3260	8	64	-0.7330
46	1	57	-0.1760	8	64	-1.2990
47	1	57	-0.0910	8	64	-2.0950
51	1	57	-1.9040	8	64	-0.4140
52	1	57	-1.0350	8	64	-0.6730
53	1	57	-0.5790	8	64	-1.1700
54	1	57	-0.3090	8	64	-2.1370
58	1	57	-5.6740	8	64	-0.3360
63	1	57	-0.2350	8	64	-5.9380

	PATTERN =3			PATTERN =4		
ELECTRODE LOCATION	CURRENT INPUT	CURRENT OUTPUT	NORMALIZED POTENTIAL (2 PI V/I)	CURRENT INPUT	CURRENT OUTPUT	NORMALIZED POTENTIAL (2 PI V/I)
2	10	15	16.680	50	55	-0.4740
7	10	15	-22.560	50	55	-1.0280
11	10	15	15.540	50	55	-0.4150
12	10	15	2.822	50	55	-0.6150
13	10	15	-4.959	50	55	-0.8800
14	10	15	-17.770	50	55	-1.1050
18	10	15	16.410	50	55	0.2350
19	10	15	7.964	50	55	-0.1700
20	10	15	1.757	50	55	-0.5520
21	10	15	-3.363	50	55	-0.9820
22	10	15	-9.338	50	55	-1.3570
23	10	15	-15.170	50	55	-1.5910
26	10	15	4.743	50	55	0.7930
27	10	15	3.274	50	55	0.4380
28	10	15	0.786	50	55	-0.4070
29	10	15	-1.890	50	55	-1.1450
30	10	15	-4.020	50	55	-1.7920
31	10	15	-5.264	50	55	-2.2210
34	10	15	1.530	50	55	2.1740
35	10	15	0.980	50	55	1.4410
36	10	15	0.000	50	55	0.0000
37	10	15	-1.181	50	55	-1.6140
38	10	15	-2.043	50	55	-2.9700
39	10	15	-2.480	50	55	-3.7700
42	10	15	0.400	50	55	5.8600
43	10	15	0.152	50	55	3.4690
44	10	15	-0.308	50	55	0.5750
45	10	15	-0.825	50	55	-2.1460
46	10	15	-1.188	50	55	-5.1870
47	10	15	-1.414	50	55	-8.0220
51	10	15	-0.196	50	55	4.9850
52	10	15	-0.395	50	55	0.8870
53	10	15	-0.638	50	55	-2.2210
54	10	15	-0.879	50	55	-6.7400
58	10	15	-0.247	50	55	4.7190
63	10	15	-0.733	50	55	-6.1390

POTENTIAL MEASUREMENTS FOR SMALL GRID
OCTOBER 14, 1984

	PATTERN =5			PATTERN =6		
ELECTRODE LOCATION	CURRENT INPUT	CURRENT OUTPUT	NORMALIZED POTENTIAL (2 PI V/I)	CURRENT INPUT	CURRENT OUTPUT	NORMALIZED POTENTIAL (2 PI V/I)
2	9	56	11.1100	16	49	0.3690
7	9	56	-0.2850	16	49	15.5600
11	9	56	5.5050	16	49	0.6550
12	9	56	2.1660	16	49	1.5060
13	9	56	0.6500	16	49	3.3650
14	9	56	-0.1560	16	49	7.3070
18	9	56	8.9920	16	49	-0.1460
19	9	56	3.7590	16	49	0.3120
20	9	56	1.5160	16	49	1.0940
21	9	56	0.2620	16	49	2.5360
22	9	56	-0.5210	16	49	5.0800
23	9	56	-1.0260	16	49	10.5600
26	9	56	3.8210	16	49	-0.7460
27	9	56	2.1450	16	49	-0.1440
28	9	56	0.8210	16	49	0.5910
29	9	56	-0.2600	16	49	1.5820
30	9	56	-1.0310	16	49	2.8540
31	9	56	-1.7000	16	49	4.5670
34	9	56	1.4450	16	49	-1.8870
35	9	56	0.7600	16	49	-0.8840
36	9	56	0.0000	16	49	0.0000
37	9	56	-0.9310	16	49	0.8480
38	9	56	-1.9120	16	49	1.5630
39	9	56	-3.0270	16	49	2.2390
42	9	56	0.4170	16	49	-3.6670
43	9	56	0.0070	16	49	-1.7220
44	9	56	-0.5810	16	49	-0.5380
45	9	56	-1.4600	16	49	0.2470
46	9	56	-2.8630	16	49	0.7480
47	9	56	-5.3670	16	49	1.1440
51	9	56	-0.3670	16	49	-2.1000
52	9	56	-0.8240	16	49	-0.8180
53	9	56	-1.6320	16	49	-0.1040
54	9	56	-3.2180	16	49	0.3570
58	9	56	-0.2770	16	49	-3.7820
63	9	56	-4.5250	16	49	0.3190

	PATTERN =7			PATTERN =8		
ELECTRODE LOCATION	CURRENT INPUT	CURRENT OUTPUT	NORMALIZED POTENTIAL (2 PI V/I)	CURRENT INPUT	CURRENT OUTPUT	NORMALIZED POTENTIAL (2 PI V/I)
2	4	25	5.8570	40	61	0.5710
7	4	25	4.3740	40	61	1.6860
11	4	25	11.0900	40	61	0.6470
12	4	25	19.8900	40	61	0.8600
13	4	25	12.6400	40	61	1.2490
14	4	25	6.2610	40	61	1.8100
18	4	25	-4.1490	40	61	0.4340
19	4	25	1.8810	40	61	0.5510
20	4	25	4.7770	40	61	0.8210
21	4	25	4.5550	40	61	1.3760
22	4	25	3.1750	40	61	2.2790
23	4	25	1.8480	40	61	3.5780
26	4	25	-8.0720	40	61	0.2980
27	4	25	-1.2770	40	61	0.3650
28	4	25	1.0940	40	61	0.6160
29	4	25	1.6720	40	61	1.2740
30	4	25	1.3950	40	61	2.6080
31	4	25	1.0030	40	61	5.3820
34	4	25	-4.6090	40	61	0.0310
35	4	25	-1.3320	40	61	-0.1340
36	4	25	0.0000	40	61	0.0000
37	4	25	0.5760	40	61	0.7140
38	4	25	0.6170	40	61	0.2590
39	4	25	0.5200	40	61	7.0580
42	4	25	-1.7240	40	61	-0.4000
43	4	25	-0.8130	40	61	-0.8840
44	4	25	-0.0140	40	61	-1.3160
45	4	25	0.1280	40	61	-1.0460
46	4	25	0.2300	40	61	0.6480
47	4	25	0.2940	40	61	3.6900
51	4	25	-0.4590	40	61	-1.7340
52	4	25	-0.1000	40	61	-3.4410
53	4	25	0.0140	40	61	-4.9460
54	4	25	0.0880	40	61	-1.9260
58	4	25	-0.3520	40	61	-0.8450
63	4	25	0.0940	40	61	-0.8080

POTENTIAL MEASUREMENTS FOR SMALL GRID
OCTOBER 14, 1984

	PATTERN =9			PATTERN =10		
ELECTRODE LOCATION	CURRENT INPUT	CURRENT OUTPUT	NORMALIZED POTENTIAL (2 PI V/I)	CURRENT INPUT	CURRENT OUTPUT	NORMALIZED POTENTIAL (2 PI V/I)
2	5	32	2.9280	33	60	0.8150
7	5	32	7.5160	33	60	-0.0700
11	5	32	5.4460	33	60	1.1100
12	5	32	11.3000	33	60	0.6290
13	5	32	18.4600	33	60	0.2600
14	5	32	10.5300	33	60	0.0420
18	5	32	1.1710	33	60	3.0140
19	5	32	2.3960	33	60	1.7240
20	5	32	3.6610	33	60	0.7990
21	5	32	4.1000	33	60	0.2280
22	5	32	1.5790	33	60	-0.0950
23	5	32	-4.2640	33	60	-0.2010
26	5	32	0.4980	33	60	5.3060
27	5	32	0.9130	33	60	2.3260
28	5	32	1.1430	33	60	0.8180
29	5	32	0.5350	33	60	-0.0090
30	5	32	-1.6850	33	60	-0.2950
31	5	32	-7.6630	33	60	-0.3540
34	5	32	0.0630	33	60	7.2770
35	5	32	0.1230	33	60	1.8570
36	5	32	0.0000	33	60	0.0000
37	5	32	-0.7190	33	60	-0.6700
38	5	32	-2.2680	33	60	-0.7060
39	5	32	-5.0780	33	60	-0.6010
42	5	32	-0.1660	33	60	2.9510
43	5	32	-0.2250	33	60	-0.3810
44	5	32	-0.4080	33	60	-1.8340
45	5	32	-0.8960	33	60	-1.8440
46	5	32	-1.6430	33	60	-1.4000
47	5	32	-2.5890	33	60	-0.9410
51	5	32	-0.3800	33	60	-2.9800
52	5	32	-0.5160	33	60	-5.1700
53	5	32	-0.7850	33	60	-3.7790
54	5	32	-1.2140	33	60	-2.0690
58	5	32	-0.3440	33	60	-1.7090
63	5	32	-0.8710	33	60	-1.3860

	PATTERN =11			PATTERN =12		
ELECTRODE LOCATION	CURRENT INPUT	CURRENT OUTPUT	NORMALIZED POTENTIAL (2 PI V/I)	CURRENT INPUT	CURRENT OUTPUT	NORMALIZED POTENTIAL (2 PI V/I)
2	3	59	21.9500	62	6	-1.748
7	3	59	1.9910	62	6	-25.020
11	3	59	21.7600	62	6	-3.177
12	3	59	14.5200	62	6	-6.477
13	3	59	6.2910	62	6	-14.500
14	3	59	2.9900	62	6	-20.750
18	3	59	4.8020	62	6	-0.886
19	3	59	6.1120	62	6	-1.779
20	3	59	5.0740	62	6	-3.153
21	3	59	3.1110	62	6	-5.430
22	3	59	1.8010	62	6	-6.612
23	3	59	0.9920	62	6	-5.254
26	3	59	1.7090	62	6	-0.445
27	3	59	2.1140	62	6	-0.835
28	3	59	1.9730	62	6	-1.381
29	3	59	1.3700	62	6	-1.962
30	3	59	0.8500	62	6	-2.100
31	3	59	0.4940	62	6	-1.740
34	3	59	-0.1400	62	6	0.068
35	3	59	-0.1480	62	6	0.031
36	3	59	0.0000	62	6	0.000
37	3	59	0.0470	62	6	0.141
38	3	59	0.0760	62	6	0.241
39	3	59	0.0750	62	6	0.249
42	3	59	-1.7530	62	6	0.450
43	3	59	-2.1680	62	6	0.748
44	3	59	-1.7440	62	6	1.222
45	3	59	-1.0890	62	6	1.948
46	3	59	-0.6480	62	6	2.462
47	3	59	-0.3630	62	6	2.024
51	3	59	-5.3330	62	6	1.254
52	3	59	-3.7820	62	6	2.226
53	3	59	-2.0930	62	6	4.202
54	3	59	-1.0810	62	6	5.711
58	3	59	-5.5490	62	6	0.841
63	3	59	-0.7600	62	6	5.908

POTENTIAL MEASUREMENTS FOR SMALL GRID
OCTOBER 14,1984

	PATTERN =13			PATTERN =14		
ELECTRODE LOCATION	CURRENT INPUT	CURRENT OUTPUT	NORMALIZED POTENTIAL (2 PI V/I)	CURRENT INPUT	CURRENT OUTPUT	NORMALIZED POTENTIAL (2 PI V/I)
2	17	24	3.591	41	48	0.0810
7	17	24	-5.907	41	48	-1.0260
11	17	24	3.245	41	48	0.1090
12	17	24	0.343	41	48	-0.3150
13	17	24	-1.847	41	48	-0.7860
14	17	24	-4.744	41	48	-1.1460
18	17	24	11.670	41	48	1.1130
19	17	24	3.793	41	48	0.5150
20	17	24	0.526	41	48	-0.1750
21	17	24	-1.815	41	48	-0.8960
22	17	24	-4.926	41	48	-1.5020
23	17	24	-12.260	41	48	-2.1310
26	17	24	7.166	41	48	2.0640
27	17	24	2.961	41	48	0.9650
28	17	24	0.399	41	48	0.0210
29	17	24	-1.495	41	48	-0.9940
30	17	24	-3.716	41	48	-2.0630
31	17	24	-7.588	41	48	-3.1530
34	17	24	2.716	41	48	4.2150
35	17	24	1.253	41	48	1.5130
36	17	24	0.000	41	48	0.0000
37	17	24	-1.211	41	48	-1.2430
38	17	24	-2.511	41	48	-2.8850
39	17	24	-3.964	41	48	-5.3180
42	17	24	0.875	41	48	5.3660
43	17	24	0.373	41	48	1.7860
44	17	24	-0.221	41	48	0.0570
45	17	24	-0.931	41	48	-1.3950
46	17	24	-1.574	41	48	-3.3210
47	17	24	-2.163	41	48	-7.3160
51	17	24	-0.067	41	48	1.2340
52	17	24	-0.357	41	48	-0.0840
53	17	24	-0.745	41	48	-1.2430
54	17	24	-1.146	41	48	-2.9360
58	17	24	-0.073	41	48	1.8460
63	17	24	-0.934	41	48	-2.9730

POTENTIAL MEASUREMENTS FOR LARGE GRID
OCTOBER 13,1984

	PATTERN =1			PATTERN =2		
ELECTRODE LOCATION	CURRENT INPUT	CURRENT OUTPUT	NORMALIZED VOLTAGE (2 PI V/I)	CURRENT INPUT	CURRENT OUTPUT	NORMALIZED VOLTAGE (2 PI V/I)
2	1	57	1.6940	8	64	0.1510
7	1	57	0.1920	8	64	5.7130
11	1	57	0.4540	8	64	0.1710
12	1	57	0.3140	8	64	0.2110
13	1	57	0.2350	8	64	0.2900
14	1	57	0.1940	8	64	0.5680
18	1	57	0.3930	8	64	0.1210
19	1	57	0.2940	8	64	0.1380
20	1	57	0.2340	8	64	0.1730
21	1	57	0.1930	8	64	0.2110
22	1	57	0.1590	8	64	0.3010
23	1	57	0.1410	8	64	0.5380
26	1	57	0.1670	8	64	0.0830
27	1	57	0.1510	8	64	0.0950
28	1	57	0.1380	8	64	0.1000
29	1	57	0.1250	8	64	0.1250
30	1	57	0.1140	8	64	0.1500
31	1	57	0.1100	8	64	0.1710
34	1	57	-0.0900	8	64	0.0470
35	1	57	-0.0690	8	64	0.0170
36	1	57	0.0000	8	64	0.0000
37	1	57	0.0280	8	64	-0.0500
38	1	57	0.0690	8	64	-0.0800
39	1	57	0.0810	8	64	-0.0940
42	1	57	-0.2580	8	64	-0.0170
43	1	57	-0.1830	8	64	-0.0590
44	1	57	-0.1270	8	64	-0.0850
45	1	57	-0.0790	8	64	-0.1460
46	1	57	-0.0090	8	64	-0.2050
47	1	57	0.0240	8	64	-0.3420
51	1	57	-0.3210	8	64	-0.0950
52	1	57	-0.1980	8	64	-0.1330
53	1	57	-0.1250	8	64	-0.2130
54	1	57	-0.0810	8	64	-0.3950
58	1	57	-1.2120	8	64	-0.0870
63	1	57	-0.0720	8	64	-1.7710

POTENTIAL MEASUREMENTS FOR LARGE GRID
OCTOBER 13,1984

	PATTERN =3			PATTERN =4		
ELECTRODE LOCATION	CURRENT INPUT	CURRENT OUTPUT	NORMALIZED VOLTAGE (2 PI V/I)	CURRENT INPUT	CURRENT OUTPUT	NORMALIZED VOLTAGE (2 PI V/I)
2	10	15	1.1980	50	55	-0.0140
7	10	15	-5.9020	50	55	-0.1790
11	10	15	0.9870	50	55	-0.0470
12	10	15	0.1430	50	55	-0.0810
13	10	15	-0.4760	50	55	-0.1210
14	10	15	-7.3810	50	55	-0.1680
18	10	15	0.8960	50	55	0.0650
19	10	15	0.4540	50	55	0.0190
20	10	15	0.1100	50	55	-0.0790
21	10	15	-0.3490	50	55	-0.1340
22	10	15	-2.4280	50	55	-0.1850
23	10	15	-7.1440	50	55	-0.2350
26	10	15	0.2940	50	55	0.1310
27	10	15	0.2030	50	55	0.0880
28	10	15	0.0740	50	55	-0.0500
29	10	15	-0.1980	50	55	-0.1530
30	10	15	-0.5310	50	55	-0.2410
31	10	15	-0.7950	50	55	-0.2940
34	10	15	0.1660	50	55	0.3010
35	10	15	0.1250	50	55	0.2170
36	10	15	0.0000	50	55	0.0000
37	10	15	-0.1220	50	55	-0.1950
38	10	15	-0.2140	50	55	-0.4050
39	10	15	-0.2800	50	55	-0.4990
42	10	15	0.1230	50	55	0.7960
43	10	15	0.0940	50	55	0.4370
44	10	15	-0.0070	50	55	0.0980
45	10	15	-0.1110	50	55	-0.2780
46	10	15	-0.1610	50	55	-0.7650
47	10	15	-0.2010	50	55	-1.4120
51	10	15	0.0470	50	55	0.7890
52	10	15	-0.0140	50	55	0.1310
53	10	15	-0.0960	50	55	-0.3400
54	10	15	-0.1340	50	55	-1.5310
58	10	15	0.0660	50	55	1.0310
63	10	15	-0.1560	50	55	-1.7730

	PATTERN =5			PATTERN =6		
ELECTRODE LOCATION	CURRENT INPUT	CURRENT OUTPUT	NORMALIZED VOLTAGE (2 PI V/I)	CURRENT INPUT	CURRENT OUTPUT	NORMALIZED VOLTAGE (2 PI V/I)
2	9	56	0.7160	16	49	0.10900
7	9	56	-0.0020	16	49	2.10800
11	9	56	0.4150	16	49	0.15300
12	9	56	0.2450	16	49	0.23000
13	9	56	0.1170	16	49	0.36700
14	9	56	0.0340	16	49	0.93700
18	9	56	0.6780	16	49	-0.01600
19	9	56	0.3450	16	49	0.09900
20	9	56	0.1970	16	49	0.18900
21	9	56	0.0910	16	49	0.31700
22	9	56	-0.0700	16	49	0.69600
23	9	56	-0.1400	16	49	3.09900
26	9	56	0.3400	16	49	-0.12800
27	9	56	0.2300	16	49	-0.02500
28	9	56	0.1260	16	49	0.11000
29	9	56	-0.0230	16	49	0.23500
30	9	56	-0.1490	16	49	0.41300
31	9	56	-0.2280	16	49	0.74800
34	9	56	0.2030	16	49	-0.29500
35	9	56	0.1430	16	49	-0.17400
36	9	56	0.0000	16	49	0.00000
37	9	56	-0.1360	16	49	0.12600
38	9	56	-0.2710	16	49	0.23900
39	9	56	-0.4060	16	49	0.33500
42	9	56	0.1370	16	49	-0.54800
43	9	56	0.0860	16	49	-0.26600
44	9	56	-0.0930	16	49	-0.11000
45	9	56	-0.2160	16	49	0.07100
46	9	56	-0.3940	16	49	0.16000
47	9	56	-0.8320	16	49	0.22300
51	9	56	-0.0420	16	49	-0.34200
52	9	56	-0.1370	16	49	-0.15900
53	9	56	-0.2690	16	49	-0.00800
54	9	56	-0.5340	16	49	0.10900
58	9	56	0.0150	16	49	-0.66100
63	9	56	-1.0580	16	49	0.14200

POTENTIAL MEASUREMENTS FOR LARGE GRID
OCTOBER 13,1984

ELECTRODE LOCATION	PATTERN =7 CURRENT INPUT	CURRENT OUTPUT	NORMALIZED VOLTAGE (2 PI V/I)	PATTERN =8 CURRENT INPUT	CURRENT OUTPUT	NORMALIZED VOLTAGE (2 PI V/I)
2	4	25	0.32200	40	61	0.1190
7	4	25	0.35600	40	61	0.2650
11	4	25	0.74500	40	61	0.1390
12	4	25	2.76500	40	61	0.1660
13	4	25	1.17800	40	61	0.2090
14	4	25	0.47700	40	61	0.2610
18	4	25	-0.29400	40	61	0.1060
19	4	25	0.18800	40	61	0.1230
20	4	25	0.42100	40	61	0.1540
21	4	25	0.43000	40	61	0.2080
22	4	25	0.38800	40	61	0.3070
23	4	25	0.32200	40	61	0.4830
26	4	25	-0.25100	40	61	0.0710
27	4	25	-0.21600	40	61	0.0870
28	4	25	-0.06100	40	61	0.1200
29	4	25	0.25900	40	61	0.1940
30	4	25	0.27200	40	61	0.3800
31	4	25	0.24700	40	61	1.2460
34	4	25	-0.45200	40	61	-0.0510
35	4	25	-0.25700	40	61	-0.0640
36	4	25	0.00000	40	61	0.0000
37	4	25	0.16700	40	61	0.0930
38	4	25	0.20400	40	61	0.3520
39	4	25	0.21600	40	61	2.1540
42	4	25	-0.29900	40	61	-0.0960
43	4	25	-0.20600	40	61	-0.1430
44	4	25	-0.13500	40	61	-0.1970
45	4	25	-0.08200	40	61	-0.2060
46	4	25	0.19700	40	61	0.1100
47	4	25	0.18400	40	61	0.7140
51	4	25	-0.21100	40	61	-0.2510
52	4	25	-0.04200	40	61	-0.5780
53	4	25	0.02800	40	61	-1.0900
54	4	25	0.11200	40	61	-0.4590
58	4	25	-0.22500	40	61	-0.1700
63	4	25	0.10500	40	61	-0.1050

ELECTRODE LOCATION	PATTERN =9 CURRENT INPUT	CURRENT OUTPUT	NORMALIZED VOLTAGE (2 PI V/I)	PATTERN =10 CURRENT INPUT	CURRENT OUTPUT	NORMALIZED VOLTAGE (2 PI V/I)
2	5	32	0.2550	33	60	0.2050
7	5	32	0.3030	33	60	0.0760
11	5	32	0.3560	33	60	0.2020
12	5	32	1.0510	33	60	0.1600
13	5	32	3.3320	33	60	0.1130
14	5	32	1.2620	33	60	0.0910
18	5	32	0.2000	33	60	0.3310
19	5	32	0.2410	33	60	0.2320
20	5	32	0.2910	33	60	0.1530
21	5	32	0.2990	33	60	0.1010
22	5	32	-0.1410	33	60	0.0660
23	5	32	-2.0580	33	60	0.0170
26	5	32	0.1430	33	60	0.6100
27	5	32	0.1420	33	60	0.2810
28	5	32	0.1170	33	60	0.1480
29	5	32	-0.0150	33	60	0.0700
30	5	32	-0.5090	33	60	-0.0100
31	5	32	-6.0570	33	60	-0.0290
34	5	32	0.0880	33	60	0.8900
35	5	32	0.0810	33	60	0.2310
36	5	32	0.0000	33	60	0.0000
37	5	32	-0.1070	33	60	-0.0970
38	5	32	-0.2950	33	60	-0.1070
39	5	32	-1.0950	33	60	-0.0990
42	5	32	0.0680	33	60	0.3910
43	5	32	0.0180	33	60	-0.0150
44	5	32	-0.0610	33	60	-0.2530
45	5	32	-0.1230	33	60	-0.2580
46	5	32	-0.2090	33	60	-0.1950
47	5	32	-0.3270	33	60	-0.1540
51	5	32	-0.0210	33	60	-0.5040
52	5	32	-0.0740	33	60	-1.1310
53	5	32	-0.1210	33	60	-0.6430
54	5	32	-0.1710	33	60	-0.3060
58	5	32	-0.0050	33	60	-0.1900
63	5	32	-0.1790	33	60	-0.2060

POTENTIAL MEASUREMENTS FOR LARGE GRID
OCTOBER 13,1984

	PATTERN =11			PATTERN =12		
ELECTRODE LOCATION	CURRENT INPUT	CURRENT OUTPUT	NORMALIZED VOLTAGE (2 PI V/I)	CURRENT INPUT	CURRENT OUTPUT	NORMALIZED VOLTAGE (2 PI V/I)
2	3	59	2.0160	62	6	-0.3260
7	3	59	0.3150	62	6	-4.6170
11	3	59	2.1510	62	6	-0.3510
12	3	59	1.0660	62	6	-0.5010
13	3	59	0.4960	62	6	-1.5940
14	3	59	0.3560	62	6	-5.0460
18	3	59	0.4200	62	6	-0.2330
19	3	59	0.4860	62	6	-0.2700
20	3	59	0.4400	62	6	-0.3360
21	3	59	0.3460	62	6	-0.4730
22	3	59	0.2860	62	6	-0.6500
23	3	59	0.2480	62	6	-0.5240
26	3	59	0.2080	62	6	-0.1610
27	3	59	0.2260	62	6	-0.1680
28	3	59	0.2140	62	6	-0.1790
29	3	59	0.2050	62	6	-0.2040
30	3	59	0.1980	62	6	-0.2260
31	3	59	0.1870	62	6	-0.2110
34	3	59	-0.0090	62	6	-0.0990
35	3	59	-0.0340	62	6	-0.0510
36	3	59	0.0000	62	6	0.0000
37	3	59	0.0450	62	6	0.0800
38	3	59	0.0970	62	6	0.0990
39	3	59	0.1130	62	6	0.0520
42	3	59	-0.2120	62	6	0.0160
43	3	59	-0.2950	62	6	0.0880
44	3	59	-0.2500	62	6	0.1710
45	3	59	-0.1510	62	6	0.3130
46	3	59	-0.0330	62	6	0.3870
47	3	59	0.0330	62	6	0.3080
51	3	59	-1.1570	62	6	0.1700
52	3	59	-0.6590	62	6	0.3120
53	3	59	-0.2810	62	6	0.8010
54	3	59	-0.1450	62	6	1.6540
58	3	59	-1.1660	62	6	0.1220
63	3	59	-0.0990	62	6	1.2200

	PATTERN =13			PATTERN =14		
ELECTRODE LOCATION	CURRENT INPUT	CURRENT OUTPUT	NORMALIZED VOLTAGE (2 PI V/I)	CURRENT INPUT	CURRENT OUTPUT	NORMALIZED VOLTAGE (2 PI V/I)
2	17	24	0.3370	41	48	0.0410
7	17	24	-0.5720	41	48	-0.2050
11	17	24	0.2310	41	48	0.0600
12	17	24	0.0650	41	48	-0.0730
13	17	24	-0.1750	41	48	-0.1320
14	17	24	-0.5780	41	48	-0.1980
18	17	24	0.9510	41	48	0.1520
19	17	24	0.2800	41	48	0.0940
20	17	24	0.0620	41	48	-0.0630
21	17	24	-0.1980	41	48	-0.1480
22	17	24	-0.7940	41	48	-0.2350
23	17	24	-7.4600	41	48	-0.3110
26	17	24	0.4780	41	48	0.2610
27	17	24	0.2140	41	48	0.1420
28	17	24	0.0580	41	48	-0.0180
29	17	24	-0.1850	41	48	-0.1660
30	17	24	-0.5960	41	48	-0.2950
31	17	24	-2.6950	41	48	-0.4430
34	17	24	0.2580	41	48	0.5680
35	17	24	0.1560	41	48	0.2500
36	17	24	0.0000	41	48	0.0000
37	17	24	-0.1500	41	48	-0.1840
38	17	24	-0.2850	41	48	-0.4110
39	17	24	-0.4700	41	48	-0.8840
42	17	24	0.1800	41	48	0.8620
43	17	24	0.1140	41	48	0.2680
44	17	24	-0.0110	41	48	0.0320
45	17	24	-0.1300	41	48	-0.2010
46	17	24	-0.2100	41	48	-0.4600
47	17	24	-0.2800	41	48	-1.4900
51	17	24	0.0750	41	48	0.2130
52	17	24	-0.0260	41	48	0.0160
53	17	24	-0.1160	41	48	-0.1940
54	17	24	-0.1810	41	48	-0.4190
58	17	24	0.0880	41	48	0.2950
63	17	24	-0.1960	41	48	-0.5430

REFERENCES

REFERENCES

1. Alfano, Luigi: "On the Possibility of Direct Inversion of D.C. Geoelectric Data", Ettore Majorana, pp. 259-277, April 1980.

2. Allard, R.J.P.: "Geophysical and Numerical Modelling of a Pollution Plume in an Aquifer Test Bed", B.Sc. thesis, University of Manitoba, 1985.

3. Bernabini, Marcello: "Methods for Geoelectrical Data Inversion", Ettore Majorana, pp. 279-299, April 1980.

4. Cowan, D.R., and Omnes, G.: "Resistivity Surveys for Groundwater at Depot Springs, Near Agnew, Western Australia", Australian I.M.M. Conference, Part B, pp. 527-536, June 1975.

5. Davis, P.A., et al.: "Resistivity Sounding Computations with Any Array using a Single Digital Filter", Bull. Aust. Soc. Explor. Geophys. V.II no. ½, June 1980.

6. De Beer, J.H.: "The Theory and Application of Techniques for the Interpretation of Schlumberger Sounding Curves", Ser. Al (Geol.) Vol. 7, pp. 107-147, 1977.

7. Fenton, Mark M.: "The Pleistocene Stratigraphy and Surficial Geology of the Assiniboine River to Lake Manitoba Area, Manitoba", M.Sc. thesis, University of Manitoba, October 1970.

8. Flathe, H.: "The Role of a Geologic Concept in Geophysical Research Work for Solving Hydrogeological Problems", Federal Institute for Geosciences and Natural Resources (West Germany), pp. 129-139, 1975.

9. Gilliland, J.A.: "Geological and Ground Water Investigation for the Portage Diversion", (unpublished report) Water Control and Conservation Branch, Manitoba, Feb. 1965.

10. Habberjam, G.M.: "Apparent Resistivity Observations and the use of Square Array Techniques", Geoexploration Monographs, Ser. 1, No. 9, Berlin, 1979.

11. Mandel, Cary: "A Novel Impedance Computed Algorithm, Some Results", B.Sc. thesis, University of Manitoba, 1985.

12. Mooney, Harold M. and Wetzel W.W.: "The Potentials about a Point Electrode and Apparent Resistivity Curves for a Two-, Three-, and Four-Layered Earth", The University of Minnesota Press, Minneapolis, 1956.

13. Mooney, Harold M.: "Handbook of Engineering Geophysics", Vol.2: Electrical Resistivity, 1980.

14. Mundry, Erich and Dennert, Ulrich: "Das Umkehrproblem in der Geoelektrik", Festkolloquium, Federal Institute for Geosciences and Natural Resources (West Germany), 1979.

15. Pratt, David, A. and Whiteley, Robert J.: "Computer Simulation and Evaluation of Electrode Array Responses in Resistivity and I.P. Prospecting", Bull. Aust. Soc. Explor. Geophys., v.5, no.2. June 1974.

16. Rao, T.G., et al.: "Resistivity Surveys in Lower Maner Basin", NGRI, Hyderabad, --.

17. Slaine, D.: "Portage La Prairie Landfill Study", Gartner Lee Associates Limited (Consulting report for Dept. of Environment, Manitoba), 1985.

18. Underwood McLellan Ltd.: "Phase II Landfill Study - Stony Mountain - Winkler - Portage La Prairie", for Manitoba Environment and Environment Canada, 1984.

19. Ushijima, Keisuke: "Automatic Interpretation of Schlumberger Soundings", Geoth. Res. Council, trans vol.4, Sept. 1980.

20. Wexler, A., et al.: "An Imped nce Computed Tomography Algorithm and System", Optical Society of America, August 1984. *

21. Wolowich, E., Tamburi, A.: "Sediment Dynamics on the Assiniboine River", CSCE Conference, Saskatoon, Saskatchewan, May 1985.

22. U.S. Environmental Protection Agency: "Geophysical Techniques for Sensing Buried Waste and Waste Migration", Las Vegas, Nevada, 1982.

* Meeting, Hecla Island, 1984.

LEGEND

- DUMP 1948
- OPEN WATER 1948
- FLOODPLAIN SILTS
- NORTH FAN
- EAST FAN
- SCAR
- PROGRESSION

PHASE I = EARLY MEANDERS

PHASE 2 = RECENT MEANDERS

FIGURE 18 B

GEOLOGY AND MEANDER ACTIVITY

by U. Roeper 1985

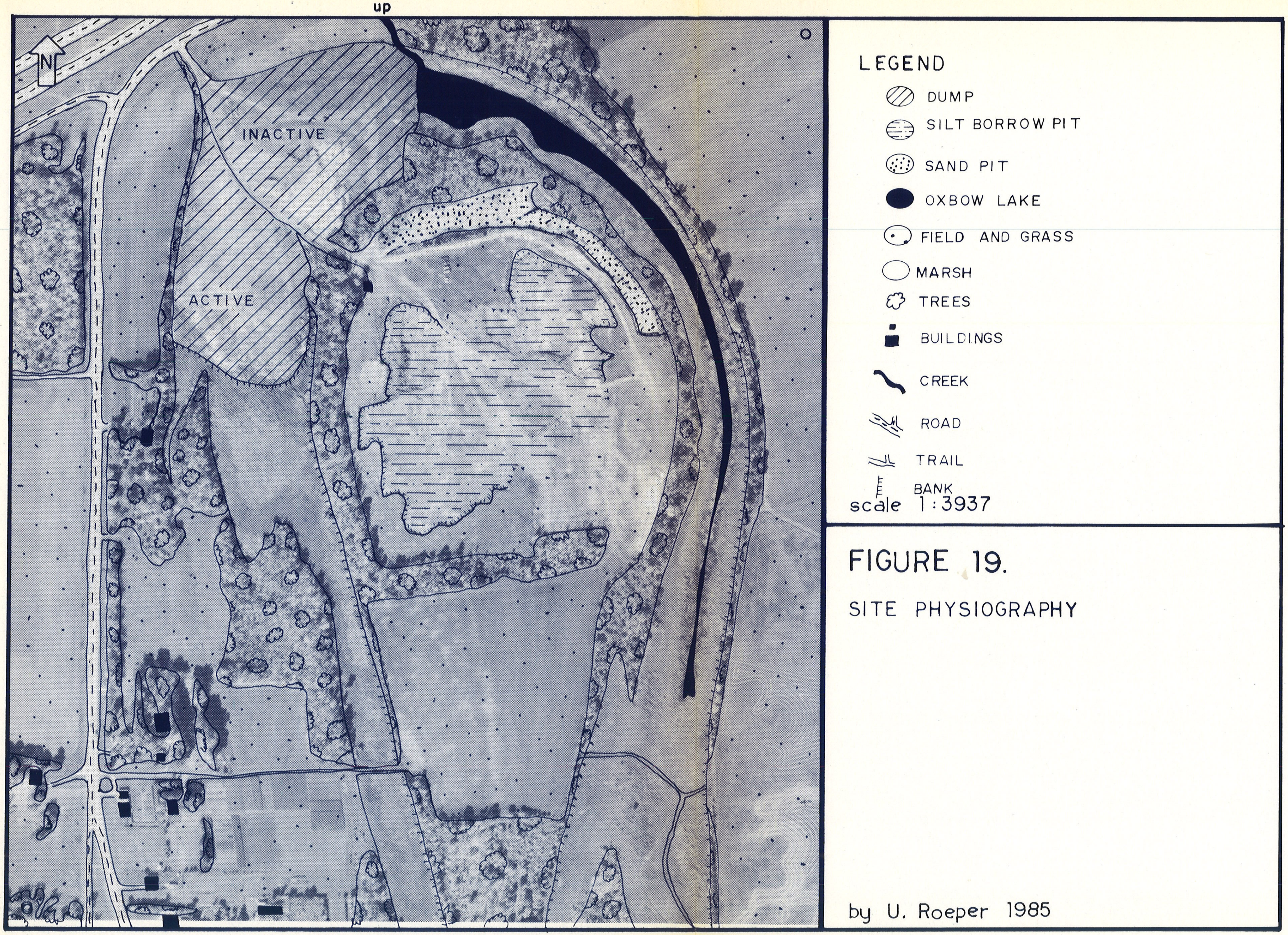

FIGURE 19.

SITE PHYSIOGRAPHY

by U. Roeper 1985

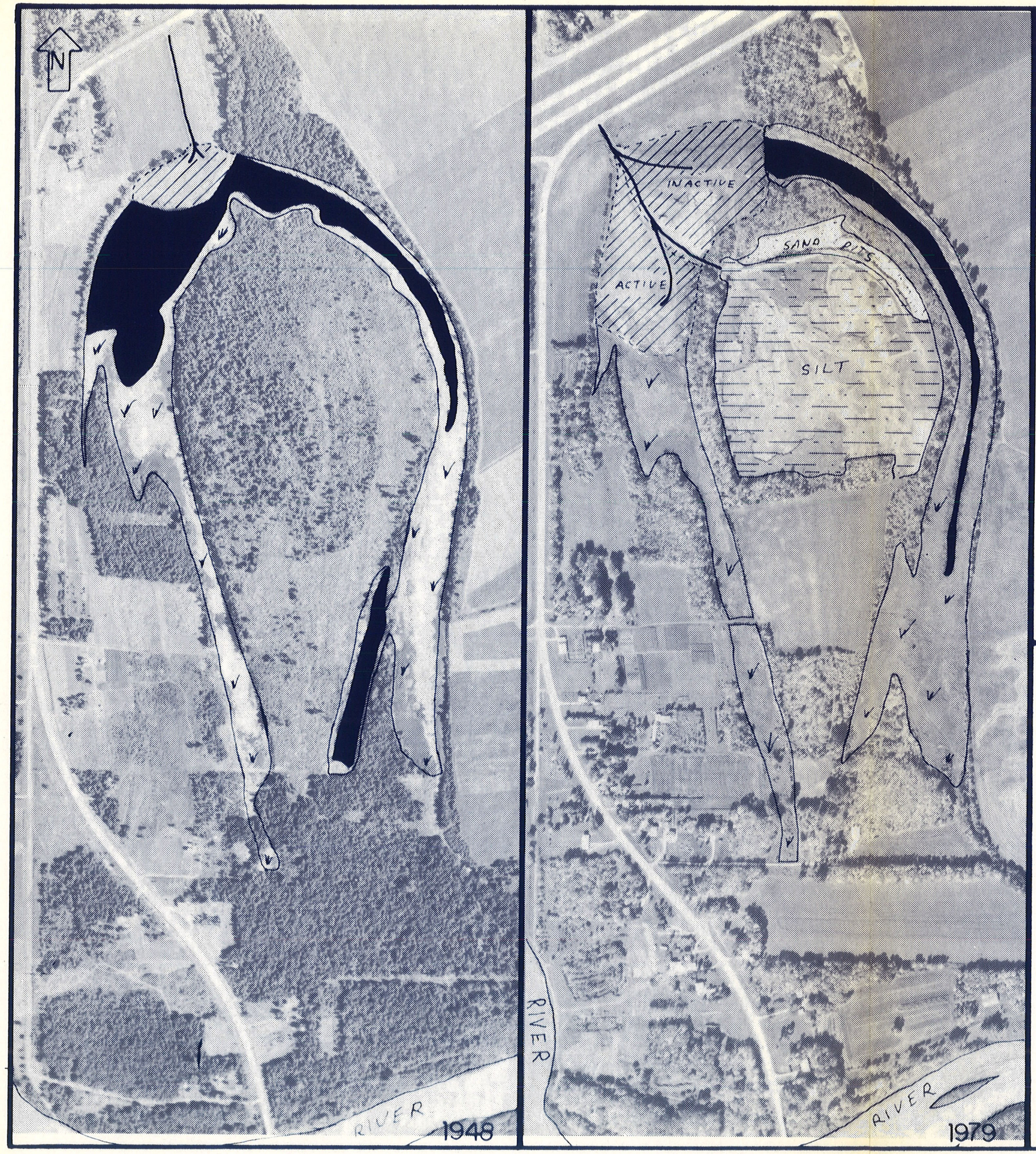

LEGEND

DUMP

SILT BORROW PIT

OX BOW

OXBOW LAKE

scale 1:7874

FIGURE 20.

SITE HISTORY AND EXTENT OF OPEN WATER IN GEORGE LAKE IN 1948 AND 1979

by U. Roeper 1985

up

LEGEND

DUMP

WATER

OXBOW

● PROVINCE OF MANITOBA
MONITORING WELL

27.50 STATIC WATER LEVEL 20.11.85
BY G.L.A.
ELEVATIONS UNREFERENCED METERS

scale 1: 3937

FIGURE 22.

GROUND WATER LEVELS

by U. Roeper 1985

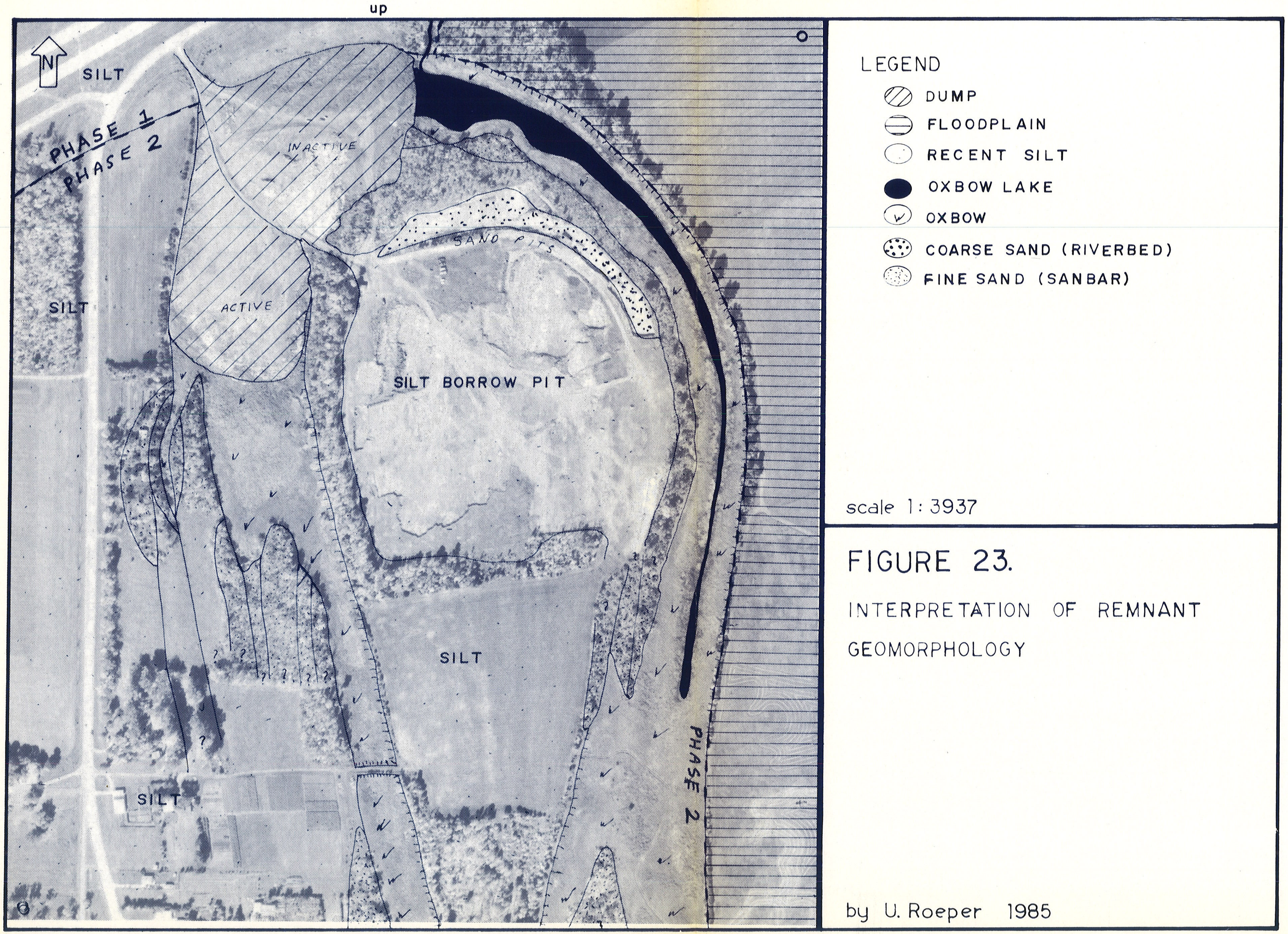

scale 1: 3937

FIGURE 23.

INTERPRETATION OF REMNANT GEOMORPHOLOGY

by U. Roeper 1985

LEGEND

DUMP

OXBOW

OXBOW LAKE

2200 — — MAY 1985

—2270— OCT. 1984 (G.L.A.)

— — 1320 OCT. 1983 (UMA)

scale 1:3937

FIGURE 26.

CONDUCTIVITY OF GROUND WATER

by U. Roeper 1985

up

LEGEND

DUMP

OXBOW

OXBOW LAKE

S1 SOUNDING

SOUNDING BY G.L.A

P1 PROFILE

scale 1:3937

FIGURE 27.

RESISTIVITY PROFILES AND SOUNDINGS

by U. Roeper 1985

up

LEGEND

DUMP

OXBOW MARSH

OXBOW LAKE

scale 1:3937

FIGURE 28.

ELECTRODE GRID LOCATIONS

by U. Roeper 1985